Low-dimensional descriptions of high-dimensional frictional hysteresis

A Thesis Submitted
in Partial Fulfillment of the Requirements
for the Degree of

Doctor of Philosophy

by

Saurabh Biswas

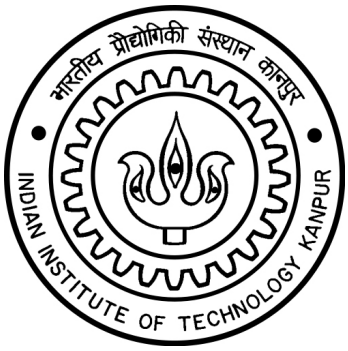

to the

DEPARTMENT OF MECHANICAL ENGINEERING
INDIAN INSTITUTE OF TECHNOLOGY KANPUR

February, 2018

Dedicated to

my late grandmother

Certificate

It is certified that the work contained in this thesis titled **"Low dimensional descriptions of high dimensional frictional hysteresis"** by **Saurabh Biswas** (Roll No. 12105178), has been carried out under my supervision and that the work has not been submitted elsewhere for a degree.

Anindya Chatterjee
Mechanical Engineering
IIT Kanpur

August, 2017

Acknowledgments

First and foremost, I would like to express my deep sense of gratitude towards my advisor Prof. Anindya Chatterjee for his valuable guidance and thorough evaluation at every stage of this work. He introduced me to the problems I studied in this thesis and helped me by giving ideas to solve them. This work has been completed only due to his constant encouragement, valuable suggestions, critical comments, and deep involvement. I would like to take the opportunity to specially appreciate his unique thinking and problem solving abilities. He has always influenced me by his passion and dedication for his research. I thank him for letting me gather valuable experience in tutoring in an undergraduate Dynamics course. I also thank him for introducing me to his "*Dilbert's Problems*", which helped me immensely in developing some very useful skills that I invariably needed in my research. Last but not the least, he often spent his time in sharing his knowledge and views on several philosophical aspects of life, which always invigorated my thoughts.

I would like to express my thanks to Dr. Prasun Jana for his collaboration in the fifth problem of this thesis.

I would like to extend my thanks to Prof. Pankaj Wahi, Prof. Anurag Gupta, Prof. Shakti Gupta and Prof. Sumit Basu for teaching courses which helped me directly or indirectly in my research. I have had an enriching experience with Prof. Bhaskar Dasgupta while working with him as a teaching assistant in a course.

I take the opportunity to thank *all* my lab members of KanGAL for making the lab a vibrant place to work. I would specially thank to Dr. Rakshit, Susheel, Numan, Ritwik, Soumyabrata, Sankalp, Santhosh, Tapan, Ashok, Ghulam, Arunava, Aakash, Ankush, Arnab and Chetna. They have always been responsive whenever

I needed any help. We had countless discussions and friendly debates on various topics, both technical and non-technical. It would have been extremely difficult to survive as a graduate student at IIT Kanpur without their company.

Thanks are due to my friends Satyaki, Arunabha, Sunil, Ratul, David, Prasad, Vaibhav, Guruprasad and Prabhat for making my long stay at IIT Kanpur a memorable one.

I would like to thank the SERB, Govt. of India, for partially funding this research project. I thank the DORA, IIT Kanpur for twice providing me partial financial supports for attending the conferences, 17th USNCTAM (2014) held at Michigan State University, USA; and PACAM XV (2015) held at University of Illinois at Urbana-Champaign, USA. I thank the Technical Committee on Vibration and Sound, ASME for providing me partial financial support for attending the ASME IDETC/CIE conference (2016) held at Charlotte, USA.

Finally, I would like to express my heartfelt gratitude to my parents and my elder brother for trusting and encouraging me in *all* situations. It would not have been possible for me to follow my dreams without their unconditional love, support and sacrifices.

Saurabh

IIT Kanpur

February, 2018

Abstract

Hysteresis is an irreversible, memory dependent, approximately rate-independent phenomenon seen in many systems, e.g., frictional systems and magnets. This thesis develops new low-dimensional descriptions of rate-independent hysteresis in systems with friction.

The thesis considers five different problems.

In the first problem, a high-dimensional massless frictional system is studied. The original system, being given in terms of signs of velocities, is first solved incrementally using a linear complementarity problem formulation. From this numerical solution, to develop a reduced-order model, basis vectors are chosen using the singular value decomposition. The slip direction in generalized coordinates is identified as the minimizer of a complicated function, which includes many signum nonlinearities. Fortunately, it allows a convenient analytical approximation. Upon solution of the approximated minimization problem, the slip direction is found. Finally, an evolution equation with six states is obtained that gives a good match with the full solution.

In the second problem, a more intuitively appealing frictional system is used that resembles the Iwan model (1966), but is much more high-dimensional than usual. The basis functions now allow analytical description. The number of states required for approximate modeling decreases from six to two, which is a theoretical minimum. The number of fitted parameters is reduced to six. Parameter fitting to match specified hysteresis loops is demonstrated.

In the third problem, hysteresis in frictional bolted lap joints is studied using ABAQUS. The computationally obtained hysteresis loops are normalized and

transformed to new ones with standardized slopes and widths. Then the foregoing two-state model is applied to capture these normalized loops. Interestingly, for single-bolted lap joints, the same hysteresis model works well over a range of friction coefficients and bolt preloads. For a double-bolted lap joint, the fitted parameters differ for different combinations of friction coefficients and bolt preloads.

In the fourth problem, an explicit approximation for a part of the computation in the aforementioned two-state model is developed. Specifically, the slip direction in the two-state model is given by a patched asymptotic approximation. The approximation gives an excellent match with the exact solution, and may help to develop insights into a slightly complicated part of the calculations in the two-state model.

In the fifth and final problem, an elastic plate with several randomly distributed frictional microcracks is studied using ABAQUS. Computational solutions show narrow hysteresis loops that are pinched at the origin, similar to an ad hoc model due to Reid (1956). Such pinched loops have been revisited lately by others, but our results provide new justification for the same. A new simple scalar model is proposed that gives a reasonable qualitative match with the numerically obtained hysteresis loops. This new model has a single state, and is quite different from the models developed and used in the first four parts above.

Keywords: hysteresis, minor loops, friction, reduced order model, Iwan model, parameter fitting, bolted joint, internal dissipation, microcracks

Contents

List of Figures

List of Tables

Chapter 1

Introduction

This thesis develops new low-dimensional descriptions of high-dimensional frictional hysteretic systems.

Hysteresis is an irreversible, nonlinear, memory-dependent behavior that occurs in many systems. Hysteresis is seen in material stress-strain relations and damping, in magnetism, in wetting-dewetting, and even in economics (see the three volumes of Bertotti & Mayergoyz [1] and the references therein). The observation of hysteresis in magnetism is attributed to Ewing [2], and a nice stress-strain hysteresis curve for material dissipation was given by Rowett [3]. An early mathematical model for hysteretic behavior in ferromagnetism was given by Preisach [4]. More recently, hysteresis has been noted in many other areas, and there has been much research in the physics, modeling, numerical simulation and dynamics of systems with hysteresis (see [1] and the references therein). To depict key qualitative features, a hysteresis curve for a mechanical element is sketched in Figure 1.1(a), and another for a magnet is sketched in Figure 1.1(b).

The present study is motivated by the rate-independent hysteresis in mechanical systems with friction. For example, many engineering materials exhibit internal dissipation through hysteresis under cyclic deformation. It has long been known that many materials, under such cyclic loading, show an energy dissipation per cycle that is independent of the frequency of the loading (for small frequencies, such as up to a few hundred Hz): see e.g., Lord Kelvin [5], Rowett [3] and Kimball & Lovell [6]. In

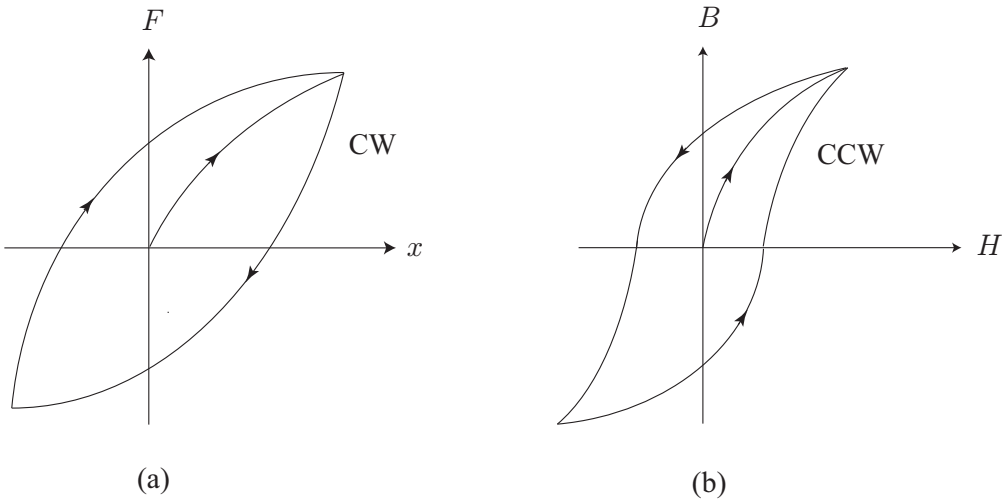

Figure 1.1: Hysteresis loops in (a) mechanical elements, and (b) magnets. F is a force and x is a displacement or stretching response; H is an applied magnetic field and B is the resulting magnetic flux density (the response). In (a), the steady periodic response traverses the loop clockwise; in (b), it is counterclockwise. There can be transients before the steady state behavior is established, though they have not been indicated in the figures, for simplicity.

rate-independent systems, the slope of the hysteresis curve depends discontinuously on the *sign* of the rate of change of loading. This dependence on the direction of loading leads to sharp corners (see Figure 1.1(a) and (b)) in hysteresis loops upon load reversals. Under simple cyclic loading, the area enclosed by the hysteresis loop gives the amount of energy dissipated in suitable units. Under more complex load histories, which contain smaller partial unloadings and reloadings within the larger load cycles, the hysteresis loop can show smaller *minor loops* within itself. These *minor loops* need to be captured accurately to measure the overall dissipation well. To that end this thesis presents new simple low-dimensional rate-independent hysteresis models that capture *minor loops* fairly accurately.

1.1 Contribution of this thesis

The main contribution of this thesis may be roughly divided into four parts. We write equations for high-dimensional frictional rate-independent hysteretic systems from first principles, and develop an unconventional approach to derive low-dimensional

models thereof; we apply our low-dimensional model to describe hysteresis in bolted lap joints, including minor loops from partial unloading; we develop an explicit approximation for an iterative part of the computation involved in our low-dimensional model; and we propose a separate scalar model with pinched hysteresis loops, motivated by a finite element based study of an elastic plate with frictional microcracks.

In the following paragraphs, we briefly give the background motivation of the problems addressed, and we highlight the notable contributions made in this thesis.

Hysteresis in material behavior includes both signum nonlinearities as well as high dimensionality. Available low-dimensional evolution equations that model hysteresis are empirical, such as the famous Bouc-Wen model [7, 8]. The Bouc-Wen model has been widely used in structural mechanics (see e.g., [9]) and is based on a simple scalar ordinary differential equation, but it cannot capture minor loops upon small load reversals within larger loading paths. With this motivation, in chapter 2, we study a high-dimensional frictional hysteretic system. The model shows hysteresis including major and minor loops. From that high- dimensional system, we derive a low-dimensional model by identifying a slip criterion as will be discussed in due course. The low-dimensional model has six states and gives a good match with the full solution.

For hysteresis in mechanical systems with elasticity and friction, the Iwan model [10, 11] has been used by many researchers. The Iwan model shows a more realistic response in contrast to the Bouc-Wen model under loadings that contain small reversals, but is high-dimensional with many elastic and dry friction elements (also known as Jenkins elements). The evolution of the Iwan model is not easily expressible in terms of a few ordinary differential equations. In chapter 3, following our work in chapter 2, we derive a reduced-order, two-state approximation (with six parameters) to a high-dimensional Iwan model, which can be used for practical parameter fitting to match a range of given hysteretic data including minor loops.

Hysteretic dissipation can occur in bolted lap joints *via* small-scale frictional sliding between the contacting surfaces. Detailed study of dissipation in bolted joints

requires solving nonlinear contact mechanics problem at the joint interfaces. Such nonlinear contact mechanics problems can be solved using commercial finite element packages. However, due to modeling complexities and high computational cost of full finite element solution, a simpler model that describes hysteresis in joints is desirable. In recent times, several authors have used the Iwan model and its variants to study hysteresis in bolted joints: see e.g., Segalman [12], Brake [13]. With the above motivation, in chapter 4, we first perform detailed finite element analysis of frictional bolted lap joints using ABAQUS to compute hysteretic responses. We normalize the computed hysteresis loops to standardize their shape and size. Subsequently, we apply our foregoing two state model of chapter 3 with just two free parameters to describe these normalized hysteresis loops. An excellent match is obtained.

As outlined above, to measure overall dissipation in a material accurately, one would seek to characterize the actual shape of the hysteresis loops on the stress-strain curves. The available literature on material dissipation contains both papers that deal with the net dissipation per cycle, as well as papers that consider details of the shapes of hysteresis loops: see e.g., Lazan (1968) [14]. In 1956, Reid [15] proposed an *ad hoc* model that shows nonintuitive hysteresis loops that are pinched at the origin. Such pinched loops are markedly different from the loops from Rowett's experiment, or from the Bouc-Wen model, or from the models developed and used in the first four parts of the thesis. In chapter 6, we present a detailed computational study that justifies such nonintuitive hysteresis loop shapes. Specifically, we study an elastic plate with several randomly distributed and oriented frictional microcracks, loaded cyclically in plane stress. Computational solutions in ABAQUS show hysteresis loops that are pinched at the origin and partially resemble the loops from Reid's model. A useful contribution of the final part of this thesis is a simple scalar evolution equation that qualitatively and approximately matches the hysteresis loops obtained from the computational study.

1.2 Layout of the thesis

In chapter 2, we first study a high-dimensional rate-independent frictional system, and then develop a new unconventional approach to derive a reduced order model from that high-dimensional system. Material from this chapter has been published in [16].

In chapter 3, we study a more intuitively appealing high-dimensional system that partially resembles the Iwan model. Following the same approach as developed in chapter 2, we obtain a two-state evolution equation that captures a wide range of hysteretic behaviors. Material from this chapter has been published in [32].

In chapter 4, we apply our foregoing two-state model to describe hysteresis in finite element models of frictional bolted joints. We also develop new analytical insights into our two-state model of chapter 3.

In chapter 5, we propose an explicit approximation for a part of the computation involved in the two-state model of chapter 3.

In chapter 6, we present a finite element study of an elastic plate with several frictional microcracks. The study yields nonintuitive pinched hysteresis loops. We propose a new scalar hysteresis model that shows such pinched hysteresis loops. Material from this chapter has been published in [58]. The work of chapter 6 was partially guided by Dr. Prasun Jana.

Finally, some concluding discussion is presented in chapter 7.

Chapter 2

A reduced order model from high-dimensional frictional hysteresis

In this chapter, we present a study of a high-dimensional rate-independent frictional system. The original system, being given in terms of signs of velocities, is first solved incrementally using a linear complementarity problem formulation. Numerical solutions show hysteresis including minor loops. From that high-dimensional system, we derive a low-dimensional model with six states by identifying a slip criterion. The low-dimensional model gives a good match with the full solution. The material of this chapter has been published in [16].

2.1 Introduction

Hysteresis, a phenomenon involving persistent memory effects, occurs in many systems, e.g., frictional systems and magnets. The underlying microscopic physics of material hysteresis is complicated. Attempts have been made over several decades to describe hysteretic responses by means of physical, semi-physical and purely empirical models [1]. A dominant majority of theoretical papers on hysteretic phenomena have concerned themselves with magnetism, for which complex theories, models,

and simulations have been developed.

However, options have been limited for simple simulation of hysteretic systems using modest computational effort. Prominent among these have been the classical and modified Preisach models and, in structural mechanics, the Bouc-Wen model [7, 8]. Of these, the Preisach type models are somewhat complicated for numerical use. These models work with an underlying distribution of idealized hysteretic elements, and during loading and unloading the states of these distributed elements need to be tracked[1]. The tracking is done using vertical and horizontal lines that sweep out portions within a triangular region where the random parameters of the hysteresis elements are distributed. The Preisach model's evolution is thus given in terms of successive geometrical constructions and is not easily expressible in terms of differential equations. In contrast to the Preisach type models, the Bouc-Wen model involves a single scalar differential equation and is much easier to use, but has a fundamental limitation as we will describe below.

Our own study of hysteresis models is motivated by an interest in internal damping in materials [17, 18]. For modeling internal damping under temporally-complex stress cycles (specifically with minor unloading loops within larger loading cycles), we seek appropriate low-dimensional heuristic models of hysteretic response and dissipation.

For hysteretic behavior in structural mechanics, the Bouc-Wen model has been used by many authors (see [9] and references therein). In the basic Bouc-Wen model, the hysteretic part of the force is given by a single internal variable z driven by a displacement input u, as in

$$\dot{z} = \alpha_1 \dot{u} - \alpha_2 |\dot{u}||z|^{n-1} z - \alpha_3 \dot{u} |z|^n, \tag{2.1}$$

[1]User-friendly code for the Preisach model is available in [1], vol. I, p. 683. There, evolution equations are not solved explicitly: the forcing history of interest is to be supplied in advance.

where α_1, α_2, α_3 and n are parameters that must satisfy

$$\alpha_1 > 0,\ \alpha_2 > 0,\ \alpha_3 \in [-\alpha_2, \alpha_2],\ \text{and}\ n > 0$$

[19, 20]. A key aspect of hysteretic material behavior is that, within a larger load cycle, if there is a minor unloading-loading loop, then the response also shows a minor loop that turns around and intersects itself. As explained below, the Bouc-Wen model cannot incorporate such self-intersection or minor loop closure. Figure 2.1 illustrates such non-closure, which leads to large differences between simulated and physically relevant behaviors. As seen in the figure, the hysteresis loops slide around too much in the horizontal direction.

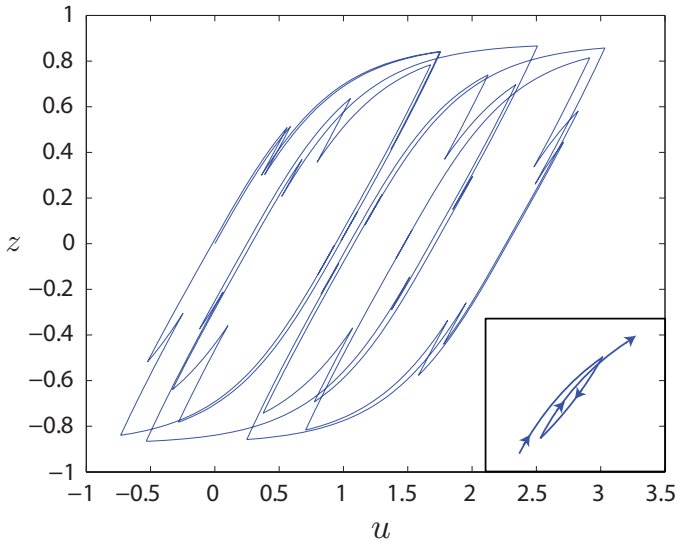

Figure 2.1: Main figure: Response of the Bouc-Wen model. Here, $\alpha_1 = 1$, $\alpha_2 = 0.8$, $\alpha_3 = 0.5$, and $n = 2$; and u was chosen to ensure that $z = 0.619\,(\sin(t) + 0.4\sin(4.16753\,t))$; these numerical values will be reused later, but are otherwise arbitrary. Inset, bottom right: a sketch of the sort of minor loop closure that is *not* shown by the Bouc-Wen model.

The inability of the Bouc-Wen model to capture such minor loops has motivated further *ad hoc* treatment: see e.g., [21]. However, we will adopt a more constructive approach in this chapter. To this end, note that the Bouc-Wen model (Eq. (2.1)) is a special case of a more general class of models of the form

$$\dot{z} = \dot{u}\, f(z, u, \mathrm{sgn}(\dot{u})), \tag{2.2}$$

where the premultiplier $\dot{u}$ and the internal dependence only on the sign of $\dot{u}$ together ensure rate-independence (other examples may be found in [22, 23]). The above can be rewritten as

$$\frac{dz}{du} = f(z, u, \mathrm{sgn}(\dot{u})). \tag{2.3}$$

If the right hand side of Eq. (2.3) did not include dependence on $\mathrm{sgn}(\dot{u})$, then loading and unloading paths would be the same and there would be no hysteresis. In this way, the Bouc-Wen model is clever and simple. However, models of the form of Eq. (2.2) cannot capture minor loops if there are more than two rate reversals within one forcing cycle, as may be seen from Figure 2.2. In the figure, responses are shown to two different forcing histories: one of small amplitude, with no additional rate reversals within the forcing cycle, and one of larger amplitude, *with* additional rate reversals within the forcing cycle. The amplitudes are adjusted so that the two solution loops touch at a point: it is emphasized that these are two different responses, under different forcing histories, of the *same* hypothetical hysteretic material. Such circumstances are easy to create in experiments with magnets [24], and our high-dimensional frictional model below will show such solutions as well. There is nothing unphysical about the circumstances depicted in the figure.

Yet, at the point where the two solution loops touch, there are two different curves along which F and x both increase. Recall that F and x here correspond to z and u in Eqs. (2.2) and (2.3). Thus, the right hand side of Eq. (2.3) is the same, but the left hand side is not. We conclude that physical behavior as depicted in Figure 2.2 implies hidden internal variables in addition to z; and this is a basic weakness of *all* models of the form of Eq. (2.2).

We can now motivate this work as follows. Experiments with magnets or hysteretic mechanical elements, even under complex loading, often only give access to the external variables (F and x; or H and B; or more abstractly z and u). In contrast, a numerical study of a frictional system with many internal variables can give us access to *all* internal variables. A study of such a system may yield better understanding of low order modeling of hysteresis in general. In this chapter, we present a

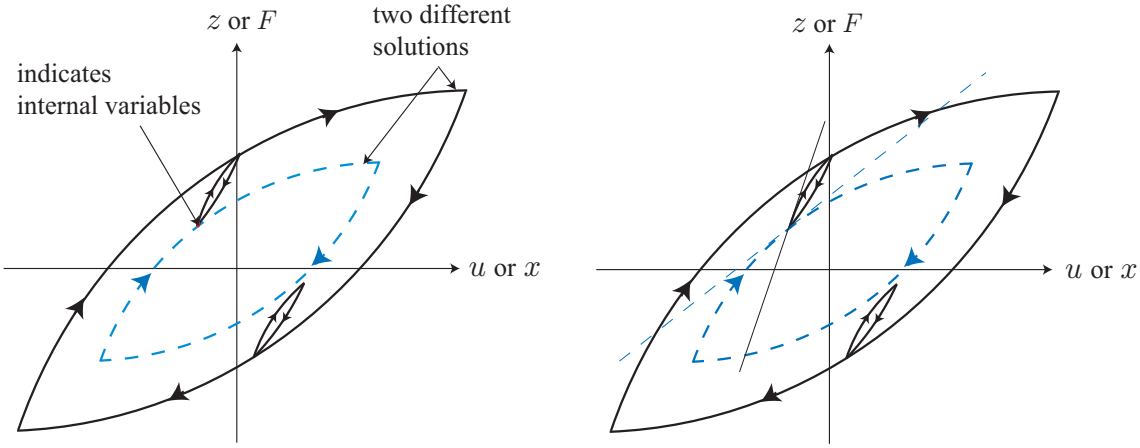

Figure 2.2: Left: Responses to two different hypothetical forcing histories. One has a small amplitude and two rate reversals per period (dashed line). The other has a larger amplitude with unloading or sub-loops within each cycle (solid line). The relative amplitudes of forcing can be adjusted to make the two solution curves touch at a point. Right: The same loops redrawn. At the point where the two solution curves touch, there are two different tangents as indicated: here, z, u, and $\mathrm{sgn}(\dot{u})$ are the same, but $\dfrac{dz}{du}$ differs, and so Eq. (2.3) is insufficient.

study of such a high-dimensional frictional rate-independent hysteretic system, and show how a low-dimensional model can be purposefully constructed from it. We have not found any similar study in the literature.

2.2 High-dimensional frictional system

Figure 2.3 schematically depicts a high-dimensional frictional system. Here B_1, B_2, $B_3, \cdots, B_N$ are N massless blocks. These blocks are arbitrarily interconnected by springs of stiffness k_1, k_2, $k_3, \cdots$. In the figure, $b_1 f(t)$, $b_2 f(t)$, $b_3 f(t), \cdots, b_N f(t)$ are external forces on the blocks. Friction forces on the blocks are written as $F_1 = -\mu_1 \,\mathrm{sgn}(\dot{x}_1)$, $F_2 = -\mu_2 \,\mathrm{sgn}(\dot{x}_2)$, $F_3 = -\mu_3 \,\mathrm{sgn}(\dot{x}_3), \cdots, F_N = -\mu_N \,\mathrm{sgn}(\dot{x}_N)$. The governing equation is (see Appendix A)

$$\mu \,\mathrm{sgn}(\dot{x}) + Kx = bf(t), \tag{2.4}$$

where x is an N-dimensional vector, μ is an $N \times N$ diagonal matrix with positive elements, K is a symmetric positive definite matrix of size $N \times N$, b is an N-

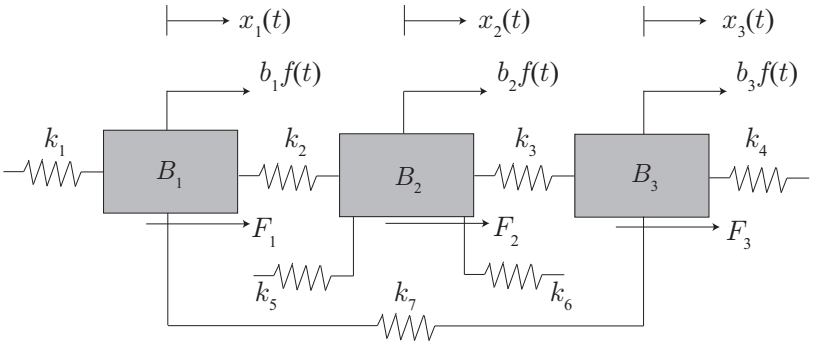

Figure 2.3: High-dimensional frictional system.

dimensional vector, and $f(t)$ is a scalar differentiable function of time representing an oscillating load; and where the *signum* function 'sgn' is defined elementwise and understood to be plus 1 for positive values of the argument, minus 1 for negative values of the argument, and multivalued (within $[-1, 1]$) when the argument is zero.

Note that the system of Eq. (2.4) is rate-independent, since the system depends only on the *sign* of $\dot{x}$. Equation (2.4) is not a set of ordinary differential equations (ODEs) in the usual sense, because the signum function is not invertible. However, the system can be incrementally solved by casting it into the form of a linear complementarity problem (LCP; see [25]), as outlined in Appendix A. For numerical solution of the LCP for each time increment, we used Lemke's algorithm as implemented in a freely available Matlab program (see [26])[2]. For verification, we also solved the above system for moderate N using a smoothed version of the signum function along with some numerical tricks, and obtained the same results as from the quicker LCP; details are omitted.

Before we proceed with numerical solutions, we point out that variables x_i' act as internal variables (recall Figure 2.2), and when we will develop a reduced-order model later, the reduced set of variables will constitute internal variables.

[2] "CompEcon Toolbox." At the time of writing, the code is also available at http://people.sc.fsu.edu/~jburkardt/m_ src/lemke/lemke.m

2.2.1 Direct numerical solution

We first solve Eq. (2.4) for random choices of μ, K and b, and under oscillatory $f(t)$. To this end, we generate a 500-dimensional random system in Matlab as follows[3]. The μ values are uniformly distributed in $(0, 1)$. K has random orthogonal eigenvectors and eigenvalues uniformly distributed in $(0, 3)$. The elements of b are normally distributed with zero mean and unit variance. Finally, we take $f = \sin(t) + 0.4\sin(4.16753\,t)$ for initial simulation (compare this f with z in Figure 2.1). Figure 2.4 shows the results obtained. These will be combined into an effective scalar displacement below.

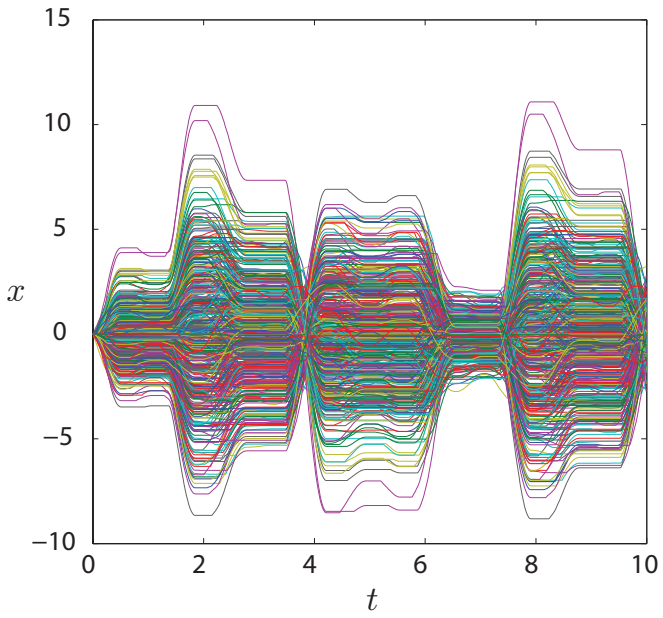

Figure 2.4: Response vs. time for a random 500 dimensional massless frictional system. The different graphs show the various elements of x plotted against time. Periods of constancy (sticking) and variation (slipping) are seen for each element.

2.2.2 Underlying two-dimensional plot

Our f is generalized scalar force, while the response x above is high-dimensional. We need an effective scalar displacement, which we will identify using the work done by the external forces. The incremental work done on the system by all the external

[3]The Matlab commands are: "`n = 500; P = orth(randn(n)); D = diag(3*rand(n,1)); K = P'*D*P; b = randn(n,1); mu = diag(rand(n,1));`"

forces is

$$dW = fb^T dx.$$

Letting $b^T dx = d\xi$, or $\xi = b^T x$, we find $dW = f d\xi$. Thus, ξ is the appropriate generalized displacement[4]. We can now study the hysteretic behavior of the frictional system through plots of force f against displacement ξ.

Figure 2.5 shows solutions for zero initial conditions and three different forcing histories: f, $0.65f$, and $0.8f$. The hysteresis curves obtained in Figure 2.5 exhibit

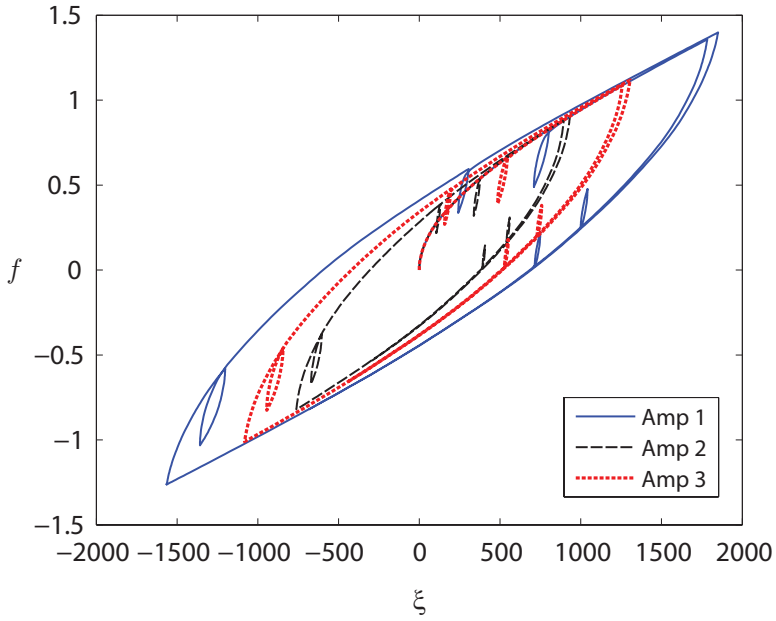

Figure 2.5: Hysteresis loops for the 500 dimensional frictional system with different forcing amplitudes. Amplitude 1 ("Amp 1") has $f = \sin(t) + 0.4\,\sin(4.16753\,t)$; Amplitudes 2 and 3 refer to $f = 0.65\,(\sin(t) + 0.4\,\sin(4.16753\,t))$ and $f = 0.80\,(\sin(t) + 0.4\,\sin(4.16753\,t))$ respectively.

both major and minor loops, unlike the Bouc-Wen model. The solution curves for Amplitudes 1 and 3 touch at a point, as anticipated in Figure 2.2, showing that such behavior is physically permissible and that hysteresis models need additional internal variables. They cannot have the simple form of Eqs. (2.2) and (2.3).

We now have a high-dimensional rate-independent system that shows hysteresis. The system violates no physical laws. Unlike typical experimental systems, here we

[4]The generalized displacement needs to be the work conjugate of the force. This is consistent with nonlinear continuum mechanics, where the strain measure has to be consistent with the stress measure (see e.g., p. 155 of [27]).

have access to every internal state. We are now ready to attack the main problem addressed in this work, namely the development of a reduced order model for this specific hysteretic system.

2.3 Reduced-order model

As noted above, Eq. (2.4) is not a system of ODEs. Galerkin projections do not seem feasible. To obtain lower order equations, we will use ideas of work and dissipation.

Let $\dot{x} = v$ in Eq. (2.4). We seek v for given values of x, $f(t)$ and $\dot{f}(t)$.

The rate of frictional dissipation cannot exceed the rate of work done by external forces minus the rate of increase of system potential energy. Therefore, $v^T b f(t) - v^T K x$ is the available dissipation budget, and $v^T \mu \operatorname{sgn}(\dot{x})$ is the dissipation rate. For slip to occur,

$$v^T \mu \operatorname{sgn}(v) + v^T K x - v^T b f(t) \leq 0. \tag{2.5}$$

If the inequality is strict, then there will be an instant of infinitely fast slip because the system has no inertia. For sustained slip at finite speeds under changing f, equality must hold in Eq. (2.5). In numerical work, we can minimize the left hand side of Eq. (2.5) with respect to unit-norm v and see if the minimum is negative; if it is, slip occurs in the direction of v.

We note that the quantity in Eq. (2.5) could be interpreted as a dissipation potential, with minor complications in that slip sometimes occurs and sometimes not. However, an exploration of the underlying theoretical and thermodynamic implications is not our goal here. We focus on model order reduction and refer the interested reader to, e.g., [28] and references therein.

To develop a reduced order model, we will need a set of basis vectors. For now, let

$$x = \Phi q \tag{2.6}$$

with $\Phi^T\Phi = I$, where the columns of Φ are yet to be chosen. We will have

$$v = \Phi\dot{q} = \Phi\eta$$

$$v^T v = \eta^T\Phi^T\Phi\eta = \eta^T\eta.$$

Substituting $x = \Phi q$ and $v = \Phi\eta$ into the left hand side of Eq. (2.5) gives

$$\eta^T\Phi^T\mu\,\mathrm{sgn}(\Phi\eta) + \eta^T(\Phi^T K\Phi)q - \eta^T(\Phi^T b)f(t). \tag{2.7}$$

We define

$$\eta^T\Phi^T\mu\,\mathrm{sgn}(\Phi\eta) = G(\eta), \quad \Phi^T K\Phi = \bar{K} \quad \text{and} \quad \Phi^T b = \bar{b}, \tag{2.8}$$

so that Eq. (2.7) becomes

$$G(\eta) + \eta^T(\bar{K}q - \bar{b}f(t)) = G(\eta) + \eta^T c, \tag{2.9}$$

where in turn

$$c = \bar{K}q - \bar{b}f(t). \tag{2.10}$$

Thus, our numerical approach will involve, at each time step, minimization of

$$G(\eta) + \eta^T c \tag{2.11}$$

with respect to η, subject to $\eta^T\eta = 1$, for a known vector c. A key point here is that the dimension of η equals the number of columns of Φ, and is much less than the $N = 500$ of the original model. However, $G(\eta)$ is complicated because of the signum of a high dimensional vector that appears within it (Eq. (2.8)).

2.3.1 Choice of basis vectors

We will choose our basis vectors via the singular value decomposition (also known as the proper orthogonal decomposition; [29]) applied to the full response x computed as described above. Here, the full model is 500 dimensional and the number of time steps is 1000. Starting from $t = 0$ to $t = 1000$, at each instant of time the responses at 500 locations are arranged row-wise. Hence, we obtain a 1000×500 response matrix x. We use Matlab function '`svd`' to obtain proper orthogonal modes and singular values[5] of x. Figure 2.6 shows the first twenty singular values of the response matrix x. The rapidly decaying singular values suggest that a low-dimensional description of the data is feasible: we used the first three singular vectors (or proper orthogonal modes) for our reduced order modeling. However, we found that small intervals

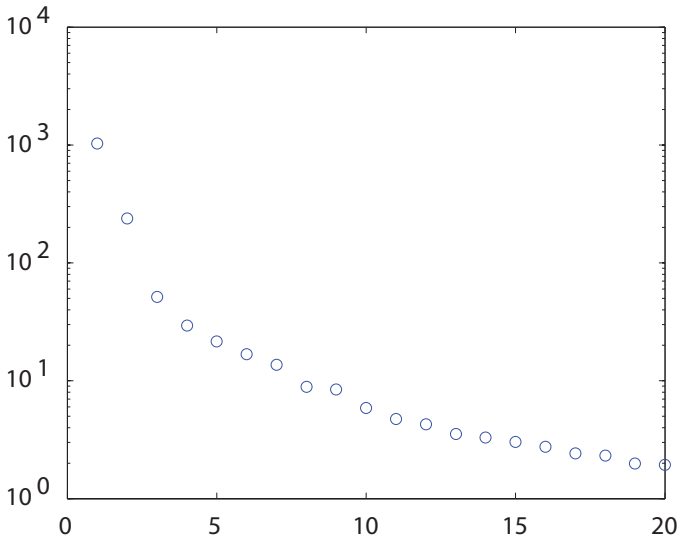

Figure 2.6: First twenty singular values of the response x.

of motion near turning points in the forcing require special attention for a good approximation. Accordingly, we also included three singular vectors corresponding to motions immediately following reversals in the forcing. We thus have six basis vectors; which we orthogonalize to obtain Φ.

[5]The Matlab command "`[u,s,v] = svd(x,0);`". '`s`' is a diagonal matrix of size 1000×500. Elements of '`s`' are the singular values. '`u`' and '`v`' are orthogonal matrices of sizes 1000×1000 and 500×500 respectively. Since response data are stacked row-wise, '`v`' is the matrix of modal coordinates.

2.3.2 Approximation of $G(\eta)$

A key step now is approximation of $G(\eta)$ of Eq. (2.11) by an analytically tractable, smooth function. We note that $G(\eta)$ is homogeneous of degree one in η, and consider (somewhat arbitrarily)

$$G(\eta) = \frac{(\eta^T A \eta)^\beta}{(\eta^T \eta)^{\beta - \frac{1}{2}}}. \tag{2.12}$$

Here A is a symmetric positive definite matrix, to be fitted along with the scalar parameter β. The fitting of A, for given β, can be simplified if we transform Eq. (2.12) to

$$\left(G(\eta) \cdot (\eta^T \eta)^{\beta - \frac{1}{2}} \right)^{\frac{1}{\beta}} = \eta^T A \eta. \tag{2.13}$$

We proceed as follows. First, β is chosen. Then a large number (we used one million) of random vectors η are generated, *not* of unit norm (we took the elements to be normally distributed with zero mean and unit variance). Since μ and Φ are known, the left hand side can be evaluated for each η. The right hand side is *linear* in the elements of A. A is 6×6 in our case, but is symmetric; so it has 21 independent elements. Thus, we get one million simultaneous equations in 21 variables (an overdetermined system). Solving these in a least squares sense gives an estimate for A for the chosen β.

We estimate A in this way for several values of β; and in each case we compute the sum of squares of the error computed from Eq. (2.12), i.e., the sum of squares of

$$G(\eta) - \frac{(\eta^T A \eta)^\beta}{(\eta^T \eta)^{\beta - \frac{1}{2}}}.$$

That sum of squares is divided by the sum of squares of $G(\eta)$, in order to obtain an overall measure of the error in the fit. The result, plotted against β, is shown in Figure 2.7. We find that the error is reasonably small, and $\beta = 0.5$ is a good choice because it is analytically most convenient.

Thus, we replace Eq. (2.12) with

$$G(\eta) \approx (\eta^T A \eta)^{\frac{1}{2}}, \tag{2.14}$$

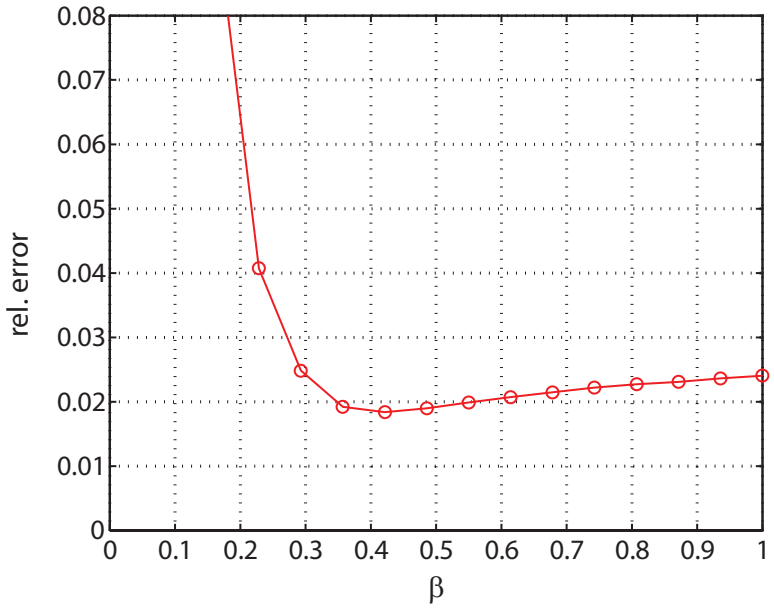

Figure 2.7: Relative error vs. β.

where we have emphasized that we have an approximate fit and not an exact match.

Since Eq. (2.14) introduces an *ad hoc* approximation, we can no longer expect our reduced order model to get better and better as we include more basis vectors in Φ. However, the approximation seems unavoidable to us.

2.3.3 Slip direction

The slip direction η minimizes $G(\eta) + \eta^T c$ subject to $\eta^T \eta = 1$. The minimization involves a few small tricks, as outlined below, but is equivalent to finding the roots of a polynomial. This means that the minimum can always be found unequivocally using standard methods.

Introducing a Lagrange multiplier for the constraint, we first set the gradient of $G(\eta) + \eta^T c - \lambda \eta^T \eta$ with respect to η to zero:

$$\frac{\partial}{\partial \eta} \left\{ \sqrt{\eta^T A \eta} + \eta^T c - \lambda \eta^T \eta \right\} = 0,$$

or

$$\frac{1}{\sqrt{\eta^T A \eta}} A\eta + c - 2\lambda\eta = 0.$$

Letting $2\lambda = \bar{\lambda}$,

$$\frac{1}{\sqrt{\eta^T A \eta}} A\eta - \bar{\lambda}\eta + c = 0. \tag{2.15}$$

A is now factored using $AQ = Q\Lambda$, where Q is an orthogonal matrix of eigenvectors and Λ is a diagonal matrix of eigenvalues.

Let

$$\eta = Qw. \tag{2.16}$$

Equation (2.15) gives

$$\frac{\Lambda}{\sqrt{w^T \Lambda w}} w - \bar{\lambda} w + Q^T c = 0. \tag{2.17}$$

Let $Q^T c = \bar{c}$ and $\dfrac{1}{\sqrt{w^T \Lambda w}} = \gamma$. Then,

$$\left(\gamma\Lambda - \bar{\lambda} I\right) w = -\bar{c}.$$

Since $\bar{\lambda}$ has no special significance, we let $\bar{\lambda} = \gamma\hat{\lambda}$ to obtain

$$\gamma(\Lambda - \hat{\lambda} I) w = -\bar{c}.$$

Hence,

$$w_i = \frac{1}{\gamma} \frac{\bar{c}_i}{(\hat{\lambda} - \Lambda_i)} \tag{2.18}$$

Now, $\eta^T \eta = 1$ gives $w^T Q^T Q w = w^T w = 1$. Accordingly,

$$w_i^2 = \frac{1}{\gamma^2} \frac{{\bar{c}_i}^2}{(\hat{\lambda} - \Lambda_i)^2}. \tag{2.19}$$

Multiplying both sides by Λ_i and adding gives

$$\sum_i w_i^2 \Lambda_i = \frac{1}{\gamma^2} \sum_i \frac{{\bar{c}_i}^2 \Lambda_i}{(\hat{\lambda} - \Lambda_i)^2}.$$

By definition of γ,

$$\frac{1}{\gamma^2} = \sum_i w_i^2 \Lambda_i,$$

so

$$\sum_i \frac{\bar{c_i}^2 \Lambda_i}{(\hat{\lambda} - \Lambda_i)^2} = 1. \tag{2.20}$$

Equation (2.20) must be solved for $\hat{\lambda}$. Assuming that the $\bar{c_i}$ are not all zero, it must have at least two real roots. To see this, note that, as $\hat{\lambda}$ approaches the eigenvalues of A (Λ_i, all real and positive), the left hand side must go to infinity (i.e., have a pole) wherever the corresponding $\bar{c_i} \neq 0$. However, to the right of the rightmost pole, the left hand side of Eq. (2.20) goes to zero as $\hat{\lambda} \to \infty$; and so it must equal 1 for some real $\hat{\lambda}$ to the right of the rightmost pole. By similar arguments, there must be a real solution to the left of the leftmost pole. There may be other real solutions, occurring in pairs, between poles.

To solve Eq. (2.20), we combine the terms on the left hand side by multiplying the individual denominators into a common denominator; and then we cross multiply with that common denominator to get a polynomial equation in $\hat{\lambda}$ of order $2n$, where n is the size of A (as mentioned above, $n = 6$ for our reduced order model). The polynomial to be solved is

$$\sum_i \left(\bar{c_i}^2 \Lambda_i \cdot \prod_{j \neq i} (\hat{\lambda} - \Lambda_j)^2 \right) = \prod_i (\hat{\lambda} - \Lambda_i)^2.$$

Computation of the coefficients of the polynomial, as well as finding its roots, can both be done numerically within Matlab; manual intervention is not required.

Solving Eq. (2.20) as above to find $\hat{\lambda}$, we retain only the real roots. For each such root, using $||w|| = 1$, Eq. (2.19) gives

$$\sum_i w_i^2 = \frac{1}{\gamma^2} \sum_i \frac{\bar{c_i}^2}{(\hat{\lambda} - \Lambda_i)^2} = 1,$$

whence we find

$$\gamma = \sqrt{\sum_i \frac{\bar{c_i}^2}{(\hat{\lambda} - \Lambda_i)^2}} \tag{2.21}$$

Eq. (2.21) gives γ for each real $\hat{\lambda}$. We can then find w using Eq. (2.18). Finally η is obtained from Eq. (2.16). Among the finite number of candidate η's thus obtained,

we choose the one which minimizes $\sqrt{\eta^T A \eta} + \eta^T c$.

In this way, given A and c (see Eq. (2.10)), we find the preferred slip direction η.

2.4 Reduced order model

The unit vector η found above gives the direction of slip, should slip occur. The rate of slip remains to be found. In this sense, we are guilty of a small abuse of notation in that η is no longer $\dot{q}$, but actually just gives the direction of $\dot{q}$.

There are two approximations involved so far. One is in the small number of basis vectors chosen in Φ (here, 6). The other is in the approximation of $G(\eta)$ in Eq. (2.14). The first approximation can be systematically improved by increasing the number of basis vectors retained. The second approximation is fortuitous, *ad hoc*, and not amenable to systematic improvement. We now wish to see the quality of approximations obtained.

Let $y = \sqrt{\eta^T A \eta} + \eta^T c$, where $c = \bar{K} q - \bar{b} f(t)$ and η is as found above. Recall that if $y < 0$, then slip should be infinitely fast; if $y > 0$ then slip should not occur; and if $y = 0$ then sustained finite-rate slip is possible. Given the approximations already made, within our goals of demonstrating a lower-dimensional model, and in the interest of simplicity, we adopt the following approximated evolution equation for the state q (recall Eq. (2.6)):

$$\frac{dq}{dt} = \text{gain} \cdot \eta \cdot |y|^p \cdot |\dot{f}| \cdot \{y < 0\}, \tag{2.22}$$

where "gain" is an arbitrary large positive multiplier (we used numbers in the range 1000-10000); p is a positive number (we used 1 or 1.2); the multiplier $|\dot{f}|$ makes the reduced system rate-independent; and the multiplier $\{y < 0\}$ is a logical variable (1 if the inequality holds, and 0 otherwise). The above evolution equation causes rapid slip if y is large and negative; little slip, if y is very small in magnitude; and (because of the large gain) finite-rate slip if y is negative and fairly small. Letting

the gain approach infinity would, in the limit, give us finite rate slip as $y \to 0^-$.

Equation (2.22) thus provides a reasonable approximation to the originally envisaged dynamics. In future work, a better numerical strategy may perhaps be developed, but this suffices for now.

For completeness, we report here the numerical values obtained for matrices A, $\bar{K}$ and $\bar{b}$ from the abovementioned calculations. The original μ, K, and b are now gone; these three matrices below define the reduced order model. The additional parameters "gain" and p of Eq. (2.22) are part of the numerical solution strategy, and not a part of the reduced model.

$$A = \begin{bmatrix} 69.7660 & -16.7609 & 5.0974 & -0.4140 & 6.0795 & 0.0735 \\ & 54.7643 & 21.1285 & -11.5050 & 9.9094 & 1.1897 \\ & & 53.1705 & 29.9240 & -1.0899 & 1.6273 \\ & \text{sym.} & & 60.6932 & 0.2900 & -1.1642 \\ & & & & 79.8739 & 0.7324 \\ & & & & & 83.5902 \end{bmatrix}, \tag{2.23}$$

$$\bar{K} = \begin{bmatrix} 0.3887 & 0.5313 & -0.1284 & 0.0080 & -0.0117 & 0.0328 \\ & 1.2884 & -0.5771 & -0.0405 & -0.3183 & 0.0362 \\ & & 1.3397 & -0.9649 & 0.1496 & 0.0970 \\ & \text{sym.} & & 1.4136 & 0.2534 & -0.1983 \\ & & & & 1.1416 & -0.2764 \\ & & & & & 1.1035 \end{bmatrix}, \tag{2.24}$$

$$\bar{b} = \left\{ \begin{array}{c} -25.6657 \\ -25.5468 \\ 8.7604 \\ -0.9557 \\ 1.6718 \\ 0.1085 \end{array} \right\}. \tag{2.25}$$

All reduced order model simulations presented below are obtained using the matrices given by Eqs. (2.23) through (2.25). These matrices represent the fitted parameters in a 6-state model that approximates the original 500-state system. Admittedly, the number of fitted parameters is large ($21 + 21 + 6 = 48$ for A, $\bar{K}$, and $\bar{b}$, respectively). By a further coordinate transformation that diagonalizes $\bar{K}$ we can transform the reduced model to an equivalent one with fewer parameters ($21+6+6 = 33$), but we avoid that additional step for brevity in presentation. Our main goal here has been systematic model order reduction, which has been achieved; and our hope is that this reduced model, in turn, provides insights that lead to more compact reduced-order hysteresis models with fewer parameters in future.

2.4.1 Summary

Our reduced-order model is now summarized. Given A, $\bar{K}$, $\bar{b}$ matrices (Eqs. (2.23) through (2.25)) and forcing $f(t)$ and current state q, we find an η that minimizes

$$\min_{||\eta||=1} \sqrt{\eta^T A \eta} + \eta^T (\bar{K} q - \bar{b} f).$$

For that η, we find

$$y = \sqrt{\eta^T A \eta} + \eta^T (\bar{K} q - \bar{b} f).$$

Then, we solve

$$\frac{dq}{dt} = \text{gain} \cdot \eta \cdot |y|^p \cdot |\dot{f}| \cdot \{y < 0\},$$

Table 2.1: Load cases with varying amplitude.

Case	Forcing (f)
1	$0.4\,\sin(t) + \sin(4.16753\,t)$
2	$\sin(t) + 0.4\,\sin(4.16753\,t)$
3	$\sin(t) + 1.5\,\sin(4.16753\,t)$
4	$1.5\,\sin(t) + \sin(4.16753\,t)$
5	$\sin(t) + 3.0\,\sin(4.16753\,t)$
6	$3.0\,\sin(t) + \sin(4.16753\,t)$

Table 2.2: Load cases with varying frequency.

Case	Forcing (f)
1	$\sin(t) + 1.5\,\sin\left(\frac{\pi}{4}t\right)$
2	$\sin(t) + 1.5\,\sin\left(\frac{\pi}{2}t\right)$
3	$\sin(t) + 1.5\,\sin\left(\pi\,t\right)$
4	$\sin(t) + 1.5\,\sin\left(\frac{5\pi}{4}t\right)$
5	$\sin(t) + 1.5\,\sin\left(\frac{3\pi}{2}t\right)$
6	$\sin(t) + 1.5\,\sin\left(2\pi\,t\right)$

where 'gain' is a large multiplier (we used values between 1000-10000) and p is a somewhat arbitrary positive parameter (we used values between 1-1.2).

We now present numerical results obtained using this reduced-order model.

2.5 Results

All our simulations of the full model given below were conducted using the LCP formulation described earlier; and all simulations of the reduced model were done using Eq. (2.22). Since Eq. (2.22) is a stiff system, we used '`ode15s`' (a stiff system solver) in Matlab. Tables 2.1 and 2.2 show the forcing histories ($f(t)$) used. Since the system response is rate-independent, the actual waveforms within f are irrelevant; only the turning points or rate reversals matter. In the forcing histories considered, we include a fixed pair of frequencies with different relative amplitudes (Table 2.1), as well as different pairs of frequencies with a fixed set of amplitudes (Table 2.2).

Figure 2.8 shows the solutions obtained for the forcing histories in Table 2.1. In

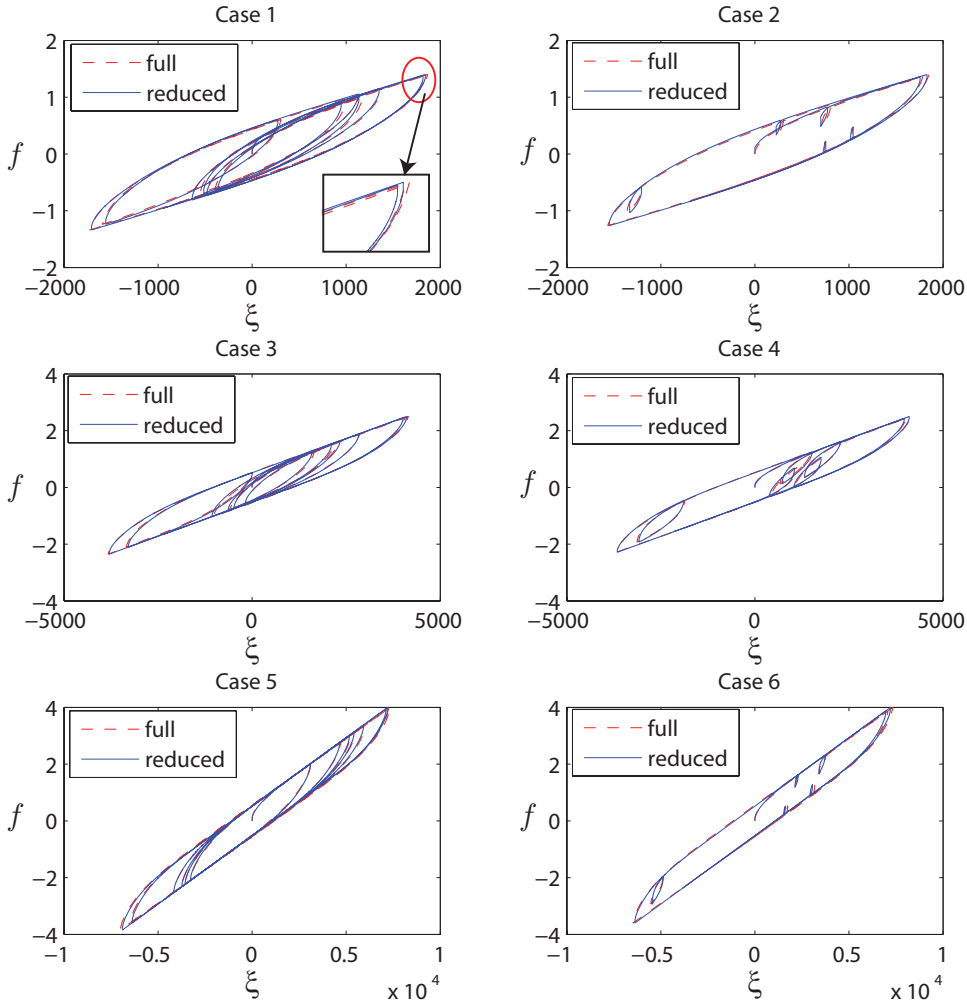

Figure 2.8: Hysteresis curves for the forcing histories in Table 2.1.

these plots, f was a known input for both full and reduced simulations. The generalized displacement ξ was taken to be $b^T x$ for the full simulation, and $\bar{b}^T q$ for the reduced simulation. It is seen that for a variety of combinations of forcing amplitudes, with small and large unloading loops, the reduced model does an excellent job of approximating the full system. A small issue in simulations of the reduced order model is that we cannot start[6] with both $q = 0$ and $f = 0$, and so the simulations were started with extremely small nonzero initial conditions for q.

Similarly, Figure 2.9 shows results for the forcing histories in Table 2.2. It is seen that changing the frequency combinations has no significant effect: the match remains good overall.

[6]See the lines following Eq. (2.20). If both $q = 0$ and $f = 0$, then $c = 0$, and thence $\bar{c}_i = 0$ for each i.

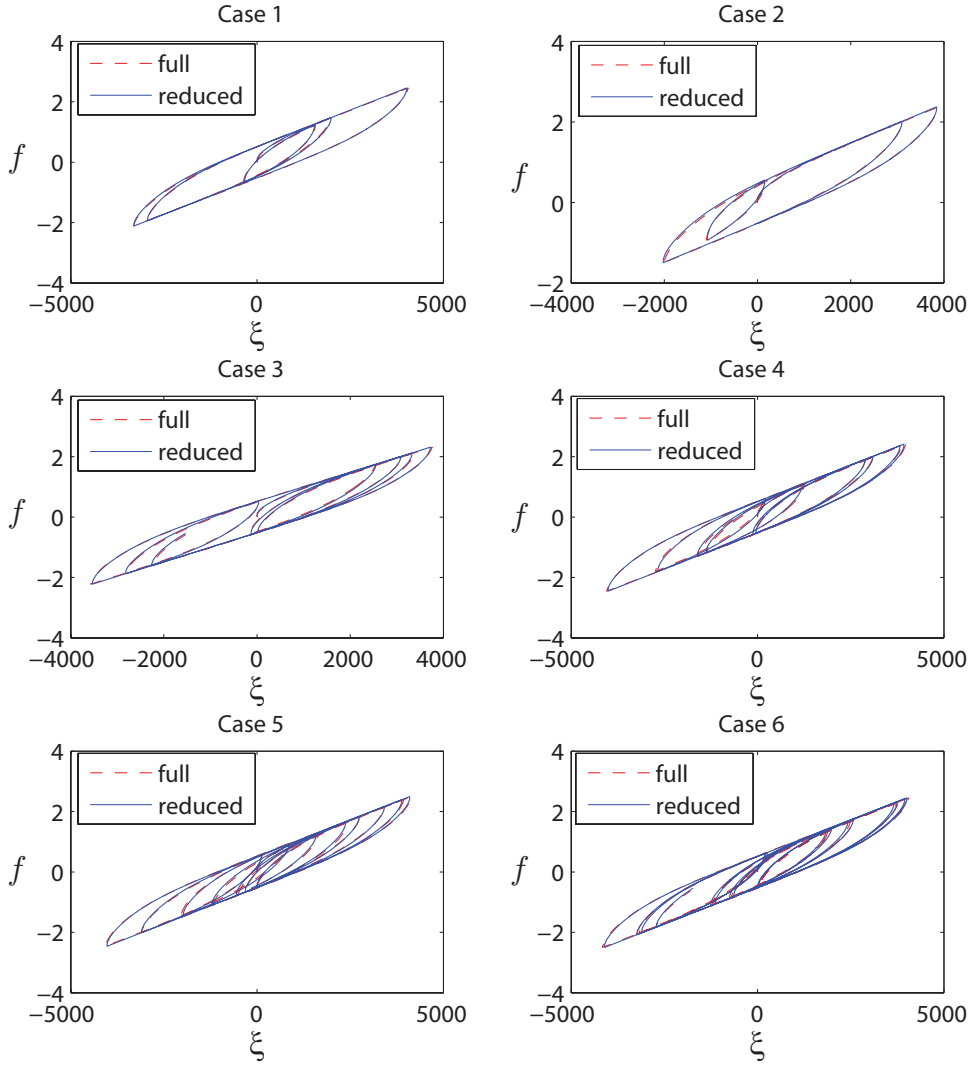

Figure 2.9: Hysteresis curves for the forcing histories in Table 2.2.

A minor flaw remains in the reduced model solutions. At points of load reversal, there is a brief interval of sticking (no slip, seen as a small vertical portion in the hysteresis plot) in the reduced model, which is negligibly small in the full model. This error does not visibly decrease even if, say, the 6-state reduced model is changed to an 8-state reduced model. The error appears to be due to the error in approximating $G(\eta)$ above. However, for a large set of forcing histories, this error is slight. Overall, the minor loops are captured well; recall that the Bouc-Wen model does not capture such loops at all.

2.6 Concluding remarks

Our primary aim in the work so far has been to systematically derive a reduced order hysteresis model from a high-dimensional frictional system. Such an approach allows access to all internal states, and we hope that it will yield insights into hysteretic phenomena in general and lead to more compact and easy to use hysteresis models in subsequent work.

The model we have studied so far shows hysteresis including major and minor loops. Such minor loops cannot be captured by the popular Bouc-Wen model. They can be captured by the Preisach model, but that model is very different from ours in both structure and function. Thus, our main contribution in this chapter lies in the reduction of a high-dimensional hysteretic system into a few explicit evolution equations. Our success has depended on a serendipitous *ad hoc* approximation of the function $G(\eta)$, as well as on being able to solve a minimization problem involving this same function. We are not aware of similar approximations made elsewhere.

However, at this stage, our reduced model remains somewhat complicated. It has three fitted matrices, and the evolution rate involves evaluation of a slightly complicated matrix function which includes root finding of polynomials. Additionally, our numerical solution procedure leads to a stiff system. These difficulties suggest that smaller empirical models must still be sought, for efficient simulation of dynamical systems involving hysteretic elements. Yet, our results may provide insights that aid in such a search. The next chapter will simplify and improve our approach, making it more competitive for routine computational applications.

Chapter 3

A two-state hysteresis model from high-dimensional friction

In this chapter, we follow up on our work of chapter 2. Here, we use a more intuitively appealing high-dimensional frictional system that resembles one studied earlier by Iwan [10, 11]. From that high-dimensional system, a reduced order model with just two states and six parameters is derived that allows parameter fitting to match given data. The material of this chapter has been published in [32].

3.1 Introduction

In this chapter we follow up on our work on low-dimensional modeling of frictional hysteresis in chapter 2. Contributions of the present chapter include a different underlying frictional model with greater intuitive appeal, new analytical insights, reduction in the number of states from six to two[1], reduction in the number of free parameters by an order of magnitude, and demonstration of fitting these parameters to several hypothetical hysteresis loops. The net result is a two state hysteresis model that captures minor loops under small reversals within larger load paths, and is ready for practical numerical implementation (simple Matlab code is provided).

[1] Two is the theoretical minimum number. Single state models cannot capture commonly observed behavior. See Figure 2.2.

For elementary background, we note that hysteresis is a largely rate-independent, irreversible phenomenon that occurs in many systems. Much research on hysteresis has been done over several decades: see, e.g., [1] and the many references therein. For classical papers see e.g., Ewing [2], Rowett [3], Preisach [4], Jiles & Atherton [33]. For our present purposes, for hysteresis in mechanical systems with elastic storage and frictional dissipation, a model due to Iwan [10, 11] seems promising, but is high-dimensional and deeply nonlinear with several dry friction elements. In contrast, the famous Bouc-Wen model [7, 8] (see also [9]) is one-dimensional but fails to form minor loops under small reversals within larger load paths.

With this background, we studied in chapter 2 a frictional hysteretic system given by (recall Eq. (2.4))

$$\mu \operatorname{sgn}(\dot{x}) + Kx = bf(t), \tag{3.1}$$

where x is high-dimensional; μ is diagonal; K is symmetric and positive definite; b is a column matrix; $f(t)$ is scalar and differentiable; and the *signum* function 'sgn' is defined elementwise as follows:

$$\operatorname{sgn}(u) \begin{cases} = +1, & u > 0, \\ = -1, & u < 0, \\ \in [-1, 1], & u = 0. \end{cases}$$

Equation (3.1) can be solved incrementally *via* a linear complementarity problem or LCP [25] or, less efficiently, using other means as described later. The solution of Eq. (3.1) captures important aspects of hysteresis including formation of minor loops. From Eq. (3.1), we had developed a reduced order model with six states. The order reduction included finding the slip direction as a minimizer of a complicated function containing many *signum* nonlinearities, for which a convenient analytical approximation was found. However, some shortcomings remained. The choice of basis vectors involved some arbitrariness whose implications were unclear; reductions

below sixth order gave poor results; and there were too many fitted parameters for practical use.

In light of the above, the present chapter makes the following notable progress. A more intuitively appealing frictional system is studied here, motivated by the Iwan model [10], and yielding a simpler governing equation. The numerically obtained basis vectors are now amenable to analytical approximation, providing better analytical insight. Finally, a two state, reduced order model is derived that allows practical parameter fitting to match a range of given data.

As far as we know, the two state model developed here has no parallel in the literature.

3.2 New frictional system

Differing somewhat from the high-dimensional model in Figure 2.3, here we consider the intuitively simpler high-dimensional frictional system sketched in Figure 3.1. In

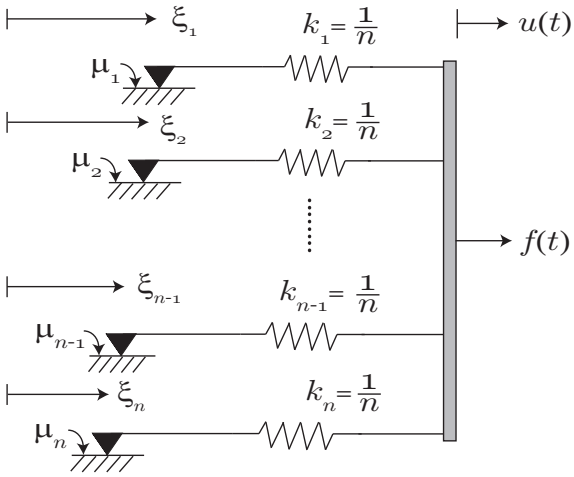

Figure 3.1: A new high-dimensional frictional system.

this n-dimensional model (with n large), each spring has stiffness $\frac{1}{n}$, and friction coefficients at the slip sites are

$$\mu_1 = \frac{\mu_0}{n}, \mu_2 = \frac{2\mu_0}{n}, \cdots, \mu_n = \frac{n\mu_0}{n} = \mu_0.$$

As indicated in the figure, $u(t)$ is a displacement input to the system, for which a force $f(t)$ is needed. Friction forces at the slip sites are written as

$$F_1 = -\mu_1 \mathrm{sgn}(\dot{\xi}_1), F_2 = -\mu_2 \mathrm{sgn}(\dot{\xi}_2), \cdots, F_n = -\mu_n \mathrm{sgn}(\dot{\xi}_n),$$

where the overdot denotes a time derivative and the *signum* function is understood to be multivalued at zero (taking any necessary value between ± 1). The governing equation is

$$\mu_j \,\mathrm{sgn}(\dot{\xi}_j) + \frac{1}{n}\,\xi_j = \frac{1}{n}\,u(t), \quad j = 1, \cdots, n$$

In matrix form

$$\mu \,\mathrm{sgn}(\dot{\xi}) + K\xi = bu(t), \tag{3.2}$$

which resembles Eq. (3.1) but is in fact simpler because the elements of μ now have a regular variation (they are linearly increasing), K is a scalar multiple of the identity matrix, and all elements of b are identical. The output force $f(t)$ is

$$f(t) = \sum_{j=1}^{n} k_j \left(u(t) - \xi_j\right) = u(t) - \frac{1}{n}\sum_{j=1}^{n} \xi_j. \tag{3.3}$$

Incidentally, if a spring of stiffness k_s is attached to the system, in parallel, being stretched by $u(t)$, then the net output force is

$$f(t) = (1 + k_s)u(t) - \frac{1}{n}\sum_{j=1}^{n} \xi_j. \tag{3.4}$$

We will use the parameter k_s later for better fitting of the model to specified hysteretic response curves; here, we note that k_s in Eq. (3.4) has no effect on the solution of Eq. (3.2), which takes $u(t)$ as its input.

We solve Eq. (3.2) incrementally by casting it first into an LCP (as described in Appendix A) and then using Lemke's algorithm (as implemented by Miranda & Fackler [26]). There is in fact a large literature on solving friction problems using the LCP; readers interested in the theory may consult, e.g., Klarbring and Pang

[34].

Alternatively, Eq. (3.2) may be regularized as follows:

$$\dot{\xi} = \mathrm{sgn}(b\,u - K\xi)\ \cdot \exp\left(\frac{|\mu^{-1}(b\,u - K\xi)| - 1}{\epsilon}\right), \quad 0 < \epsilon \ll 1. \tag{3.5}$$

In the above the exponential, the absolute value within it, and the signum function are all evaluated elementwise; the fact that K is a scalar multiple of the identity and that μ is diagonal has been used to simplify the first term; and ϵ is a regularizing parameter. The justification for this regularizing method is that (i) the exponential term produces high rates of change only when the concerned absolute value exceeds unity, and (ii) the signum term outside guides that rate of change in the correct direction. Further discussion of this regularizing method is avoided to minimize the distraction from the main flow of the work, but a numerical example is given in Appendix B. Note that Eq. (3.5) may be solved using an ODE solver.

For our numerical solution, the arbitrarily selected numerical parameters are as follows. We use $n = 500$, $\mu_0 = 0.002$, and the two-frequency displacement input

$$u(t) = 0.6748\ \sin(t) + 0.2887\ \sin(6.5581\,t). \tag{3.6}$$

We then solve Eq. (3.2) incrementally using 12000 uniform time steps of $dt = 0.001$ each.

In this way, we obtain a 12000×500 matrix, wherein each row is ξ^T at some instant. From ξ, we find f using Eq. (3.3). Figure 3.2 shows $f(t)$ against $u(t)$. Minor loops are seen. As emphasized in chapter 2, such minor loops are not predicted by the Bouc-Wen model or indeed any hysteresis model with a single state.

We now develop a reduced order model from this high-dimensional hysteretic system (Figure 3.1, Eq. (3.2)).

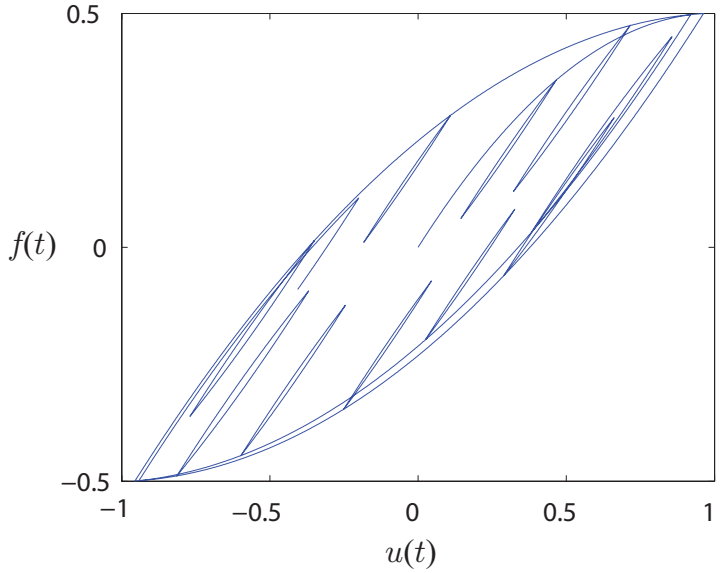

Figure 3.2: Hysteresis curve obtained for the 500 dimensional frictional system with $u(t)$ as in Eq. (3.6). Note the minor loops, as mentioned in section 3.1.

3.3 Reduced-order model

Our system is discrete. However, the largeness of n and the slow variation in μ_j suggests that we might loosely think of it as an approximation of a continuous system. With this motivation, we assume

$$\xi_j \approx \sum_{r=1}^{m} q_r(t)\phi_r(x_j), \quad x_1 = 1, x_2 = 2, \cdots . \tag{3.7}$$

In the above, m is the reduced dimension, $q_r(t)$'s are functions of time, and the $\phi_r(x)$'s are basis functions yet to be chosen.

3.3.1 Choice of basis functions

The singular value decomposition of the 12000×500 data matrix from section 3.2 shows that the first 2 singular values are distinctly larger than the rest: see Figure 3.3. Figure 3.4 (left) shows the first three singular vectors plotted against $x^{\frac{3}{2}}$ (where $x = 1, 2, \cdots, 500$) for two different solutions using different μ_0's and $u(t)$'s. The same figure (right) shows that, after rescaling, the singular vectors for the two cases are similar. These observations suggest that the basis functions may be taken

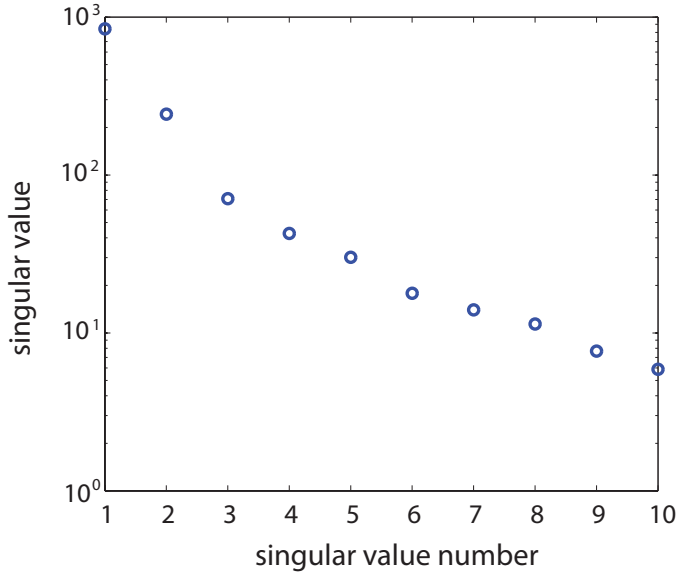

Figure 3.3: First ten singular values of ξ.

as functions of $x^{\frac{3}{2}}$ (the 3/2 power is empirical, based on the fact that the slope near zero is finite and nonzero). In order to ensure eventual decay to zero, we choose the following basis functions for lower order modeling:

$$\phi_r(x) = \exp\left(-\alpha x^{\frac{3}{2}}\right) \cdot \left(x^{\frac{3}{2}}\right)^{r-1}, \quad r = 1, \cdots, m \tag{3.8}$$

The free parameter $\alpha > 0$ controls the decay rate of the basis functions. The actual discrete versions of these basis functions will be orthonormalized below for analytical convenience.

It may be noted that the *ad hoc* form of Eq. (3.8) leads to simplification below, but also means that the possibility of a very good match with the full numerical solution has now been abandoned.

3.3.2 Slip criterion

Our *slip criterion* is this: slip cannot occur if the accompanying frictional dissipation exceeds the external work input minus the internal increase in potential energy. This criterion will help us find slip directions and rates below.

What follows in sections 3.3.2 through 3.3.4 has much in common with chapter

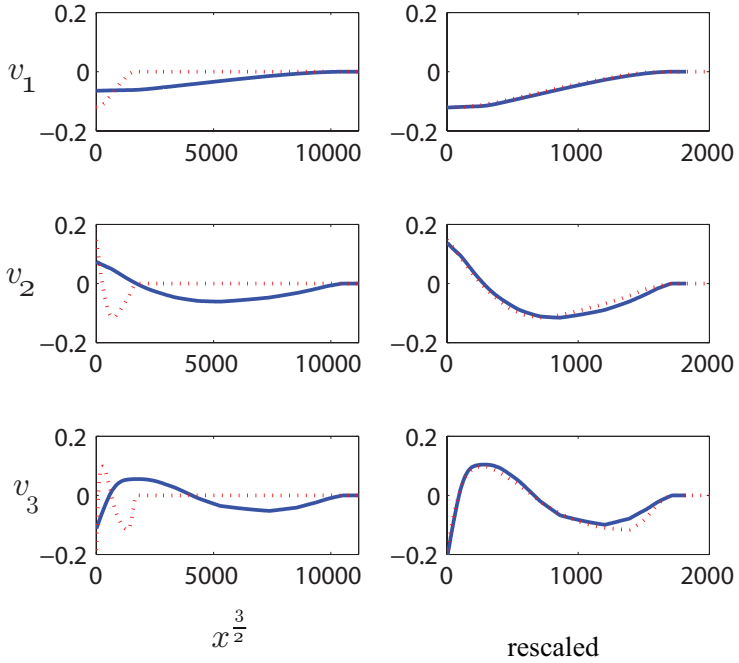

Figure 3.4: Left: First three singular vectors plotted against $x^{\frac{3}{2}}$ (the 3/2 power is empirical, based on the fact that the slope near zero is finite and nonzero). The blue solid curves are solutions for $\mu_0 = 0.002$ and $u(t)$ as in Eq. (3.6); the red dotted curves are solutions for $\mu_0 = 0.004$ and the different, also arbitrary, $u(t) = 0.4049\,\sin(t) + 0.1732\,\sin(4.5581\,t)$. Right: Singular vectors for the two cases (left) match fairly well after scaling horizontally and vertically.

2, but is included for completeness. Let

$$\xi \approx \Phi q$$

where the columns of Φ are basis vectors from Eq. (3.8), but orthonormalized so that $\Phi^T\Phi = I$. Then the slip rate vector

$$v \approx \Phi\dot{q} = \Phi\eta \text{ (say)}$$

with

$$v^T v = \eta^T\Phi^T\Phi\eta = \eta^T\eta.$$

The rate of frictional dissipation is

$$\sum_{j=1}^{n} |\dot{\xi}_j| \mu_j = \sum_{j=1}^{n} \dot{\xi}_j \mu_j \operatorname{sgn}(\dot{\xi}_j) = \eta^T \Phi^T \mu \operatorname{sgn}(\Phi\eta). \tag{3.9}$$

The rate of increase in spring potential energy is

$$\frac{d}{dt}\left(\sum_{j=1}^{n} \frac{1}{2n}(u-\xi_j)^2\right) = \frac{1}{n}\sum_{j=1}^{n}(\dot{u}-\dot{\xi}_j)(u-\xi_j) \tag{3.10}$$

and the rate of work done by the external force f is

$$\dot{u}\, f = \dot{u} \sum_{j=1}^{n} \frac{1}{n}(u-\xi_j). \tag{3.11}$$

Substituting the above into our slip criterion yields

$$\eta^T \Phi^T \mu \operatorname{sgn}(\Phi\eta) + \eta^T(\Phi^T K \Phi)q - \eta^T(\Phi^T b)u \leq 0, \tag{3.12}$$

with matrices μ, K and b as described in section 3.2. We define

$$\eta^T \Phi^T \mu \operatorname{sgn}(\Phi\eta) = G(\eta) \tag{3.13}$$

and

$$(\Phi^T K \Phi)q - (\Phi^T b)u = \bar{K}q - \bar{b}u = c, \tag{3.14}$$

so that inequality (3.12) becomes

$$G(\eta) + \eta^T c \leq 0. \tag{3.15}$$

We note that $\bar{K} = \dfrac{1}{n} I$ above, with I being the identity matrix; and choosing $n = 500$,

$$\bar{b} = \begin{Bmatrix} 0.0326 \\ 0.0068 \end{Bmatrix} \text{ and } \begin{Bmatrix} 0.0285 \\ 0.0059 \end{Bmatrix}$$

for $\alpha = 0.0008$ and $\alpha = 0.0012$ respectively. These values will be used later.

If the *minimum* possible value of the left hand side of inequality (3.15) is negative, rapid slip will occur because there is no inertia; if the minimum is positive, no slip can occur; and if it is zero over a time interval, sustained slip can occur at a finite rate.

Accordingly, we will minimize $G(\eta)+\eta^T c$ at each time step with respect to η, and see if the minimum is negative or positive. Noting that $G(\eta) + \eta^T c$ is homogeneous of degree one in η, our minimization will be done subject to $\eta^T\eta = 1$. The only difficulty is that $G(\eta)$ is a complicated function. Luckily, a convenient analytical approximation for $G(\eta)$ of Eq. (3.13) was found in section 2.3.2.

3.3.3 Approximation of $G(\eta)$

$G(\eta)$ is homogeneous of degree one in η. In section 2.3.2, a similar function was encountered and the following approximation was considered

$$G(\eta) \approx \frac{(\eta^T A\eta)^\beta}{(\eta^T\eta)^{\beta-0.5}}, \tag{3.16}$$

with A a fitted symmetric and positive definite matrix; also, $\beta = 0.5$ was found to be near-optimal and selected due to analytical convenience. We use the same approximation here (again with $\beta = 0.5$).

Fitting of the matrix A was described in detail in chapter 2. Here we fix $n = 500$, let μ_0 vary, and fit A for $\alpha = 0.0008$ and $\alpha = 0.0012$. We find that to an excellent approximation

$$A = \mu_0^2 \bar{A} \tag{3.17}$$

with

$$\bar{A} = \begin{bmatrix} 24.8170 & -10.0836 \\ -10.0836 & 6.2967 \end{bmatrix}$$

and

$$\bar{A} = \begin{bmatrix} 11.1372 & -4.5175 \\ -4.5175 & 2.8222 \end{bmatrix}$$

for $\alpha = 0.0008$ and $\alpha = 0.0012$ respectively. With A as above and $\beta = 0.5$, $G(\eta)$ has been approximated; we now turn to the slip direction.

3.3.4 Slip direction

The slip direction η minimizes $y = G(\eta) + \eta^T c$ for given

$$c = \frac{1}{n}\, q - \bar{b}u,$$

subject to $\eta^T \eta = 1$.

Introducing a Lagrange multiplier for the constraint, using the approximation $G(\eta) \approx \sqrt{\eta^T A \eta}$, taking the gradient with respect to η, and letting $2\lambda = \bar{\lambda}$, we obtain

$$\frac{1}{\sqrt{\eta^T A \eta}} A\eta - \bar{\lambda}\eta = -c. \tag{3.18}$$

The minimizing 2×1 matrix η is found by solving a 4×4 eigenvalue problem (see Appendix C). If the corresponding

$$y = \sqrt{\eta^T A \eta} + \eta^T c < 0, \tag{3.19}$$

then slip occurs in the direction of η.

3.3.5 Reduced order model using incremental map

The unit vector η (computed as outlined in Appendix C) gives the direction of slip, but the actual rate of slip $\dot{q}$ remains to be found. In chapter 2, we used a stiff system of ODEs with a large *ad hoc* gain parameter. Here, we use a faster explicit incremental formulation as follows.

During time increment Δt, let $\Delta q = \eta \Delta s$ for some $\Delta s \geq 0$. Holding η fixed

during the time increment, we find from Eqs. (3.19) and (3.14)

$$\Delta y = \eta^T \Delta c = \eta^T \left(\bar{K} \Delta q - \bar{b} \Delta u \right). \tag{3.20}$$

It follows that

$$y + \Delta y = \sqrt{\eta^T A \eta} + \eta^T c + \eta^T (\bar{K} \eta \Delta s - \bar{b} \Delta u). \tag{3.21}$$

Equation (3.21) gives a linear relationship between the unknowns Δs and $y + \Delta y$ (with all other things including Δu being known). The unknowns satisfy the linear complementarity conditions

$$\Delta s \geq 0, \quad y + \Delta y \geq 0, \quad \Delta s \cdot (y + \Delta y) = 0. \tag{3.22}$$

Solving[2] Eqs. (3.21) and (3.22) yields Δs, which in turn gives the increment in q through

$$q(t + \Delta t) = q(t) + \eta \Delta s. \tag{3.23}$$

The output force $f(t)$, from Eqs. (3.3), (3.4) and (3.7), is

$$f(t) = (1 + k_s) u(t) - q^T \bar{b}. \tag{3.24}$$

Figure 3.5 shows results for $u(t)$ as in Eq. (3.6), and with $k_s = 0$. We used $n = 500$, $\mu_0 = 0.002$, and $\alpha = 0.0008$ and 0.0012. Both solutions capture minor loops. The hysteresis loops obtained depend on the parameter α.

As mentioned earlier, a direct comparison of these results with the earlier high-dimensional simulation is not meaningful because we have adopted analytical expressions for the basis functions (Eq. (3.8)) instead of numerically computed proper orthogonal modes from actual solutions (Figure 3.4). The high-dimensional model has thus motivated the structure of the lower dimensional model, and now we work directly with the latter.

[2]Since Δs and y are scalars, these equations can be solved easily, and LCP code is not needed.

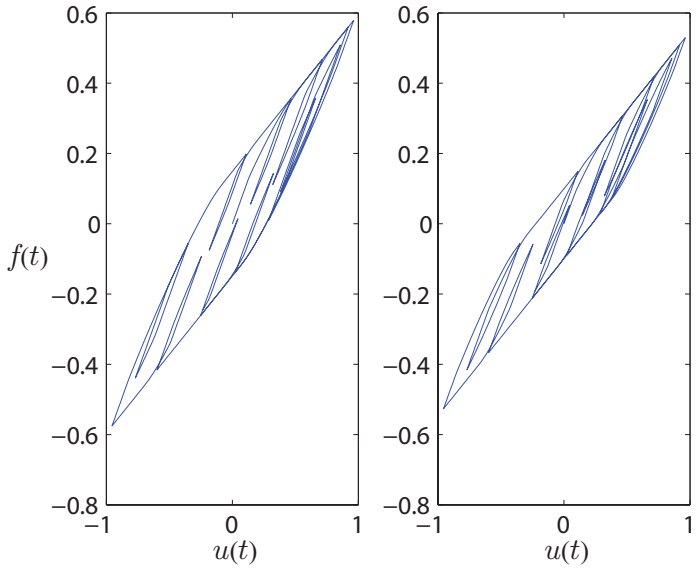

Figure 3.5: Hysteresis curves for $u(t)$ as in Eq. (3.6). Left: $\alpha = 0.0008$. Right: $\alpha = 0.0012$.

3.3.6 Final reduced order model using a differential equation

Although the numerical results that follow were obtained using the incremental map given above, some users may prefer to have a differential equation for the hysteresis model. We now present one. We also present the entire hysteresis model compactly and algorithmically below. A detailed example calculation is given in Appendix D.

The quantities assumed given are:

1 System matrices. These are:

(i) An $m \times m$ symmetric and positive definite matrix A (we have been working with $m = 2$). Since A can be diagonalized by an orthogonal coordinate transformation, for compactness we henceforth assume that A is diagonal, with elements in increasing order. In the $m = 2$ case, we introduce a scalar factor $\bar{\mu} > 0$ to write

$$A = \bar{\mu} \begin{bmatrix} \sigma & 0 \\ 0 & 1 \end{bmatrix}, \quad 0 < \sigma < 1.$$

(ii) A matrix $\bar{K}$, which is a scalar multiple of the identity. Here

$$\bar{K} = \bar{\alpha} \begin{bmatrix} 1 & 0 \\ 0 & 1 \end{bmatrix}, \quad \bar{\alpha} > 0.$$

(iii) An $m \times 1$ column matrix $\bar{b}$. Here

$$\bar{b} = \begin{Bmatrix} \bar{b}_1 \\ \bar{b}_2 \end{Bmatrix}.$$

2 System inputs: u is the system input, and $\dot{u}$ is known at each instant.

3 The state vector: q is an $m \times 1$ state vector (here $m = 2$).

Given the above system matrices and inputs, we first compute $c = \bar{K}q - \bar{b}\,u$. Subsequently, the possible slip direction η is computed as a function of A and c as described in Appendix C, using straightforward matrix calculations of order $2m$.

Using the above, we define the intermediate quantity[3]

$$\dot{s} = \left[\frac{\eta^T \bar{b}}{\eta^T \bar{K} \eta}\, \dot{u} - My\,|\dot{u}| \right] \cdot \{y \leq 0\}, \tag{3.25}$$

where M is a user-defined positive number (we have used $M = 1$ with good results); and where $\{y \leq 0\}$ is a logical variable (1 if the condition holds, and 0 otherwise).

Finally, recalling Eq. (3.22), we write

$$\dot{q} = \eta\, \dot{s} \cdot \{\dot{s} > 0\}, \tag{3.26}$$

where $\{\dot{s} > 0\}$ is a logical variable as above (1 if the condition holds, and 0 otherwise). At this point, starting from the state matrices, the inputs u and $\dot{u}$, and the state vector q, we have computed $\dot{q}$.

[3]The way $\dot{s}$ is defined ensures that if $y > 0$, then $\dot{s} = 0$; and otherwise, the first term inside the square brackets maintains $\dot{y} = 0$ (see Eq. (3.21)) while the second term drives y from any negative values it takes during simulation toward zero. Since the $-My$ term is a small stabilizing correction, M does not need to be very large.

The above system of ODEs does not need a large *ad hoc* 'gain' parameter as was used in chapter 2.

3.4 Fitting parameters to given data

As described in section 3.3.6, for a two state model we have 5 fitted parameters ($\bar{\mu}$, σ, $\bar{\alpha}$, $\bar{b}_1$ and $\bar{b}_2$). If we used a three state model, we would add one diagonal entry in A, no new parameters to $\bar{K}$, and one element to $\bar{b}$, obtaining a model with 7 fitted parameters.

Introduction of an added spring in parallel with constant k_s, as in Eq. (3.4), would make it 6 fitted parameters for the two-state model and 8 fitted parameters for the three state model. For clarifying that a spring in parallel is implied, we will refer to these latter two as $5+1$ and $7+1$ respectively.

We now fit some hypothetical hysteresis loops using our two state, 5+1 parameter model, using nonlinear least squares as depicted schematically in Figure 3.6 (the minimization was done using Matlab's built-in function `fminsearch`).

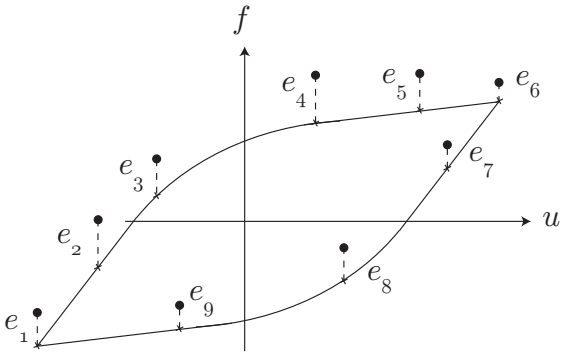

Figure 3.6: Fitting a hysteresis curve. Dotted points represent given data. Vertical distances between data and fitted curve are squared and added. That sum is minimized with respect to the fitted parameters.

3.5 Results and discussion

We now show results of fitting the hysteresis model to some arbitrary input data. Results are depicted graphically here; numerical values of fitted parameters are given

in Appendix E.

Figure 3.7 shows fitting of three hysteresis loops, numbered 1 through 3. Each case is depicted in three parts, namely (a), (b) and (c). Parts 1(a) through 3(a) show the prescribed or desired loop shapes (half the cycle). Parts 1(b) through 3(b) show the corresponding hysteresis loops obtained by fitting parameters. These fitted parameters are then used to plot hysteresis loops using smaller (85% and 70%) input amplitudes, and parts 1(c) through 3(c) show these loops corresponding to 100% (blue solid), 85% (black dotted) and 70% (red dashed) amplitude.

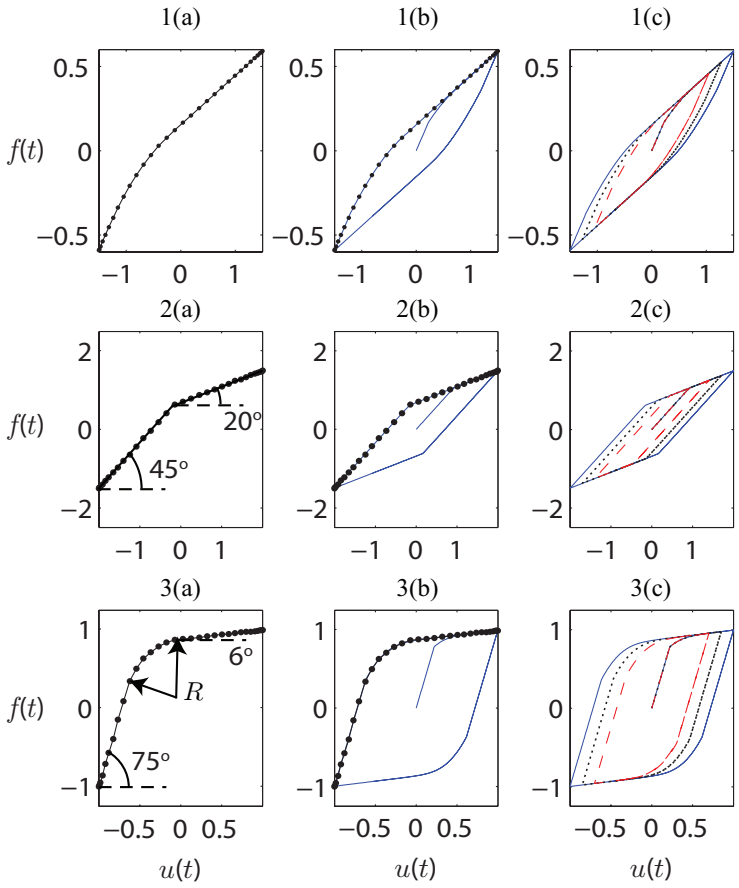

Figure 3.7: Fitting of hysteresis loops. Part (a): prescribed hysteretic shape (only half of the cycle). Part(b) corresponding fitted hysteresis loop. Part (c) fitted hysteresis loop (blue solid) along with two hysteresis loops corresponding to 85% (black dotted) and 70% (red dashed) of the amplitude.

The model fits the above given data (Figure 3.7) well. However, the model does not work well for hysteresis curves with two distinct changes of slope. For example, Figure 3.8 shows how a hysteresis curve made of three straight lines is not captured

very accurately by the 2-state model (or even, in attempts not documented here, by models with 3 or 4 states). However, overall, our model fits a reasonable range of data usefully well.

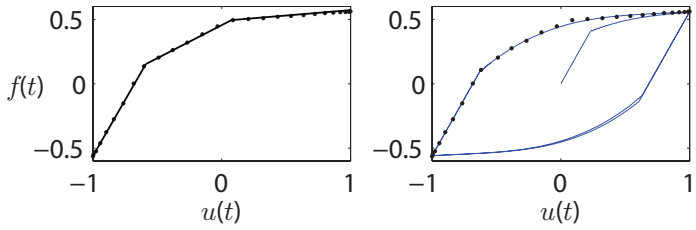

Figure 3.8: Left: given data, made of three straight lines. Right: corresponding fitted hysteresis loop. The model apparently cannot capture two sharp slope changes.

In Figure 3.9, we consider fitting of minor loops. In case 1(a), we specify two minor loops within a major loop. The corresponding fit is shown in 1(b). In case 2(a), we try to thicken one of minor loops of case 1(a). The model captures the loop thickening in the third quadrant of the plot, but similar changes occur in the first quadrant as well, because our hysteresis loops are symmetrical about the origin.

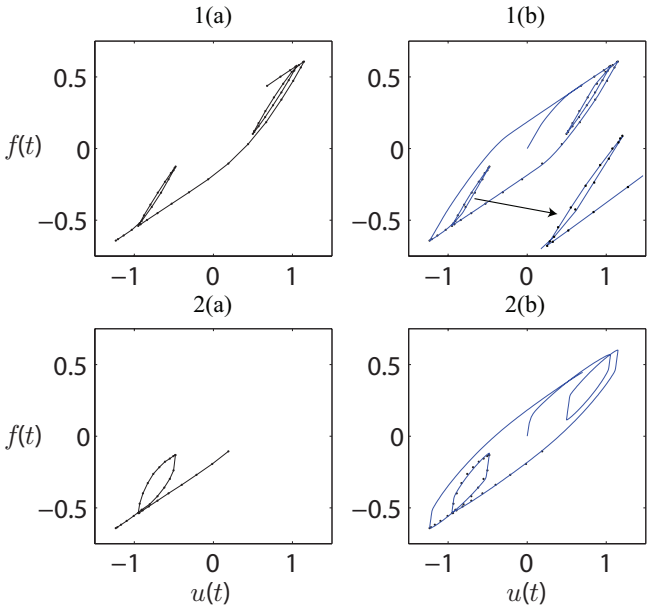

Figure 3.9: Left: given data for hysteresis loops with minor loops. Right: corresponding fitted hysteresis loops. Case 1(a): two minor loops are specified within the major loop. Case 2(a): thicker minor loop than in Case 1(a). 1(b) and 2(b): nature of complete loops.

The model developed in this chapter, as explained and demonstrated above, has

several advantages over our earlier work in chapter 2. These advantages include a more intuitive underlying frictional system, analytical insights into basis functions, a minimal number of states (two), a small number of fitted parameters, and the ability to match a reasonable range of hysteretic behaviors.

The computational complexity of our model exceeds that of the Bouc-Wen model but compensates by capturing minor loops. A comparison of the energy dissipation per cycle for the Bouc-Wen model and for the two-state model is presented in Appendix F. Direct computation with the Iwan model for arbitrary forcing, in high dimensions, would be significantly more complex than for our model.

Further study may clarify the precise advantages of including more than two states in the hysteresis model; why (apparently) two distinct changes in slope are difficult for the model to capture; and how parameter fitting can be done more reliably and efficiently than using general purpose minimization routines with random initial guesses.

New research questions might also now be addressed somewhat more easily in future work; these include control strategies for such hysteretic systems, as well as the nonlinear dynamics of systems that include elements with such hysteretic behavior.

3.6 Closing note

An anonymous reviewer of [32] brought to our attention the work by Scerrato *et al.* [35, 36]. These works are interesting and complementary to our future intent, possibly opening up new lines of research for both.

In particular, in these works, a micro-structural model for dissipation in concrete is considered, while our starting model is abstract although physical, and not motivated by any specific material. Both models allow complex stress histories, but their work considers multiaxial stress states while ours so far does not. In that work, the experimental hysteresis loops fitted are asymmetric, while ours are symmetric. We have fewer state variables than they do.

Thus, their work motivates our approach to try to incorporate triaxiality in stress and asymmetry in hysteresis loops, while our work suggests new methods of approximation and model order reduction that may lead to improvements in their approach.

Chapter 4

Hysteresis in bolted joints described by the two state model

In this chapter, we apply the model of chapter 3 to a practical problem. In particular, we study lap joints connecting two plates, with a single bolt and with two bolts, loaded cyclically in the transverse direction. Computational solutions in ABAQUS show hysteresis in force-displacement responses. We first normalize the computationally obtained hysteresis loops to obtain new ones with standardized slopes and widths. We then apply our two state hysteresis model to capture these normalized hysteresis loops. An excellent match is obtained with the reduced order model, which has two free parameters. Interestingly, for single-bolted lap joints, the same hysteresis model works well over a range of friction coefficients and bolt preloads. For the double-bolted lap joint, there are two friction coefficients and two preloads; and the fitted parameters are not constant over different combinations thereof.

4.1 Introduction

Bolted joints can play a significant role in the overall damping behavior of structures. The mechanics of dissipation in bolted joints is complicated and highly nonlinear. Under cyclic loading, bolted lap joints dissipate energy *via* small-scale frictional sliding between contacting surfaces [38, 39]. A key feature of such hysteretic behavior

is that, if there is partial unloading and reloading within a larger loading path, the response shows slender *minor loops* within the bigger, or major, hysteresis loop. Simple hysteresis models struggle with such minor loops, and we will discuss this issue in some detail in due course.

Detailed study of dissipation in bolted joints involves identification and tracking of microslip motions. The available literature contains both constitutive and phenomenological models: see e.g., the review paper by Ibrahim and Petit [40] and the references therein. Recent trends in joint design involve detailed finite element computations, which require solving nonlinear contact mechanics problems at the joint interfaces. Due to modeling complexities and the high computational cost of full finite element solutions, a simpler model that captures several key aspects of the dissipation in joints is desirable. This need has been addressed in recent times by many authors, as discussed below; and the present chapter provides an efficient and unconventional approach to the same problem.

There have been many studies on dissipation in jointed structures over several decades. A representative sample of the literature follows. In 1964, Ungar [41] experimentally studied the effects of joint spacing, joint tightness, flange material, and surface finish on the damping of built up structures. In 1966, Earles [42] presented a theoretical estimation of the frictional energy dissipation in a lap joint. In 1968, Metherell and Diller [43] derived an equation for energy dissipation per cycle in a lap joint for steady-state cyclic loading under uniform clamping pressure. More recently, Beards [44] studied damping in mechanical systems with bolted joints due to wear and fretting. Beards also estimated that almost 90% of the total damping is provided by the joints. Gaul and Lenz [45] used a reduced parameter Valanis model [46] to capture hysteresis loops obtained from experiments. Chen and Deng [47] did finite element calculations to predict the effect of dry friction on the damping in frictional joints.

More directly related to our present work, several authors have used the Iwan model [10, 11] to study hysteretic damping in various jointed structures. The Iwan

model is a parallel arrangement of many one-dimensional elements (sometimes called Jenkins elements, and sometimes called generalized Maxwell elements), each consisting of a spring and dry frictional slider. Song *et al.* [48] used adjusted Iwan beam elements to study effects of a bolted joint on beam structures. Segalman [12] used a four parameter distributed Iwan model to capture hysteretic behavior observed from experiments on lap joints, and obtained expressions for hysteretic dissipation under harmonic loading (no minor loops). Oldfield *et al.* [49] studied hysteresis in a finite element model of a bolted joint using Jenkins elements (i.e., the Iwan model) as well as the Bouc-Wen model [7, 8]. Iwan type models were subsequently used to study various hysteretic behaviors in frictional joints in several papers [50]-[55]. Most recently, Brake [13] studied an Iwan model that includes pinning for bolted joints.

As the previous paragraph shows, the utility of the Iwan model in describing the behavior of joints is well established. The present chapter proposes a method of normalizing the hysteresis loops, followed by applying a drastically reduced order, two state approximation to a high-dimensional Iwan model, which can be used easily for such joints.

For readers not fully familiar with the issue of minor loops in hysteresis, a comparison between the Iwan and the Bouc-Wen models is useful for motivation. The Iwan model is high-dimensional and strongly nonlinear, and numerical solution is complicated when there are many Jenkins elements. The model's evolution is not expressible using a few simple differential equations. However, the response of the Iwan model is realistic, especially when there are minor loops within larger ones, i.e., small load reversals within larger load cycles. In contrast, the Bouc-Wen model involves a simple scalar ordinary differential equation with four free parameters, but it does not capture minor loops (for further discussion see, e.g., [16]). In other words, in complex deformation cycles where there are multiple load reversals within each cycle, the Bouc-Wen model is inappropriate and the Iwan approach is distinctly superior. This is why a reduced order approximation of the Iwan model, even if it

is more complex than the Bouc-Wen model, is desirable.

With the above motivation, we have developed in this thesis an unconventional model reduction method (chapters 2 and 3). We have obtained in chapter 3 a reduced order model with two states and six fitted parameters. In this chapter we simplify the model further, and apply it to the behavior of bolted joints with frictional interfaces. It will be seen that the results obtained are excellent.

In what follows, we perform detailed finite element (FE) simulations of lap joints connecting two plates, with either a single bolt or two bolts, using the finite element package ABAQUS, to compute hysteretic responses. We normalize the computed hysteresis loops to obtain new ones with standardized slopes and widths. Subsequently, we apply our two-state model with two free parameters to capture these normalized hysteresis loops. For single-bolted lap joints, we observe that the same fitted parameter values work well for a given range of friction coefficients and bolt preloads. For a double bolted lap joint, the fitted parameters change for different combinations of friction coefficients and bolt preloads. In both cases, the numerical match is excellent while the computational load is far smaller than for a comparably accurate Iwan model.

4.2 Computational data: finite element modeling of bolted joints

For simplicity we present the single-bolt computations first, followed by fitting procedures and results. The generality of the approach will be demonstrated later with a two-bolt calculation, presented in an appendix.

4.2.1 Single bolt model

We consider two plates connected by a single-bolted lap joint as sketched in Figure 4.1. The material properties assigned were $E = 210$ GPa and $\nu = 0.3$. Following [56, 57], the bolt and nut are modeled as one integral object for simplicity, i.e.,

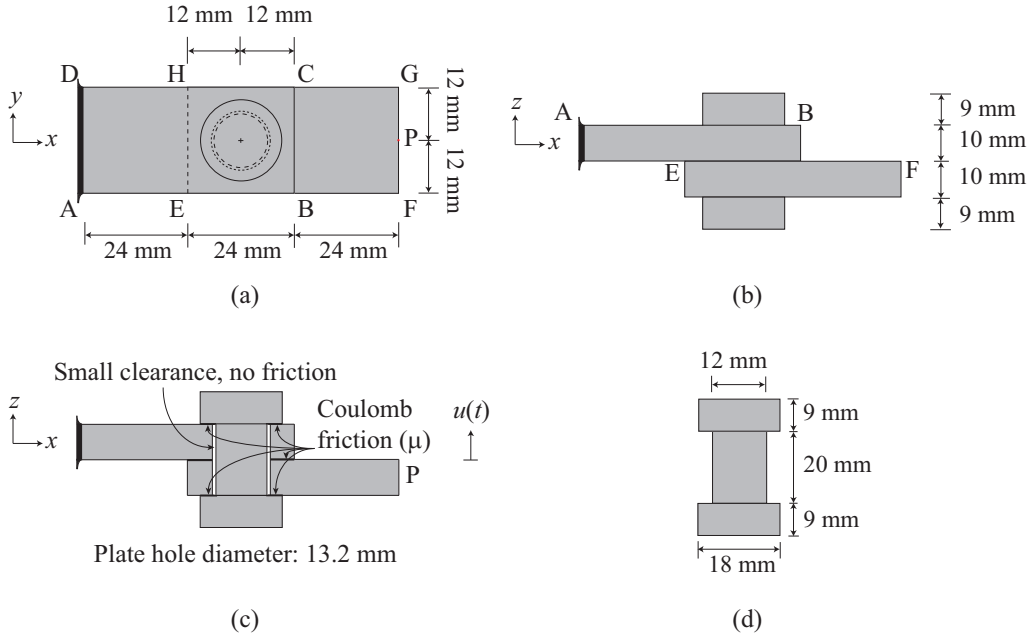

Figure 4.1: A single-bolted lap joint connecting two plates: (a) top view, (b) side view, (c) mid-sectional side view. The left end is clamped, and the right end is free. Point P is the mid point of the edge FG. We apply transverse displacement inputs $u(t)$ at P. (d) The bolt and nut are modeled as one integral object. The radial clearance between the bolt shank and plate holes is 0.6 mm.

threads are not modeled.

Figure 4.2 depicts the 3D finite element model defined in ABAQUS. Frictional contact with possible separation is defined between the two plates. ABAQUS offers an inbuilt facility for assigning bolt preloads.

We carried out pseudostatic analyses of the ABAQUS model under (a) six different two-frequency displacement inputs with the same friction coefficient and same bolt preload (Table 4.1); and (b) the same two-frequency displacement input with two different friction coefficients and two different bolt preloads (Table 4.2). For each case, the finite element simulation was run for three cycles of $u(t)$ with 3000 time steps, or 1000 steps per cycle.

4.2.2 Computational results: normalized hysteresis loops

Figure 4.3(a) shows a deformed configuration of the model at an intermediate instant in a finite element simulation of case 1 of Table 4.1. Displacements are exaggerated.

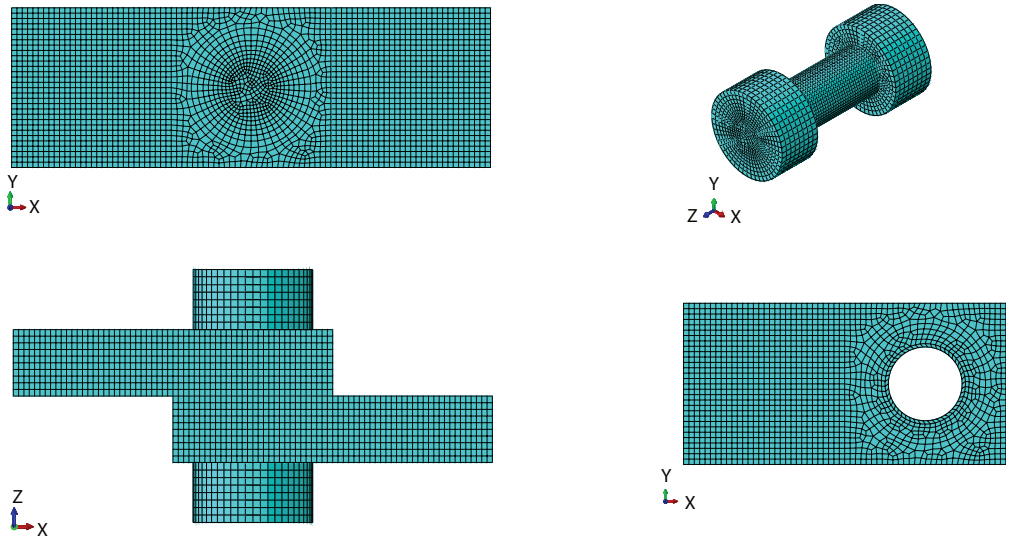

Figure 4.2: 3D finite element mesh in ABAQUS. C3D8R, a 8-node linear brick element, is used. The mesh is finer around the plate holes. Total elements: 50062, after convergence checks on the hysteresis loops.

Table 4.1: Six different two-frequency displacement inputs with same friction coefficient μ and same bolt preload (PL) considered for the finite element simulation.

Case	μ	PL (kN)	$u(t)$ (mm)
1	0.15	20	$2\sin 2\pi t + \sin 8\pi t$
2	0.15	20	$2\sin 2\pi t + \sin 9\pi t$
3	0.15	20	$2\sin 2\pi t + 0.8\ \sin 10\pi t$
4	0.15	20	$2\sin 2\pi t + 0.8\ \sin 11\pi t$
5	0.15	20	$2\sin 2\pi t + 0.6\ \sin 12\pi t$
6	0.15	20	$2\sin 2\pi t + 0.6\ \sin 13\pi t$

We emphasize that, although we refer to time, the simulation is quasistatic.

The finite element simulations give the time histories of reaction forces $f(t)$ at point P. To study the hysteretic response, we plot $f(t)$ against $u(t)$. The numerical results do show hysteresis. However, the actual hysteresis loops are too thin to show details clearly, see e.g., Figure 4.3(b). To see hysteretic responses in more detail, some kind of normalization or widening is needed (see e.g., [58]).

Examination of the hysteresis loops shows that they have some common qualitative features, shown schematically in Figure 4.4. These features are: a limiting slope s_0 for the loading and unloading curves; a near-constant initial slope s_1 at vertices;

Table 4.2: Same two-frequency displacement input, but different friction coefficients μ and bolt preloads (PL).

Case	μ	PL (kN)	$u(t)$ mm
1	0.10	20	$2\sin 2\pi t + \sin 8\pi t$
2	0.20	20	$2\sin 2\pi t + \sin 8\pi t$
3	0.15	30	$2\sin 2\pi t + \sin 8\pi t$
4	0.15	40	$2\sin 2\pi t + \sin 8\pi t$

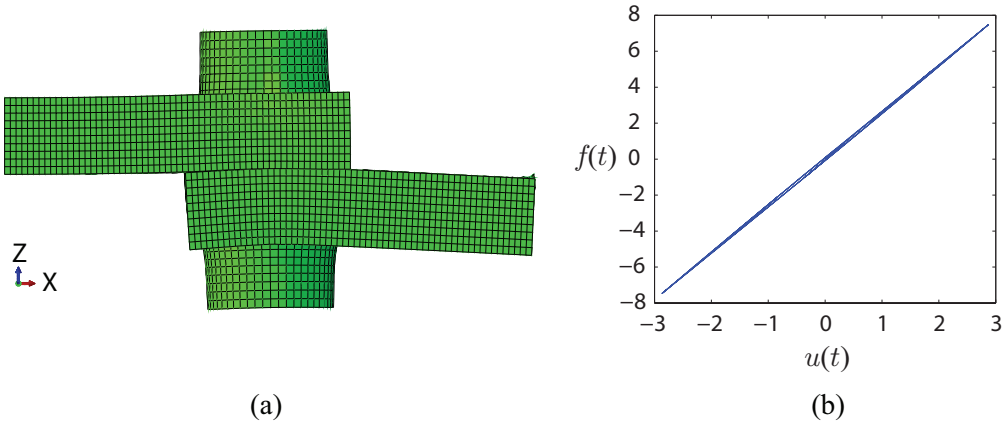

Figure 4.3: (a) A deformed configuration of the FE model at an instant for case 1 of Table 4.1. (b) Plot of $f(t)$ vs. $u(t)$ for case 1 of Table 4.1. Here, $f(t)$ is in kN and $u(t)$ is in mm. The result shows a narrow hysteresis loop. Such narrow loops will be widened by normalization below, and their fine details will be matched using the hysteresis model.

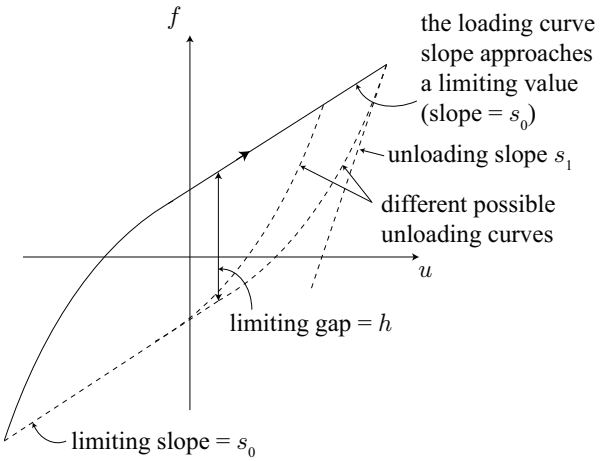

Figure 4.4: Qualitative features of the observed hysteretic response.

and a limiting separation or gap, h. In general, these quantities depend on the joint details (geometry as well as friction coefficient and preload).

For our present purpose, we use linear transformations on all FE results to transform the hysteresis loops into new ones for which

$$s_0 = 0,\ h = 2, \text{and}\ s_1 = 1. \tag{4.1}$$

To this end, we define

$$\bar{f} = a_0 f - a_1 u, \tag{4.2}$$

and

$$\bar{u} = a_2 u, \tag{4.3}$$

where a_0, a_1 and a_2 are scalar multipliers to be chosen appropriately to achieve Eq. (4.1). The determination of a_0, a_1 and a_2 for a given computationally obtained hysteresis loop is straightforward, involves solution of linear equations, and is not discussed further. Results are shown in Figures 4.5 and 4.6.

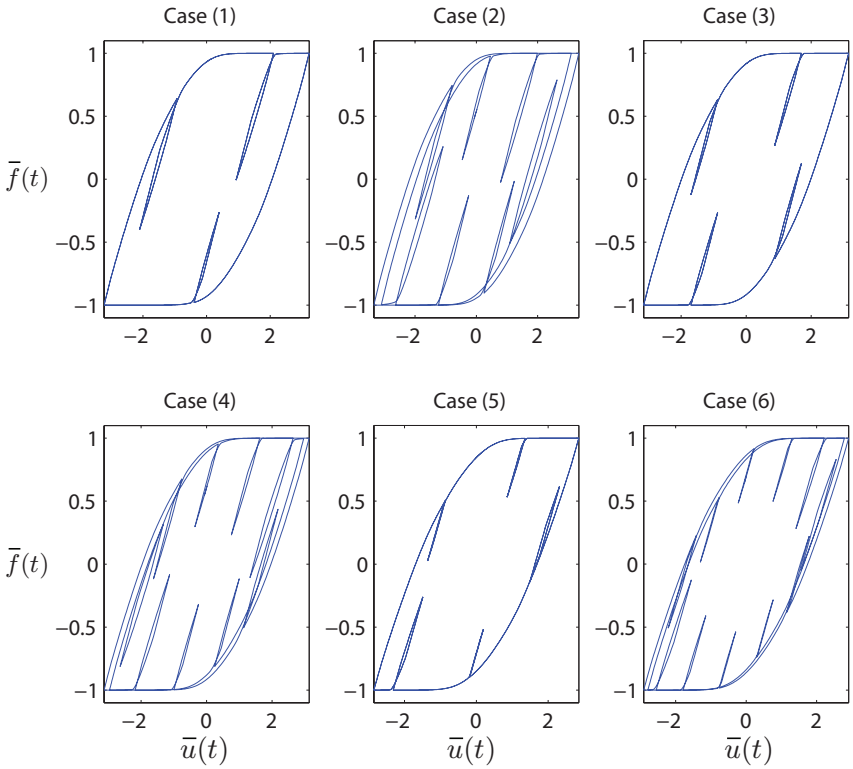

Figure 4.5: Hysteresis loops obtained for the cases considered in Table 4.1. $a_0 = 11.1266$, $a_1 = 28.6250$ and $a_2 = 1.1255$ for all six cases. Note that the saturated loading curve slope $s_0 = 0$, limiting gap $h = 2$, and the initial unloading curve slope $s_1 = 1$ in all cases, matching Eq. (4.1). Minor loops are clearly seen.

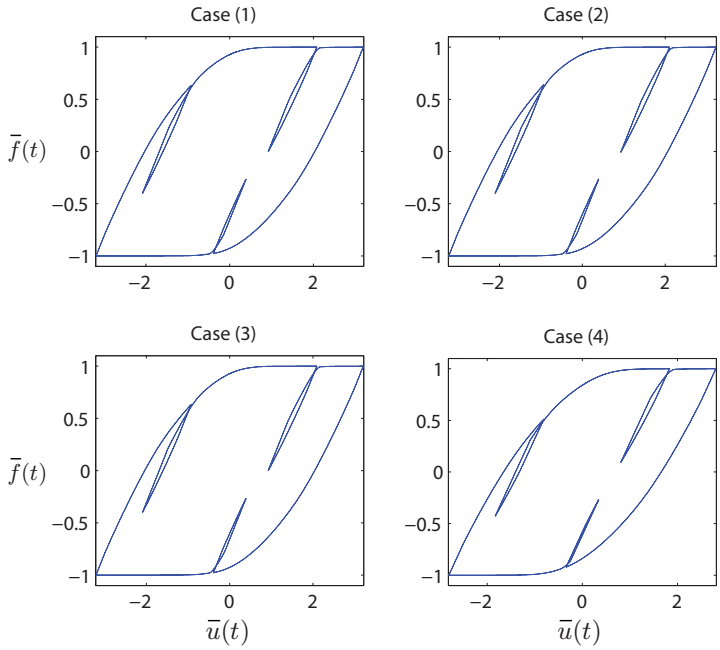

Figure 4.6: Hysteresis loops obtained for the cases considered in Table 4.2. Case 1: $a_0 = 15.1656$, $a_1 = 39.0379$ and $a_2 = 1.1134$. Case 2: $a_0 = 8.8871$, $a_1 = 22.8566$ and $a_2 = 1.1259$. Case 3: $a_0 = 7.6868$, $a_1 = 20.2205$ and $a_2 = 1.1195$. Case 4: $a_0 = 6.9522$, $a_1 = 18.0100$ and $a_2 = 0.9801$. Note that the conditions of Eq. (4.1) are achieved in all cases.

Figures 4.5 and 4.6 show such transformed (normalized) $\bar{f}$ vs. $\bar{u}$ for the loading cases given in Tables 4.1 and 4.2 respectively. It is clear that the conditions of Eq. (4.1) have been achieved in all cases. We emphasize that each of the transformed loops in these two figures originally looked like the loop in Figure 4.3(b), but contained much detail including minor loops that are now easily visible.

In Figure 4.5, the numerical values of a_0, a_1 and a_2 are the same for all cases, since the friction coefficient and bolt preload are the same. In Figure 4.6, the numerical values of a_0, a_1 and a_2 are different for different cases, since the friction coefficient and bolt preload vary.

Figures 4.5 and 4.6 provide illustrative data, intended to motivate application of the two-state model. For completeness and for further evaluation of the model, we will present additional numerical results for single-bolted lap joints in Appendix H, considering different bolt head thickness, clearance between the bolt shank and plate holes, friction coefficients, and bolt preloads. As mentioned above, we will also

consider two-bolt joints in due course, to demonstrate the general applicability of our proposed approach.

We now move on to the two-state hysteresis model.

4.3 Two-state hysteresis model

The reduction of an Iwan model with many sliding elements to a two-state model is described in chapter 3. The final computation there is summarized in this section for completeness.

The model has three system matrices $\bar{K}$, A, and $\bar{b}$

$$\bar{K} = \bar{\alpha} \begin{bmatrix} 1 & 0 \\ 0 & 1 \end{bmatrix}, \quad A = \bar{\mu} \begin{bmatrix} \sigma & 0 \\ 0 & 1 \end{bmatrix}, \quad \text{and} \quad b = \begin{Bmatrix} \bar{b}_1 \\ \bar{b}_2 \end{Bmatrix}, \tag{4.4}$$

where $\bar{\alpha} > 0$, $\bar{\mu} > 0$, and $0 < \sigma < 1$.

The state vector q is 2×1, and the input u is a scalar, with $\dot{u}$ assumed known. Given q and u, we compute

$$c = \bar{K}q - \bar{b}u = \bar{\alpha}q - \bar{b}u. \tag{4.5}$$

We define

$$y = \sqrt{\eta^T A \eta} + \eta^T c. \tag{4.6}$$

We minimize y with respect to η subject to $\eta^T \eta = 1$. This leads to

$$\frac{A\eta}{\sqrt{\eta^T A \eta}} + c - \lambda\eta = 0, \tag{4.7}$$

where λ is a Lagrange multiplier. Let the minimizing η be η^*. If $y(\eta^*) \leq 0$, slip can

occur. η^* can be found by solving a 4×4 eigenvalue problem, namely of matrix

$$B = \begin{bmatrix} A & cc^T \\ A & A \end{bmatrix}.$$

B has 4 eigenvalues (of at least 2 are real), and either 2 or 4 real eigenvectors. We have shown in Appendix C that η^* is the upper half (2×1) of a real eigenvector of B, normalized to $\eta^{*T}\eta^* = 1$, and with sign chosen such that $\eta^{*T}c \leq 0$. In computation, we check all real eigenvectors (2 or 4) and select the one that minimizes y of Eq. (4.6).

A recipe for the model's computation now follows.

1 Given the system parameters $\bar{\alpha}$, $\bar{\mu}$, σ, $\bar{b}_1$, and $\bar{b}_2$ along with the input $u(t)$ and current state q, our aim is to find $\dot{q}$. To this end we first find η^* and $y^* = \sqrt{\eta^{*T} A \eta^*} + \eta^{*T} c$ as described above.

2 Then, we compute

$$\dot{s} = \left[\frac{\eta^{*T}\bar{b}}{\bar{\alpha}} \dot{u} - y^* |\dot{u}| \right] \cdot \{y^* \leq 0\}, \tag{4.8}$$

where $\{y^* \leq 0\}$ is a logical variable (1 if the condition holds, and 0 otherwise).

3 Finally, the state evolves as

$$\dot{q} = \eta^* \dot{s} \cdot \{\dot{s} > 0\}, \tag{4.9}$$

where $\{\dot{s} > 0\}$ is a logical variable as above, and Eq. (4.9) is to be integrated numerically to find $q(t)$.

4 The hysteretic output force $f(t)$ is

$$f(t) = u(t) - q^T \bar{b}. \tag{4.10}$$

4.4 Elimination of superfluous parameters

The model of section 4.3 can be simplified further. In [32], we failed to notice that if $\bar{K}$, A and $\bar{b}$ are replaced with $r^2\bar{K}$, r^2A and $r\bar{b}$, respectively, then the hysteretic output does not change. Accordingly, we can take $\bar{\mu} = 1$ in Eq. (4.4). We thus have

$$\bar{K} = \bar{\alpha} \begin{bmatrix} 1 & 0 \\ 0 & 1 \end{bmatrix}, \quad A = \begin{bmatrix} \sigma & 0 \\ 0 & 1 \end{bmatrix}, \quad \text{and} \quad \bar{b} = \begin{Bmatrix} \bar{b}_1 \\ \bar{b}_2 \end{Bmatrix}$$

with *four* free parameters $\bar{\alpha}$, σ, $\bar{b}_1$, and $\bar{b}_2$.

Our aim is now to understand the role of the above four parameters, and to seek further reduction in number of free parameters. To that end, we assume the input displacement u is large enough to cause saturation in the hysteresis loops' loading curves as seen above (Figures 4.5 and 4.6).

From numerics, we have observed that as $|u|$ becomes large, c (Eq. (4.5)) saturates to one of two limiting vectors $\pm c_s$, i.e.,

$$\pm c_s = \bar{\alpha} q - \bar{b} u \quad \text{for } u \text{ large.} \tag{4.11}$$

It can be shown that (see Appendix I)

$$c_s = -\frac{A\bar{b}}{\sqrt{\bar{b}^T A \bar{b}}}. \tag{4.12}$$

From Eqs. (4.11) and (4.12), when $c = c_s$,

$$q = \frac{u}{\bar{\alpha}}\bar{b} - \frac{A\bar{b}}{\bar{\alpha}\sqrt{\bar{b}^T A \bar{b}}}. \tag{4.13}$$

Substituting Eq. (4.13) in Eq. (4.10), when $c = c_s$,

$$f = \left(1 - \frac{\bar{b}^T \bar{b}}{\bar{\alpha}}\right) u + \frac{\sqrt{\bar{b}^T A \bar{b}}}{\bar{\alpha}}. \tag{4.14}$$

In fact, when $c = \pm c_s$

$$f = \left(1 - \frac{\bar{b}^T \bar{b}}{\bar{\alpha}}\right) u \pm \frac{\sqrt{\bar{b}^T A \bar{b}}}{\bar{\alpha}}. \tag{4.15}$$

Recalling Figure 4.4, Eq. (4.1), and Figures 4.5 and 4.6, we see that $s_0 = 0$ can be achieved if

$$1 - \frac{\bar{b}^T \bar{b}}{\bar{\alpha}} = 0 \tag{4.16}$$

and $h = 2$ can be achieved if

$$\frac{\sqrt{\bar{b}^T A \bar{b}}}{\bar{\alpha}} = 1. \tag{4.17}$$

From Eq. (4.1), the condition $s_1 = 1$ remains to be fulfilled. To this end, recall Eq. (4.10) and note that upon reversal of loading direction there is always a brief phase of sticking (such that $\dot{q} = 0$). With our hysteresis model, therefore, $s_1 = 1$ in all cases. All conditions of Eq. (4.1) are satisfied if (from Eqs. (4.16) and (4.17))

$$\bar{b}_1 = \pm\sqrt{\frac{\bar{\alpha}(1-\bar{\alpha})}{1-\sigma}} \quad \text{and} \quad \bar{b}_2 = \pm\sqrt{\frac{\bar{\alpha}(\bar{\alpha}-\sigma)}{1-\sigma}}.$$

In fact, simple checks show that the choice of sign has no real consequence, and we therefore take

$$\bar{b}_1 = \sqrt{\frac{\bar{\alpha}(1-\bar{\alpha})}{1-\sigma}} \tag{4.18}$$

and

$$\bar{b}_2 = \sqrt{\frac{\bar{\alpha}(\bar{\alpha}-\sigma)}{1-\sigma}}. \tag{4.19}$$

In this way, subject to the hysteresis loops satisfying $s_0 = 0$, $h = 2$ and $s_1 = 1$ (Eq. (4.1)), $\bar{b}_1$ and $\bar{b}_2$ are not free parameters any more. Only two free parameters, namely $\bar{\alpha}$ and σ, remain for fitting the hysteresis loops.

Figure 4.7 shows two possible loops with $s_0 = 0$, $h = 2$ and $s_1 = 1$, for different choices of $\bar{\alpha}$ and σ. For Figure 4.7(a), $\bar{\alpha} = 0.5$, $\sigma = 0.49$ and $u(t) = 5 \sin t$. For Figure 4.7(b), $\bar{\alpha} = 0.5$, $\sigma = 0.49$ and $u(t) = 3 \sin t + 1.5 \sin 5t$. In each case, $\bar{b}_1$ and $\bar{b}_2$ are calculated using Eqs. (4.18) and (4.19) for chosen sets of $\bar{\alpha}$ and σ. It is seen that adjusting $\bar{\alpha}$ and σ can have a significant effect on the shapes of loops obtained.

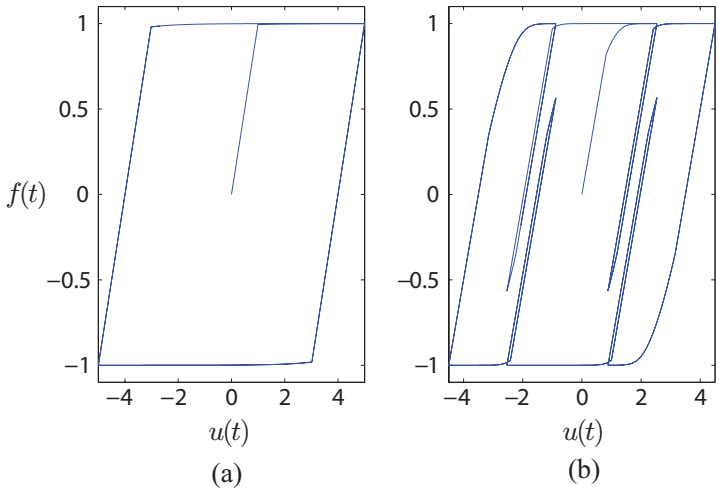

Figure 4.7: Hysteretic responses of the two-state model with $s_0 = 0$, $h = 2$ and $s_1 = 1$.

So far, we have normalized the loops to be fitted; and also reduced the number of free parameters in the hysteresis model from five to two. We now proceed to fit the FE results with our two-state hysteresis model.

4.5 Parameter fitting to match FE simulation data

We now use the two state hysteresis model with the above simplifications to fit the normalized loops obtained from finite element simulations.

In each case, we use Eqs. (4.2) and (4.3) to transform the hysteresis loops into new ones satisfying $s_0 = 0$, $h = 2$ and $s_1 = 1$. Subsequently, using our two-state model with two free parameters $0 < \sigma < \bar{\alpha} < 1$ (see Eqs. (4.18) and (4.19)), we use a least squares criterion to fit the data (see Figure 4.8). For simplicity, we use the elementary Matlab function `fminsearch` for minimizing our least squares error measure. Results of fitting are given below.

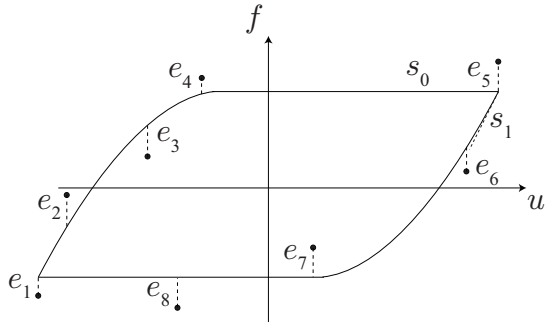

Figure 4.8: Fitting a hysteresis loop. Dotted points represent given discretely spaced data. Vertical distances between the data and the fitted loop are squared and added. The sum is minimized with respect to the fitted parameters.

4.6 Results and discussion

From numerical fitting of all load cases considered so far (Tables 4.1 and 4.2), the following parameter values were found to give good results:

$$\bar{\alpha} = \frac{2}{3},\ \sigma = \frac{1}{16}, \tag{4.20}$$

with $\bar{b}_1$ and $\bar{b}_2$ obtained using Eqs. (4.18) and (4.19), respectively. Note that these same parameters are used for the single-bolt joint, for a few different friction coefficients as well as bolt preloads. The differences arising due to changing friction coefficients and bolt preloads are, it therefore appears, taken care of during normalization of the hysteresis loop.

The fit quality is shown in Figures 4.9 and 4.10, corresponding to Figures 4.5 and 4.6 respectively. The hysteresis loops are plotted using simple solid lines, and the FE results are plotted using lines with dots.

The fit is excellent considering the simplicity of the model and the small number of free parameters (only two). Note that the actual loops are very small, and it is the normalized view that allows us to display the relatively small mismatch near the bending portions of the loops (bottom right and top left). Finally, using more states in the model (easy to develop following chapter 3), an even better fit is possible (details not presented). In Appendix G, we present a comparison between the fit

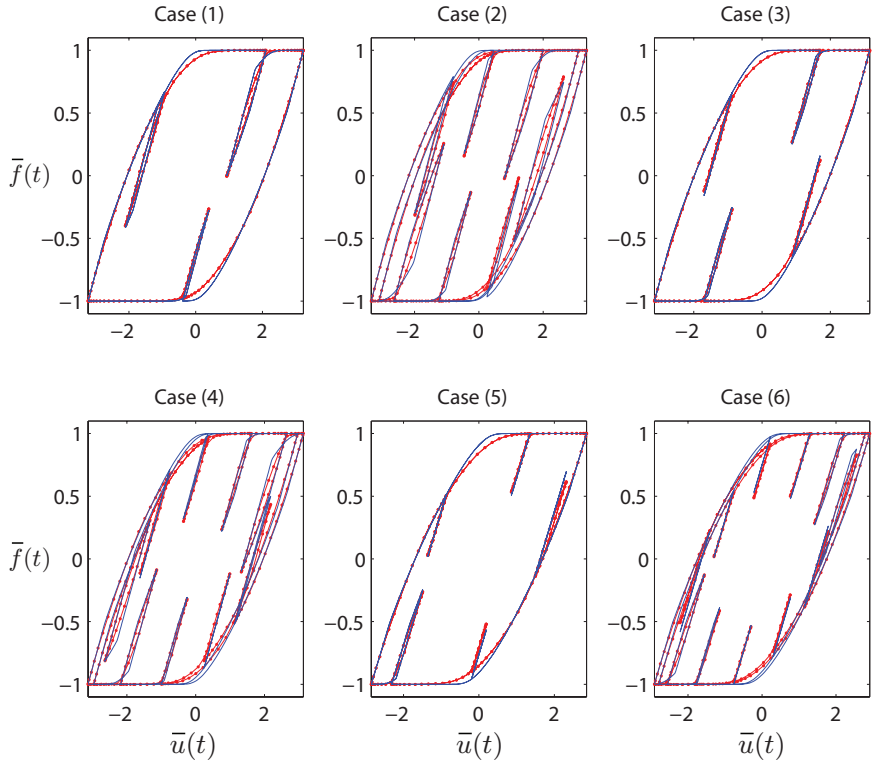

Figure 4.9: Fitting loops of Figure 4.5, with parameters given in Eq. (4.20). The blue solid lines: fitted hysteresis loops from the two-state model. Red solid lines with dots: FE results.

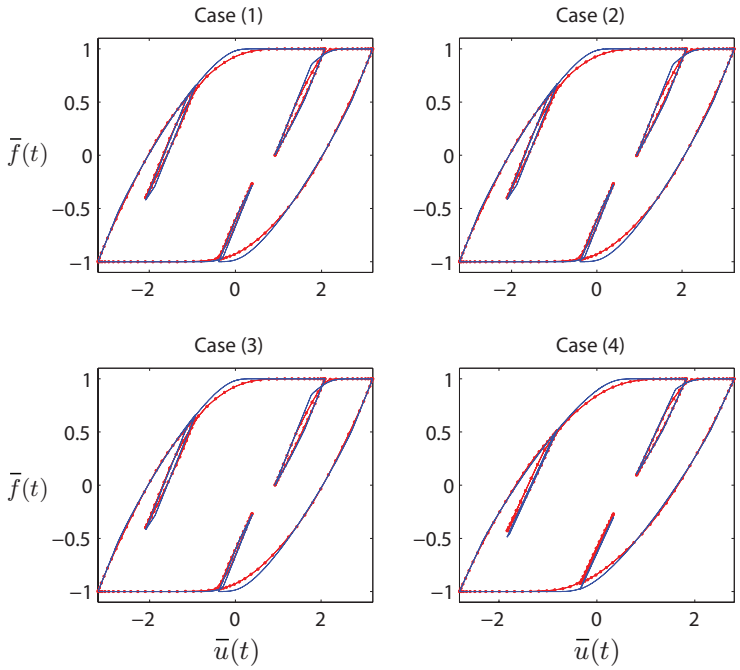

Figure 4.10: Fitting loops of Figure 4.6, with parameters given in Eq. (4.20). The blue solid lines: fitted hysteresis loops from the two-state model. Red solid lines with dots: FE results.

quality of the two-state model and the Iwan model.

Appendix H presents further fitting results for other single-bolt joint designs (different bolt heads and clearances; different friction coefficients and preloads). The match there is as good as it is here.

We close this section with some key observations and pointers to other calculations in the appendices. In our present approach, we have normalized the computed hysteretic responses from FE simulations, using three scalars a_0, a_1 and a_2 (Eqs. (4.2) and (4.3)), to obtain new ones with standardized slopes and widths (Eq. (4.1)). Such normalization makes both the fitting process and fit quality more transparent. These three parameters in the transformation, namely a_0, a_1 and a_2, vary with the joint's geometry (e.g., single-bolted or double-bolted), friction coefficients, and bolt preloads. For the special case of *single-bolted* lap joints, we have observed empirically that the same set of numerical parameters σ and $\bar{\alpha}$ (Eq. (4.20)) works well over a range of friction coefficients and bolt preloads. However, for two-bolt joints with differing friction coefficients and bolt preloads, we have found that the same numerical σ and $\bar{\alpha}$ do *not* fit all the data. Simulations and fitting examples for a two-bolt joint are given, for completeness, in Appendix J.

4.7 Concluding remarks

In this chapter, we have demonstrated that hysteresis loops in the load-deflection behavior of frictional bolted joints have some common features that allow normalization of these loops. Upon such normalization, a simplified version of a recently developed two-state hysteresis model can conveniently capture these same loops with fairly high accuracy. There have been several papers in the literature that model the behaviors of such joints using Iwan models, which are computationally more cumbersome. In terms of fit quality achievable for a given level of computational complexity, we believe that our proposed approach is the best one presently available in the literature. We hope that the present model will be deemed useful for modeling such bolted joints.

Chapter 5

A new explicit approximation for the slip direction η

In this chapter, we give an explicit approximation for slip direction η. The approximation turns out to be reasonably accurate, and it eliminates the 4×4 eigenvalue problem as used in chapter 3. Specifically, we find a patched asymptotic approximation for η, considering small c, infinite c, and a special choice of intermediate c ($c = c_s$; see chapter 4, Eq. (4.11)).

5.1 Patched asymptotic approximation for η

We proceed as follows.

Recall from chapter 3 that to find slip direction η, we minimize

$$y = \sqrt{\eta^T A \eta} + \eta^T c$$

with respect to η subject to $\eta^T \eta = 1$. This leads to

$$\frac{A\eta}{\sqrt{\eta^T A \eta}} + c - \lambda \eta = 0. \tag{5.1}$$

Now, we consider small c, infinite c, and $c = c_s$ in Eq. (5.1) to find a patched

asymptotic approximation for η.

1 As $\|c\| \to 0$.

From Eq. (5.1), as $\|c\| \to 0$, we have in the limit

$$\frac{1}{\sqrt{\eta^T A \eta}} A\eta - \lambda\eta = 0.$$

Thus, as $\|c\| \to 0$, $\eta \to -\text{sgn}(c^T x_1)x_1$. Here, x_1 is the eigenvector of A corresponding to the minimum eigenvalue (recall that A is diagonal, and $x_1 = [1\ \ 0]^T$).

2 As $\|c\| \to \infty$.

From Eq. (5.1), as $\|c\| \to \infty$, $\eta \to -c/\|c\|$.

3 As $c \to c_s$.

As discussed in chapter 4, we have observed that as $|u|$ becomes sufficiently large, c saturates to one of two constant vectors $\pm c_s$, where (Appendix I)

$$c_s = -\frac{A\bar{b}}{\sqrt{\bar{b}^T A \bar{b}}}.$$

It is also shown in Appendix I that as $c \to c_s$, $\eta \to \hat{b} = \bar{b}/\|\bar{b}\|$.

Based on the above, we propose tentatively a patched asymptotic approximation for η that matches asymptotic limits of $c \to 0$, and $c \to \infty$, namely

$$\eta \approx \frac{-\text{sgn}(c^T x_1)x_1 + Qc - \|c\|c}{1 + \beta_0\|c\| + \|c\|^2}, \tag{5.2}$$

where Q is a diagonal matrix to be fitted; and β_0 is a free parameter (we have arbitrarily used $\beta_0 = 10$ and obtained good results). Putting $\eta = \hat{b}$ and $c = c_s$ in Eq. (5.2), we get the elements of Q

$$Q_j = \frac{\text{sgn}(c_s^T x_1)x_{1j} + (1 + \beta_0\|c_s\| + \|c_s\|^2)\hat{b}_j + \|c_s\|c_{sj}}{c_{sj}}, \quad j = 1, 2. \tag{5.3}$$

To summarize:

$$x_1 = \left\{ \begin{array}{c} 1 \\ 0 \end{array} \right\}, \quad \eta_0 = -\mathrm{sgn}(c^T x_1) x_1, \quad \eta_\infty = -\frac{c}{\|c\|},$$

$$c_s = -\frac{A\bar{b}}{\sqrt{\bar{b}^T A \bar{b}}}, \quad \beta_0 = 10, \quad Q = \left[\begin{array}{cc} Q_1 & 0 \\ 0 & Q_2 \end{array} \right],$$

with Q_1 and Q_2 given by Eq. (5.3). Finally for any c

$$\eta \approx \frac{-\mathrm{sgn}(c^T x_1) x_1 + Qc - \|c\| c}{1 + \beta_0 \|c\| + \|c\|^2}. \tag{5.4}$$

The above approximation need not have unit norm. Recall that $\eta^T \eta$ should be unity as per our initial problem statement, and $\eta^T \eta$ is indeed unity for $\|c\| \to 0$, $\|c\| \to \infty$ and $c = c_s$. In general, in numerical code, we normalize η to unit norm, for arbitrary c.

5.2 Results and comments

Note that the new explicit approximation for η (Eq. (5.4)) is actually a function of A, c and $\bar{b}$. In contrast, in our original formulation (chapter 3), η is a function of A and c, and $\bar{b}$ does not appear explicitly. This $\bar{b}$-dependence of the approximation is perhaps due to our trying to match it at points commonly encountered during the hysteresis calculation rather than at all possible possible points.

The new explicit approximation for η is actually good. In Figure 5.1, we present four numerical examples showing comparison between the simulations using exact η, and using the new approximation for η. The parameters and input $u(t)$ used for these four cases are given in Table 5.1. Note that the new approximation gives an excellent match with the exact one every time.

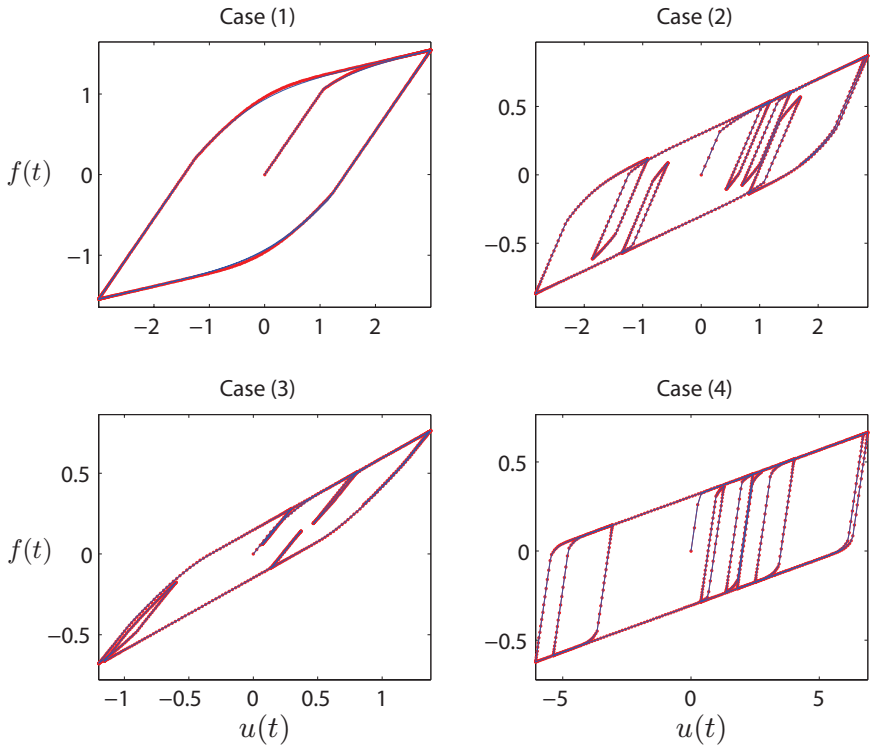

Figure 5.1: Comparison between the numerical results obtained using exact η (hysteresis loops with red solid lines with dots), and using the new approximation for η (hysteresis loops with blue solid lines).

Table 5.1: Parameters used in Figure 5.1.

Case	$\bar{\alpha}$	σ	$\bar{b}_1$	$\bar{b}_2$	$u(t)$
1	0.6134	0.2254	0.3353	0.6353	$3 \sin t$
2	5.0000	0.2800	1.5457	1.2692	$2 \sin t + 0.85 \sin 5.1524t$
3	17.6663	0.0906	1.7959	2.5594	$\sin t + 0.4 \sin 4.3675t$
4	7.8443	0.5570	1.9537	1.9020	$5 \sin t + 1.9 \sin 4.2314t$

5.3 Concluding remarks

In this chapter, we have found an analytical approximation, which is in closed form without requiring eigenvalue solution, using a patched asymptotic expansion. Readers may simply find this approximation interesting from an academic viewpoint. Alternatively, readers who in the process of numerical solution do not have access to eigenvalue routines may also like to use this approximation.

Chapter 6

Hysteretic damping in an elastic body with frictional microcracks

In this chapter, we study a rather different hysteresis model. In particular, we study an elastic plate with several randomly distributed and oriented frictional microcracks, loaded cyclically in plane stress. Computational solutions in ABAQUS show narrow hysteresis loops that are pinched at the origin and partially resemble an *ad hoc* model proposed by Reid [15]. We propose a new simple scalar model that gives a good qualitative match with the numerically obtained hysteresis loops. The material of this chapter has been published in [58].

6.1 Introduction

The aim of this chapter is to present a detailed computational study that *justifies* a nonintuitive hysteresis loop shape that has been proposed by some authors. Such theoretical justification would be particularly relevant to the vibration damping research community. Typical loops measured for metallic objects have distinctly different shapes than the loops to be studied in this chapter, which are relevant to materials with dry frictional cracks in them. A useful contribution of the present chapter is a simple scalar evolution equation that leads to hysteresis loops that qualitatively, though not completely, match the loops obtained from the computational

study. While our work impinges on studies in fundamental constitutive modeling of dissipative materials at microscales, our aim here is to contribute new ways to think about simple damping models for structural vibrations wherein such phenomena (e.g., internal frictional damping) can be approximately incorporated.

As mentioned earlier in the thesis, the available literature contains both papers that deal with the net material dissipation per cycle, as well as papers that consider details of the shapes of hysteresis loops. We focus on hysteresis that is rate or frequency-independent. Hysteretic material damping in many materials is experimentally well known to be frequency independent up to a few hundreds of Hz (for classical papers see e.g., Lord Kelvin [5], Rowett [3], Kimball & Lovell [6]). Mathematically, the dissipation D in the material, on a per cycle and per unit volume basis, has been approximated by an empirical power law,

$$D = J\sigma^n, \tag{6.1}$$

where σ is an equivalent stress amplitude, and J and $n \geq 2$ are material constants. Rowett [3] found $n \approx 3$ for torsion of steel tubes, while Kimball and Lovell [57] found $n \approx 2$ for eighteen different materials.

To motivate the present study of hysteresis loop shapes, Figure 6.1(a) shows a hysteresis loop measured by Rowett [3]. For comparison, Figure 6.1(b) shows a response computed using the empirical Bouc-Wen model [7, 8] under a single-frequency input[1]. Additionally, Figure 6.1(c) shows a hysteresis loop obtained from our own earlier model studied in chapter 2, derived formally from a high-dimensional frictional system, wherein $f(t)$ is a forcing input and $x(t)$ is a corresponding displacement output. The key difference between the Bouc-Wen model and our earlier model is that the latter captures *minor loops* upon partial unloading, while the Bouc-Wen model does not: see Figures 6.1(d) and (e). These two subfigures indicate clearly that the Bouc-Wen model may introduce errors when used to model

[1]The Bouc-Wen model consists of a scalar differential equation with output $z(t)$ (Eq. (2.1)). The model has four free parameters α_1, α_2, α_3 and n, for which we used the numerical values 1.2, 0.6, 0.45 and 1, respectively.

structural damping under multifrequency excitation or with interacting modes of vibration.

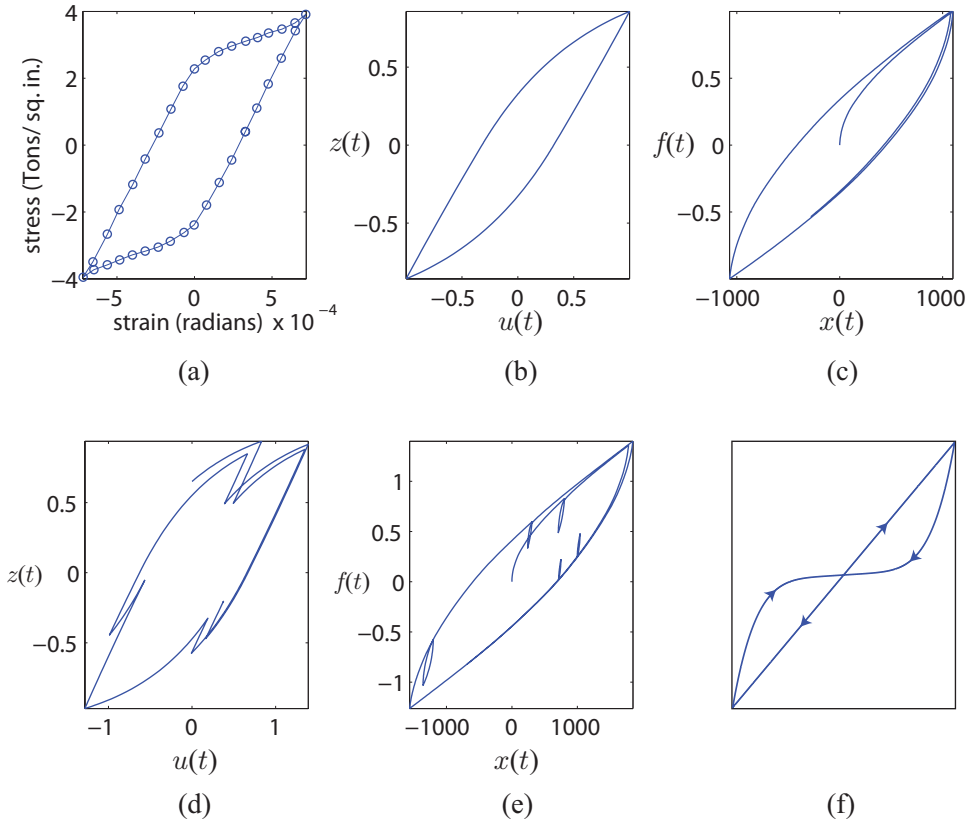

Figure 6.1: (a) Stress-strain hysteresis loop adopted from Rowett [3]; the vertical separation between loading and unloading is magnified 40-fold. (b) Bouc-Wen model under a single frequency input. (c) The model of chapter 2 under single-frequency input. (d) Bouc-Wen model under a two-frequency input. Minor loops are not captured and the response shows horizontal drift. (e) Minor loops are captured by the model of chapter 2. (f) Sketch of a hysteresis loop pinched at the origin (of primary interest in this study).

With the above motivation, in this chapter we first study hysteresis in a square elastic plate with several frictional microcracks of random sizes, locations and orientations. We perform finite element simulations of the plate under several time varying biaxial loadings. Interestingly, our results show hysteresis loops *quite unlike* those in Figures 6.1(a)-(e), and more like the loop in Figure 6.1(f).

The new loops resemble the pinched and angular loops proposed empirically by Reid [15] and Muravskii [59] (more on that below), but have additional features.

We will close the chapter with a new single degree of freedom evolution equation

which captures such pinched hysteresis loops, thus rationalizing the models of Reid and Muravskii through our finite element results, extending their approach, and giving a simple new model for such rate-independent hysteresis in low-dimensional systems.

For completeness, we mention here that damping due to microscopic frictional flaws has been studied elsewhere for more technologically driven applications, e.g., in coatings on turbine blades [60]-[62]. From more fundamental theoretical viewpoints, Barber and his co-authors have recently presented several studies in the mechanics of solids with frictional contacts [63]-[66]. In one of these studies [63], the authors discussed frictional dissipation in microcracks using Kachanov's [67] simplification for modeling interactions between the cracks. We also mention the Iwan model [10] here, used to model microslip in solid bodies using a set of one-dimensional elements in parallel, each consisting of a spring and frictional slider (referred to as Jenkins elements). The Iwan model has been used for interfaces and joints [50, 55], and also motivates our own two-state hysteresis model of chapter 3 that captures a variety of hysteretic behaviors including minor loops. However, the peculiar shape of the hysteresis loops observed in this study has not been noted before in the structural vibration research literature.

An underlying model of microcracks has been used for other technological applications as well. For example, toward understanding size effects in fatigue life of cracked bodies, Carpinteri and Spagnoli [68] developed a fractal set approach and proposed a size dependent stress intensity factor. Here, our study of a body with frictional microcracks is intended to yield insights into physical justifications for simple low-dimensional hysteresis models that can then be used for improved modeling of structural dissipation under multifrequency excitation. In our own earlier work [18] studying dissipation in a single frictional microcrack, we concentrated on per cycle effects as in Eq. (6.1). Here we study many cracks and within-cycle effects, as in Figure 6.1(e). The basic connection with Eq. (6.1) will be reestablished at the end of the chapter.

6.2 Computational model: an elastic plate with frictional microcracks

We consider a square elastic plate as in Figure 6.2. The plate has 32 randomly dispersed frictional microcracks. The crack positions, lengths, orientations, and friction coefficients (μ's) are assigned randomly within some ranges as described later. The cracks are non-propagating, and not too close to the edges of the plate. As shown in Figure 6.2, the plate is subjected to a bi-axial external load without

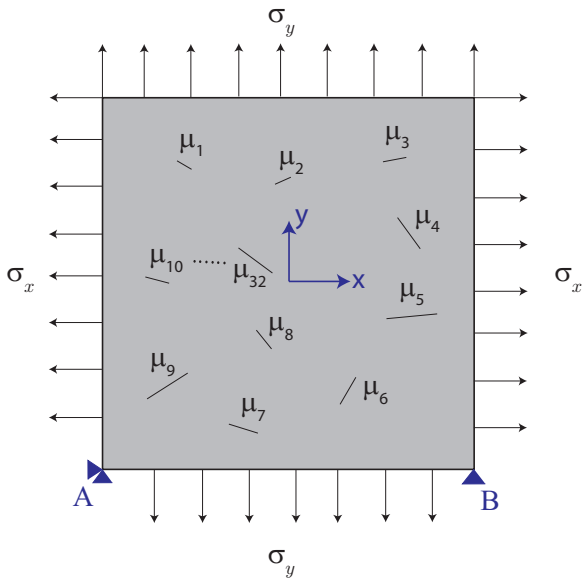

Figure 6.2: Square elastic plate with multiple frictional microcracks, under far-field bi-axial loading.

shear components. There is no loss of generality in the absence of far-field shear stress, because the crack orientation angles are randomly and uniformly distributed in $[0, \pi]$, and so statistically there are no special orientations of the edges of the square domain. In other words, we have merely assumed that our coordinate axes are aligned with the principal directions of the notional or macroscopic stress.

The crack faces do experience shear tractions, due to friction. Displacement boundary conditions are used at corners A and B to eliminate rigid body modes, as suggested in the figure.

6.2.1 Finite element simulations

Two finite element models of size 10 mm × 10 mm were made in ABAQUS with two different randomly generated sets of cracks. The crack lengths were taken to be uniformly distributed between 0.1 and 1 mm; the crack orientations uniformly distributed between 0° and 180°; the coordinates (x and y) of the crack centers uniformly distributed between -4 and 4 mm (leaving a 1 mm distance from all four edges); and the friction coefficients uniformly distributed between 0 and 1 (fixed μ were considered later as well). The Young's modulus and Poisson's ratio of the plate were taken arbitrarily as 210 GPa and 0.3 respectively.

Figures 6.3(a) and (b) show the two models generated using ABAQUS. We used element CPS4R, a 4 node bilinear element, for plane stress analysis (with thickness set to 1 mm) in these two models. Frictional contact with possible separation was defined on each crack face. Figure 6.3(c) shows a mesh for model 1. To accurately compute near-crack-tip stresses, a fine mesh is used near the tips (Figure 6.3(d)). Models 1 and 2 had 154710 and 130925 elements respectively. These numbers were chosen after convergence checks and are large enough for our purposes[2].

We carried out pseudostatic analyses in ABAQUS for these two models under 12 different load cases as given in Table 6.1. In the table, $f(t)$ represents a time-varying multiplier for the σ_x and σ_y values given. For example, for case 1, $\sigma_x = -20$, $\sigma_y = 100$ and $f(t) = \sin 2\pi t$ implies that the time-varying tractions on the boundary were based on the stress matrix

$$\sigma = \begin{bmatrix} -20 \sin 2\pi t & 0 \\ 0 & 100 \sin 2\pi t \end{bmatrix} \text{(MPa)}.$$

For each such load case, the finite element simulation was run for three cycles of $f(t)$. Each simulation was conducted with 600 load steps, which was found large

[2] Specifically, our convergence checks were made to ensure that further mesh refinement did not change the hysteresis loops within plotting accuracy; displacements at key nodes, stresses, strains, and dissipation all converged correspondingly. As emphasized earlier, our goal is to qualitatively identify the shapes of hysteresis loops and capture the same using a simple model for use in structural dynamics.

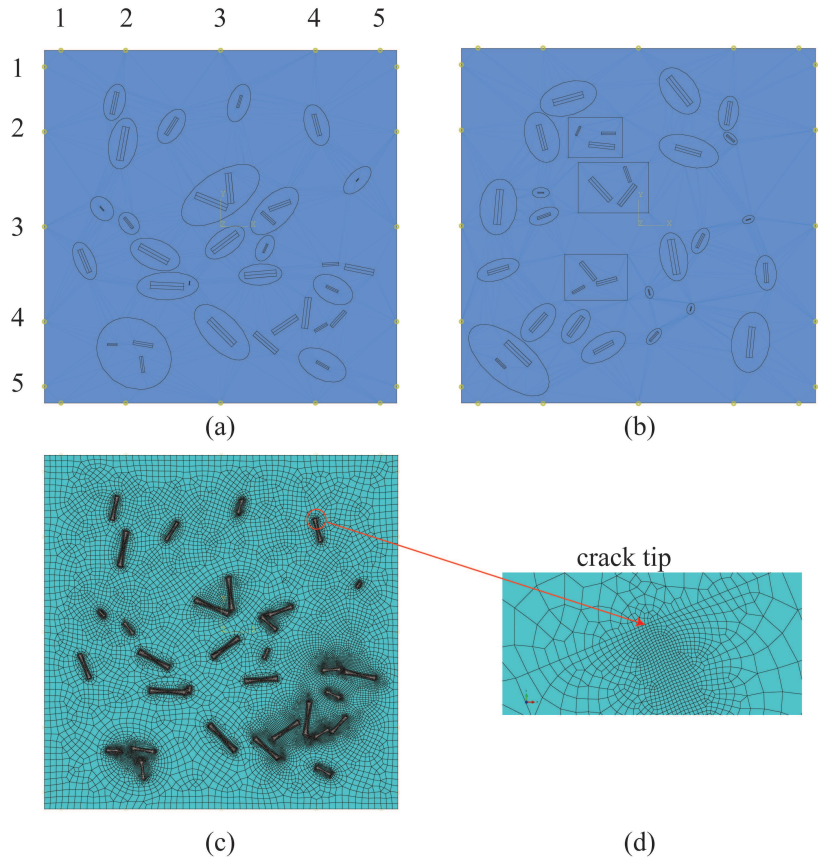

Figure 6.3: Two-dimensional models with frictional microcracks generated in ABAQUS: (a) Model 1. (b) Model 2. (c) Finite element mesh generated for model 1. (d) Finer mesh around a crack tip. The circle and the arrow were drawn in later, manually and approximately, for visualization. In both (a) and (b), the ellipses and rectangles around the cracks denote sub-regions used for manual mesh refinement, and have no subsequent relevance; and the points numbered 1 through 5 will be used as Gauss points for integration, as described later.

enough for the computed dissipation values to converge satisfactorily. An advantage of conducting the simulations in ABAQUS is that the dissipation is computed within the software package and requires no new programming.

A key point here is that we are interested in an underlying *scalar* model of hysteretic behavior, as in both the Bouc-Wen model as well as our recent work in chapter 2. Accordingly, for each load case, $f(t)$ is taken as an effective scalar load. We now consider the corresponding scalar displacement and associated hysteresis loops.

Table 6.1: Load cases considered for the finite element simulation

Case	σ_x (MPa)	σ_y (MPa)	$f(t)$
1	-20	100	$\sin 2\pi t$
2	-50	100	$\sin 2\pi t$
3	-70	100	$\sin 2\pi t$
4	-100	100	$\sin 2\pi t$
5	-120	100	$\sin 2\pi t$
6	-160	100	$\sin 2\pi t$
7	150	-200	$\sin 2\pi t + 0.4 \sin 8\pi t$
8	150	-200	$\sin 2\pi t + 0.4 \sin 10\pi t$
9	150	-200	$\sin 2\pi t + 0.5 \sin 12\pi t$
10	150	-200	$\sin 2\pi t + 0.5 \sin 14\pi t$
11	150	-200	$\sin 2\pi t + 0.3 \sin 16\pi t$
12	150	-200	$\sin 2\pi t + 0.3 \sin 18\pi t$

6.2.2 Scalar displacement and hysteresis loop

Pseudostatic analyses of the above finite element models give the amounts of frictional energy loss under various cyclic stresses. To generate the corresponding hysteresis loops for each load case, we identify a suitable scalar displacement *via* the work done by external forces, as follows.

Note the five Gauss integration points on the edges of the plate in Figures 6.3(a) and (b). The meshes were generated with nodes coinciding with these points. From the finite element simulation results, we take the x displacements for the vertical edges and the y displacements for the horizontal edges at these Gauss points. We then find the average displacements of these edges using the Gauss quadrature rule (see e.g., [69]). The net average displacements (or more correctly, average stretches) in the x and y directions are

$$u_x = u_{\text{right}} - u_{\text{left}},$$

$$u_y = u_{\text{top}} - u_{\text{bottom}},$$

where u_{right}, u_{left} are average x displacements of the right and the left edges respec-

tively; and u_{top} and u_{bottom} are average y displacements of the top and the bottom edges respectively. The work done per unit area on the external surfaces by the external tractions in a small incremental displacement is then

$$dW = \sigma_x f(t)\, du_x + \sigma_y f(t)\, du_y = f(t)\, d\xi,$$

say, whereby

$$\xi = \sigma_x u_x + \sigma_y u_y \tag{6.2}$$

is seen to be the appropriate generalized scalar displacement of the system[3]. To study the hysteretic response, we should plot $f(t)$ against $\xi(t)$ for each load case. The results do show hysteresis. However, the net dissipation is tiny and the loops are too thin to show details unless some artificial magnification is done for the vertical separation (recall Figure 6.1(a)). Accordingly, we subtract a bilinear term from $f(t)$ to thicken the loops; that is, for each load case, we define a new

$$\bar{f}(t) = f(t) - a\,\xi(t) - b\,|\xi(t)|, \tag{6.3}$$

and plot $\bar{f}(t)$ against $\xi(t)$. There is some arbitrariness in the choices of a and b. We used the following formula. In each case, i.e., for every subfigure for both FE models, first a least squares fit was numerically computed for

$$f(t) = \tilde{a}\,\xi(t) + \tilde{b}\,|\xi(t)|,$$

and then a and b in Eq. (6.3) were chosen to be 0.999 times $\tilde{a}$ and $\tilde{b}$ respectively. The 0.999 instead of 1.000 was used to retain a small average trend in the hysteresis loops, which makes them look a little more pleasing.

Some common qualitative features are seen in the results, given for all 12 load cases for models 1 and 2 in Figures 6.4 and 6.5 respectively. Note that the hysteresis loops are pinched at the origin, unlike those in Figure 6.1 (this pinched nature is

[3]Here, ξ has the same units as dW because $f(t)$ is dimensionless; however, our interest is in the loop shapes, and so the units play no direct role.

expected in the present context because the loading passes through a stress-free state, but it is mentioned explicitly because of its relevance to hysteretic models in structural damping). For the load cases 7 through 12, partial unloadings cause smaller loops, as observed in Figures 6.4 and 6.5.

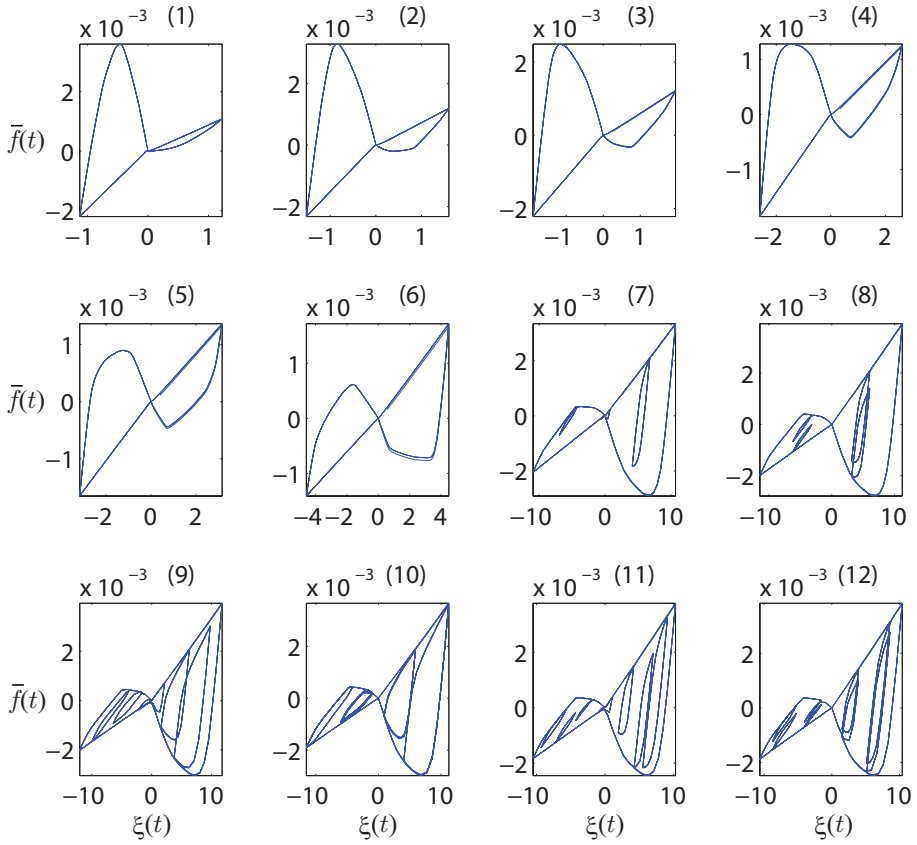

Figure 6.4: Hysteresis loops obtained from Model 1 for the twelve load cases considered in Table 6.1. The load case numbers from the table reappear over the corresponding subfigures.

Since we have used randomly assigned friction coefficients μ at the various crack locations, it is natural to ask what happens if μ is uniform across the cracks. What differences might we expect between the hysteretic behaviors for small and large μ? For given μ, how consistent are the results for the two geometries? These are legitimate questions although they divert us a little from our main goal of motivating and developing a new simple hysteresis model for structural vibrations; so, for completeness, these questions are addressed in Appendices K and L.

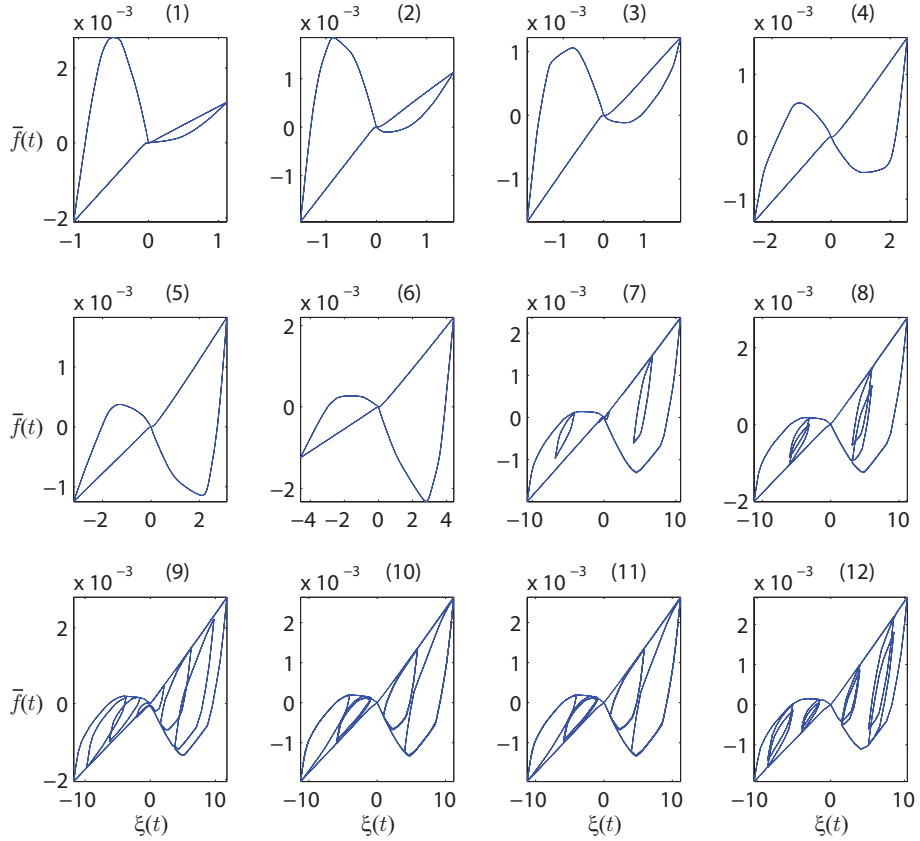

Figure 6.5: Hysteresis loops obtained from Model 2 for the twelve load cases considered in Table 6.1. The load case numbers from the table reappear over the corresponding subfigures.

6.3 Empirical model for the hysteresis loops

We now turn to an empirical model of the observed hysteretic behavior that might be useful for modeling frictional damping in structural dynamics, e.g., something significantly more realistic than simply assigning modal damping values, which is commonly done at present.

We observe that the hysteresis loops obtained in Figures 6.4 and 6.5 have some qualitative resemblance with the loops given by Reid [15] and Muravskii [59]. Reid's model is an *ad hoc* scalar equation that specifies the hysteretic force to be

$$f = k(1 + \eta_0 \operatorname{sgn}(x\dot{x}))x, \tag{6.4}$$

where x is a displacement, k is a stiffness, and η_0 is a dissipation coefficient. Figure

6.6(a) shows a typical response from Eq. (6.4), the hysteresis loop being a pair of triangles meeting at the origin. Upon loading and unloading, each triangle is traversed clockwise, there is a slope discontinuity at the origin, and the area enclosed represents a rate-independent energy dissipation. Muravskii's *ad hoc* desired correction to Reid's loop is sketched in Figure 6.6(b). However, as explained by Spitas [70], Muravskii's suggested added spring element does not quite give the sort of triangular loop he desires.

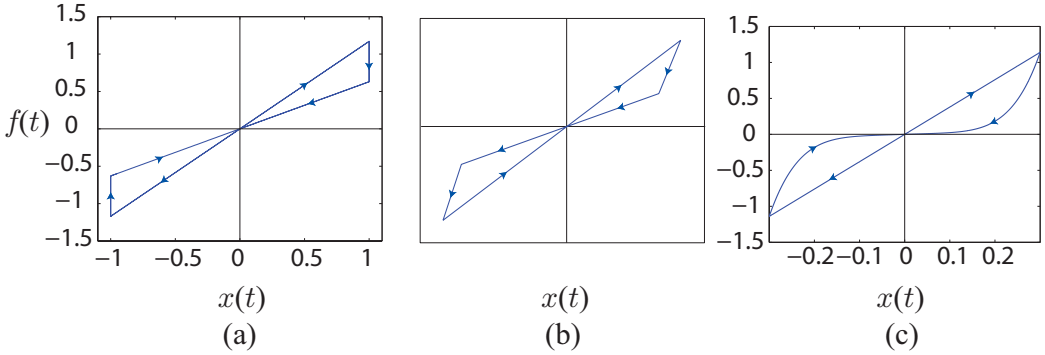

Figure 6.6: (a): Hysteresis loop from the Reid model, Eq. (6.4). $f(t)$ is discontinuous at the corners. (b) Muravskii's [59] desired hysteresis loop. (c) Loop obtained from Eq. (6.5), with $K_0 = 4$, $\theta_m = 2$, $\tilde{\beta} = 1.8$, and $\epsilon = 10^{-4}$.

An improvement upon Reid and Muravskii's proposals is offered by our following new empirical, scalar, rate-independent model:

$$\dot{\theta} = \frac{K_0}{|x| + \epsilon} \Big(\theta_m + \tilde{\beta} \operatorname{sgn}(x\dot{x}) - \theta \Big) \cdot |\dot{x}|, \tag{6.5}$$

where x is the input displacement, θ is an internal variable, and output

$$f = \theta\, x.$$

The model has 4 parameters assumed to obey the following restrictions: $K_0, \tilde{\beta}, \theta_m > 0$, and $0 < \epsilon \ll 1$. Here ϵ is a small regularization parameter to help cross over the singularity at $x = 0$, which is in turn needed to produce a sudden slope change at zero. The sort of loop produced by Eq. (6.5) is shown in Figure 6.6(c).

Figure 6.7 shows some more hysteresis loops obtained from Eq. (6.5). In these

examples, the inputs $x(t)$ were taken to be $\sin 2\pi t + h(t)$, with $h(t) = 0.4 \sin 8\pi t$, $0.4 \sin 10\pi t$, $0.5 \sin 12\pi t$, $0.5 \sin 14\pi t$, $0.3 \sin 16\pi t$ and $0.3 \sin 18\pi t$ in the six different cases shown.

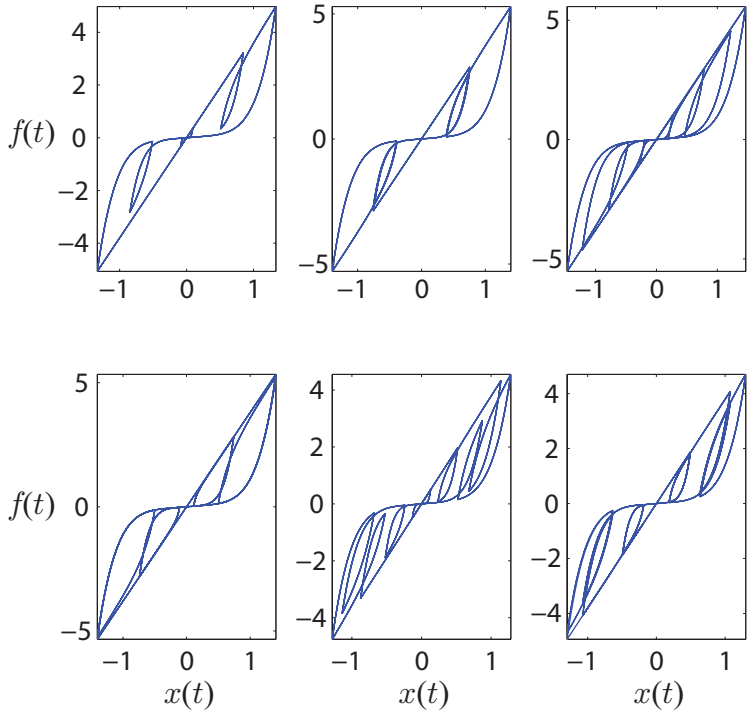

Figure 6.7: Hysteresis loops from two-frequency inputs, using Eq. (6.5).

It may be noted that Eq. (6.5) does not predict minor loops under very small load reversals. This issue was discussed at some length in chapter 2, for the loops shown in Figure 6.1(e). However, in the present context, Eq. (6.5) offers significant advantages over Reid's [15] and Muravskii's [59] proposals, and captures key qualitative features of Figures 6.4 and 6.5. In particular, Reid's model predicts a nonzero jump in the hysteretic output even upon infinitesimal load reversals, while Eq. (6.5) gives a continuous transition. Muravskii's proposal suggests a continuous transition, but as mentioned above, there is no equation given by him that actually produces the figure he desires.

For more detailed assessment, a direct comparison with the results of Figure 6.4 is now presented. Note that the loops obtained in Figure 6.4 are asymmetric due to the finite number of randomly placed cracks in the plate model, while the empirical hysteresis model gives loops symmetric about the origin. For this reason,

comparison will be made with the loops of Figure 6.4 restricted to the first quadrant. Additionally, each subfigure of Figure 6.4 has implicit in it a different shifting and scaling in the form of different a and b in Eq. (6.3). Therefore, the parameters K_0, $\tilde{\beta}$ and θ_m are to be separately fitted for each subfigure using only first quadrant data and Eq. (6.5). Final results are shown in Figure 6.8 (for parameter values used, see Table M.1 in Appendix M).

It is seen that the simple empirical model of Eq. (6.5) does a fairly good job of mimicking the results from finite element computations. In the first few subfigures, the finite element results have loops that are a little more angular while the empirical fitted loops are rounder, but we expect that as more cracks are included the finite element loops will get rounder. The last two subfigures, in their top right corners, show that the empirical model has some qualitative errors upon unloading due to its inability to fully capture minor loops. This issue was discussed in the context of the Bouc-Wen model earlier (see Figure 6.1(d)), and cannot be avoided completely in hysteresis models with only one internal variable (see discussion in section 2.1). Overall, considering the simplicity of Eq. (6.5), the quality of the fits is good.

Finally, it may easily be shown that in the single-frequency case, for amplitudes that are much larger than ϵ, Eq. (6.5) predicts a per-cycle dissipation that follows Eq. (6.1) with

$$D = \frac{2\tilde{\beta}K_0}{K_0 + 2}\, x_m^2,$$

where x_m is the input displacement amplitude.

6.4 Concluding remarks

The precise nature of the hysteresis in the stress strain relation of a material plays an important role in determining how it dissipates energy under complex time-varying deformations. Thus, the shape of the hysteresis loop is of both academic and practical interest. Typical hysteresis loops observed in material damping, as in Rowett's experiment [3], as well as hysteresis loops in some well known models (like

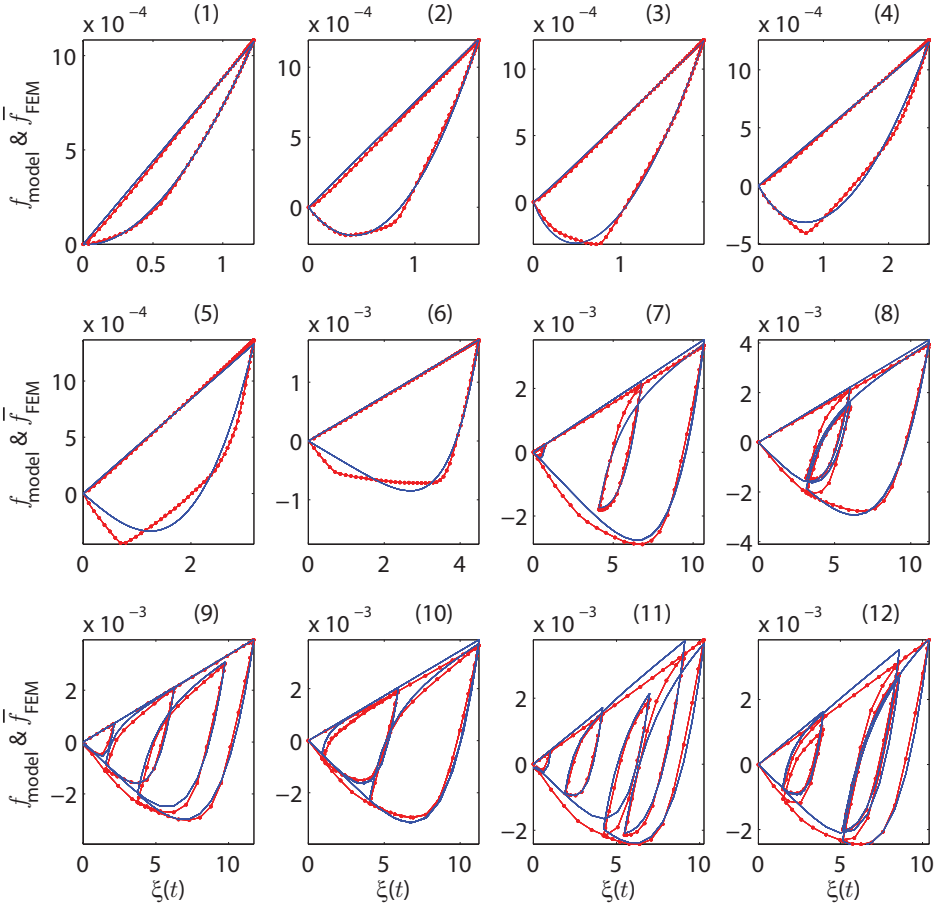

Figure 6.8: Hysteresis loops of Figure 6.4, fitted individually using Eq. (6.5). Only first quadrant portions are considered. The red solid lines with dots denote FE results; the blue solid lines without dots are the fitted curves.

the Bouc-Wen model [7, 8], and even our recently presented model (chapter 2)), all have nonzero thickness at zero deformation (or displacement input).

In contrast, the loops proposed by Reid [15] and Muravskii [59] are pinched at the origin. From a vibration damping viewpoint the latter loops seemed to be prompted merely by convenience, and apparently had no physical basis. Here, through finite element simulations of a plate with many small random frictional cracks, we have shown a possible physical basis for such hysteresis loops. In addition to being pinched at the origin, our loops also exhibit some other peculiarities, such as moving out from the origin along a well defined upper slope but relaxing more smoothly toward a lower slope while unloading. An anonymous reviewer of [58] pointed out that the pinched hysteresis loops here are obvious consequences of the frictional crack based

dissipation model, since the origin represents an external-traction-free state in which we do not expect internal cracks to have locked-in frictional tractions (within a limit: see [71]). However, we have taken special note of this pinched nature because of our interest in structural vibration damping models, since in that community this aspect of hysteretic frictional damping is not widely recognized.

Finally, we have presented a new scalar evolution equation that captures essential features of such hysteresis loops. This new simple model can be used for theoretical studies of damping in frictional systems under multi-frequency deformations. In particular, unlike in linear viscous dissipation, dissipation rates due to different frequencies can interact, and a new possible way to model such interactions has been developed in this chapter.

Chapter 7

Conclusions

We have developed new low-dimensional descriptions of high-dimensional rate-independent frictional hysteretic systems.

In chapter 2, we have developed a new unconventional approach to derive a reduced order model from a high-dimensional frictional system studied. The results we have obtained in chapter 2 are of academic interest because of the novel approach and application. The reduced order model obtained there is somewhat complicated and not very useful for practical purposes. Yet, the work both provides fresh insights as well as access to internal states that are neither incorporated in typical empirical models nor available in experiments. The model also captures minor loops in the hysteresis, which the Bouc-Wen model does not. In this way, this work has opened up interesting lines of new research into the mathematics and physics of hysteresis, which we have applied in our subsequent work.

In chapter 3, we have studied a new high-dimensional system that has offered several advantages over the model in chapter 2, e.g., analytically tractable POD based modes, a minimal number of states (two), and a fewer fitted parameters. The model now allows practical parameter fitting to match a range of hysteretic data. This model is now highly competitive for application in several nonlinear dynamical systems with friction. For example, the model can be used as a constitutive model for hysteretic damping in structures (beam, plate), as a vibration absorber with hysteretic damping. The model can be used in control systems with friction, and

new control strategies may be developed for such systems. A minor flaw still remains in the model. The model apparently cannot capture hysteresis loops with two or more distinct slope changes even with an increase in the number of states. This leaves room for further improvement. Future work may lead to a new approach that will eliminate this flaw in the model.

In chapter 4, we have successfully used the foregoing two state model to describe hysteresis in finite element models of frictional lap joints. An excellent match is obtained between the two state model and normalized hysteresis loops obtained *via* FE simulations. Interestingly, we have found that for single-bolted joints, the same hysteresis model fit works well over a range of friction coefficients and bolt preloads. The main contribution of the chapter is that we have offered a new low-dimensional alternative to high-dimensional Iwan models that are often used to describe hysteresis in joints. Our model is computationally less expensive and more efficient in capturing minor loops. In future our model may become accepted among the researchers who are currently using Iwan models.

In chapter 5, we have given an explicit approximation for the slip direction in the two state model. The approximation gives an excellent match with the exact solution. This new approximation also may help to develop new insights into the two state model. It is essentially an academic exercise at this stage however.

In chapter 6, first through FE simulations of elastic plates with several frictional microcracks, we have obtained hysteresis loops that are pinched at the origin. Such pinched loops partially resemble an *ad hoc* model due to Reid (1956). We have proposed a simple scalar evolution equation that captures key qualitative aspects of the pinched loops obtained from the FE simulations. The significant point of this model is that the hysteretic behavior it shows is qualitatively different from the hysteresis loops observed from Rowett's experiment, or from the Bouc-wen model, or from the models we have developed and used in the first five chapters of this thesis. In future, this model can be used for theoretical studies of damping in materials with frictional microcracks, e.g., ceramics, concrete, rocks. This model may help

to develop a constitutive description for damping in those materials, thereby also providing physical insight into the meaning of the model parameters. In this way the new pinched hysteresis loop model opens a new interesting line of research.

Appendices

Appendix A

Derivation of frictional system equation and its LCP form

We consider the system shown in Figure 2.3. Suppose first that the blocks have masses $m_1,\ m_2,\ m_3, \cdots, m_N$. The kinetic energy (KE) and the potential energy (PE) of the system are as below:

$$KE = \frac{1}{2}\sum_{i=1}^{N} m_i\, \dot{x_i}^2,$$

$$PE = \frac{1}{2}x^T K x,$$

where x is an N-dimensional vector of generalized coordinates and K is a symmetric, positive definite matrix of size $N \times N$. Lagrange's equations of motion (see, e.g., [30]) are

$$M\ddot{x} + Kx = bf(t) + F,$$

where M is a diagonal matrix whose i^{th} element is m_i; b is a column matrix whose i^{th} element is b_i as indicated in Figure 2.3; and F is an N-dimensional vector whose i^{th} element is F_i as indicated in the figure. Here, the system is massless and the force vector F arises from Coulomb friction, and so we have

$$\mu\,\mathrm{sgn}(\dot{x}) + Kx = bf(t). \tag{A.1}$$

In the above, μ is an $N \times N$ diagonal matrix with positive elements. Premultiplying Eq. (A.1) by μ^{-1} yields

$$\mathrm{sgn}(\dot{x}) + \mu^{-1}Kx = \mu^{-1}bf(t),$$

which we write as

$$-\tilde{F} + \tilde{K}x = \tilde{b}f(t), \tag{A.2}$$

where $\mu^{-1}K = \tilde{K}$, $\mu^{-1}b = \tilde{b}$, and

$$\mathrm{sgn}(\dot{x}) = -\tilde{F}. \tag{A.3}$$

We now cast an incremental form of Eq. (A.2) into LCP form. This way of solving friction problems is well known (e.g., [31]) but is described here for completeness.

We introduce two new nonnegative variables U and V, defined elementwise as follows. Let $U = -\dot{x}$ if $\dot{x} < 0$, and $U = 0$ otherwise; and $V = \dot{x}$ if $\dot{x} > 0$ and $V = 0$ otherwise. We then have the complementarity relations

$$U \geq 0, \;\; V \geq 0, \;\; U^T V = 0,$$

and observe that

$$\dot{x} = V - U.$$

Next, we observe that $|\tilde{F}| \leq 1$. We introduce two more new nonnegative variables S and R, defined elementwise as $S = 1 + \tilde{F} \geq 0$ and $R = 1 - \tilde{F} \geq 0$.

It follows that when (for any element) $\dot{x} > 0$, and $V > 0$, then $\tilde{F} = -1$ (see Eq. (A.3)) or $S = 0$. Similarly, when $\dot{x} < 0$, and $V = 0$, then $\tilde{F} = 1$, or $S > 0$. Thus, V and S satisfy the complementarity relation $V^T S = 0$. It can be similarly seen that $U^T R = 0$.

We now note that

$$S + R = 2$$

$$S - R = 2\tilde{F}$$

Considering a small time increment Δt, Eq. (A.2) becomes

$$-\Delta\tilde{F} + \tilde{K}\Delta x = \tilde{b}\Delta f \tag{A.4}$$

Now, $\Delta x = (V - U)\,\Delta t$ gives

$$-\Delta\tilde{F} + \tilde{K}\Delta t(V - U) = \tilde{b}\Delta f, \tag{A.5}$$

where we write

$$\Delta\tilde{F} = \frac{\Delta S - \Delta R}{2} = \frac{(S_{k+1} - S_k) - (R_{k+1} - R_k)}{2}, \tag{A.6}$$

and consider writing

$$\tilde{b}\Delta f = \tilde{b}(f_{k+1} - f_k).$$

However, x does not appear explicitly in Eq. (A.5). To avoid possible drift in x, we retain x by writing

$$\tilde{b}\Delta f = \tilde{b}f_{k+1} - \tilde{K}x_k + \frac{S_k - R_k}{2}. \tag{A.7}$$

Finally, Eqs. (A.5), (A.6) and (A.7) are combined and rearranged to give

$$\begin{bmatrix} I & I \\ -\frac{I}{2} & \frac{I}{2} \end{bmatrix} \begin{Bmatrix} S_{k+1} \\ R_{k+1} \end{Bmatrix} - \begin{bmatrix} 0 & 0 \\ -\tilde{K}\Delta t & \tilde{K}\Delta t \end{bmatrix} \begin{Bmatrix} V_{k+1} \\ U_{k+1} \end{Bmatrix} = \begin{Bmatrix} 2 \\ \tilde{b}f_{k+1} - \tilde{K}x_k \end{Bmatrix}. \tag{A.8}$$

The linear complementarity problem (or LCP) considers given matrices $\tilde{M}$ of size $p \times p$ and $\tilde{q}$ of size $p \times 1$, and seeks vectors $\tilde{w}$ and $\tilde{z}$ which satisfy

$$\tilde{w} - \tilde{M}\tilde{z} = \tilde{q},$$

$$\tilde{w}_i \geq 0; \tilde{z}_i \geq 0;$$

$$\tilde{w}_i \tilde{z}_i = 0.$$

Noting the complementarity relations between S and V, and between R and U, we find that Eq. (A.8) is an LCP with

$$\tilde{M} = \begin{bmatrix} I & I \\ -\frac{I}{2} & \frac{I}{2} \end{bmatrix}^{-1} \begin{bmatrix} 0 & 0 \\ -\tilde{K}\Delta t & \tilde{K}\Delta t \end{bmatrix},$$

$$\tilde{q} = \begin{bmatrix} I & I \\ -\frac{I}{2} & \frac{I}{2} \end{bmatrix}^{-1} \begin{Bmatrix} 2 \\ \tilde{b}\Delta f - \frac{S_k - R_k}{2} \end{Bmatrix}.$$

The LCP can be numerically solved using Lemke's algorithm, and our solutions were obtained using an implementation of the same given by [26] in their "CompEcon" toolbox. In our solutions, we start from an initial state, choose a time increment Δt, and march forward in time to obtain a solution. Redoing with a smaller Δt and obtaining the same results indicates that the solution is sufficiently accurate for our purposes.

Appendix B

LCP and ODE solutions compared

An anonymous reviewer of [32] asked about the possibility of other solutions than what the LCP predicts. It is true that such high-dimensional frictional systems can have non-unique solutions. The aim of our work has been to *derive* a low-dimensional hysteresis model rather than probe the full complexities of the original high-dimensional model. Nevertheless, here we demonstrate that the LCP solution is close to the solution obtained from a system of ODEs (namely Eq. (3.5)) obtained by regularizing the frictional forces in the model.

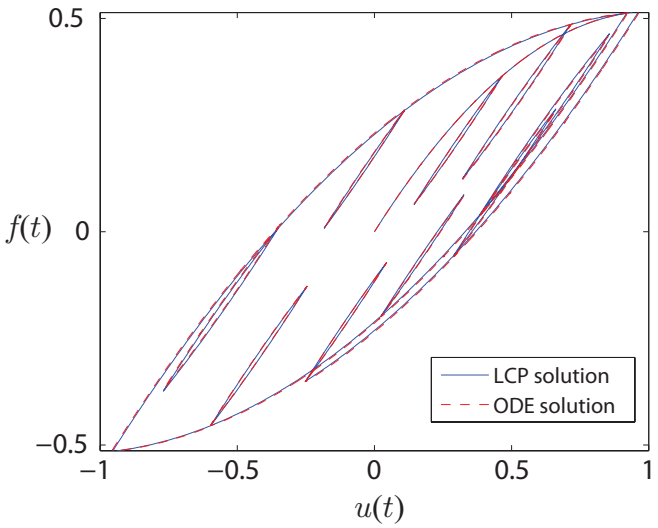

Figure B.1: Hysteresis curves obtained for a 50-dimensional system from LCP and ODE solutions.

Figure B.1 shows a comparison between LCP and ODE results from Eqs. (3.2)

and (3.5). Here, we have used $n = 50$, $\mu_0 = 0.02$, and $u(t)$ as in Eq. (3.6). We also chose $\epsilon = 0.003$ in Eq. (3.5). Both the solutions match quite well. The LCP solution is much faster and therefore adopted for larger n.

Appendix C

Slip direction η

C.1 Finding the slip direction η

We have been able to substantially simplify the calculation of the slip direction η, compared to our original method developed in section 2.3.3. Recall section 3.3.6, where it was explained that using an orthogonal transformation we can take A to be diagonal:

$$A = \bar{\mu} \begin{bmatrix} \sigma & 0 \\ 0 & 1 \end{bmatrix}.$$

We reproduce Eq. (3.18) below:

$$\frac{A}{\sqrt{\eta^T A \eta}}\eta - \bar{\lambda}\eta + c = 0.$$

Let $\bar{\lambda} = (1/\sqrt{\eta^T A \eta})\,\hat{\lambda}$. Then,

$$\frac{1}{\sqrt{\eta^T A \eta}}(A - \hat{\lambda} I)\eta = -c \tag{C.1}$$

or

$$\frac{1}{\sqrt{\eta^T A \eta}} \left(\bar{\mu} \begin{bmatrix} \sigma & 0 \\ 0 & 1 \end{bmatrix} - \hat{\lambda} \begin{bmatrix} 1 & 0 \\ 0 & 1 \end{bmatrix} \right) \begin{Bmatrix} \eta_1 \\ \eta_2 \end{Bmatrix} = - \begin{Bmatrix} c_1 \\ c_2 \end{Bmatrix}. \tag{C.2}$$

From Eq. (C.2)

$$\eta_1 = -\frac{c_1\sqrt{\eta^T A\eta}}{(\bar{\mu}\sigma - \hat{\lambda})} \tag{C.3}$$

and

$$\eta_2 = -\frac{c_2\sqrt{\eta^T A\eta}}{(\bar{\mu} - \hat{\lambda})}. \tag{C.4}$$

Since $\eta^T A\eta = \bar{\mu}(\eta_1^2\sigma + \eta_2^2)$, by Eqs. (C.3) and (C.4) we have

$$\bar{\mu}\left(\frac{c_1^2\sigma}{(\bar{\mu}\sigma - \hat{\lambda})^2} + \frac{c_2^2}{(\bar{\mu} - \hat{\lambda})^2}\right) = 1,$$

which yields

$$(\bar{\mu}\sigma - \hat{\lambda})^2(\bar{\mu} - \hat{\lambda})^2 - \bar{\mu}(\bar{\mu} - \hat{\lambda})^2 c_1^2\sigma - \bar{\mu}(\bar{\mu}\sigma - \hat{\lambda})^2 c_2^2 = 0. \tag{C.5}$$

Now, somewhat fortuitously, we consider the 4×4 matrix

$$B = \begin{bmatrix} A & cc^T \\ A & A \end{bmatrix}. \tag{C.6}$$

It turns out that $\hat{\lambda}$ of Eq. (C.5) is an eigenvalue of the above B. Setting

$$\det\left(\begin{bmatrix} A - \hat{\lambda}I & cc^T \\ A & A - \hat{\lambda}I \end{bmatrix}\right) = 0,$$

we obtain

$$\det\left((A - \hat{\lambda}I)^2 - Acc^T\right) = 0. \tag{C.7}$$

We now use a matrix determinant lemma (e.g., [37]) which says that for a square matrix H and column matrices g and h of appropriate sizes,

$$\det\left(H + gh^T\right) = \det(H)\left(1 + h^T H^{-1} g\right).$$

By this lemma, Eq. (C.7) gives

$$\det(A-\hat{\lambda}I)^2 \cdot \left(1 - c^T[(A-\hat{\lambda}I)^2]^{-1}Ac\right) = 0$$

or

$$(\bar{\mu}\sigma - \hat{\lambda})^2(\bar{\mu}-\hat{\lambda})^2 \cdot \left(1 - \frac{\bar{\mu}\sigma c_1^2}{(\bar{\mu}\sigma-\hat{\lambda})^2} - \frac{\bar{\mu}c_2^2}{(\bar{\mu}-\hat{\lambda})^2}\right) = 0 \tag{C.8}$$

which, upon multiplying the terms out, gives Eq. (C.5). Thus, $\hat{\lambda}$ is an eigenvalue of B.

Now consider the corresponding eigenvectors

$$\begin{bmatrix} A-\hat{\lambda}I & cc^T \\ A & A-\hat{\lambda}I \end{bmatrix} \begin{Bmatrix} \psi \\ \zeta \end{Bmatrix} = \begin{Bmatrix} 0 \\ 0 \end{Bmatrix}, \tag{C.9}$$

where ψ and ζ are 2×1. From Eq. (C.9),

$$(A-\hat{\lambda}I)\psi + cc^T\zeta = 0, \tag{C.10}$$

and

$$A\,\psi + (A-\hat{\lambda}I)\zeta = 0. \tag{C.11}$$

Premultiplying Eq. (C.10) with ζ^T gives

$$\zeta^T(A-\hat{\lambda}I)\psi + (c^T\zeta)^2 = 0, \tag{C.12}$$

while premultiplying Eq. (C.11) with ψ^T and then transposing gives

$$\psi^T A\psi + \zeta^T(A-\hat{\lambda}I)\psi = 0. \tag{C.13}$$

From Eqs. (C.12) and (C.13), we obtain

$$c^T\zeta = \pm\sqrt{\psi^T A\psi}. \tag{C.14}$$

Dividing Eq. (C.10) by the scalar quantity $c^T\zeta$ and then substituting Eq. (C.14), we obtain

$$\frac{1}{\sqrt{\psi^T A\psi}}(A - \hat{\lambda}I)(\pm\psi) = -c. \tag{C.15}$$

Since ψ is part of an eigenvector is can be scaled such that $\psi^T\psi = 1$, and the above equation remains unaffected. However, ψ remains indeterminate up to a "$\pm$" sign. Comparing Eqs. (C.15) and (C.1), we find $\eta = \pm\psi$.

Thus, the algorithm for computing η is as follows. First, we construct matrix B as in Eq. (C.6). We find its eigenvalues $\hat{\lambda}$. For every real $\hat{\lambda}$, we find the corresponding portion of its eigenvector, ψ, normalized to $\psi^T\psi = 1$, and with sign chosen such that $\psi^T c \leq 0$. Searching through all such ψ (numbering at least 2 as shown in section 2.3.3, and at most $2m$ which is the size of B), we select the one that minimizes $\sqrt{\psi^T A\psi} + \psi^T c$. That ψ is the slip direction η.

C.2 Matlab code for computing η

The Matlab code below finds the slip direction η given a diagonal A and 2×1 vector c.

```
function eta=slip(A,c)
m=length(c); B=[A,c*c';A,A];
[v,d]=eig(B); E=[]; S=[]; d=diag(d);
for k=1:2*m
    if imag(d(k))==0
        temp=v(1:m,k);
        temp=-temp/norm(temp)*sign(temp'*c);
        E=[E,temp]; S=[S,sqrt(temp'*A*temp)+temp'*c];
    end
end
[m,n]=min(S);
eta=E(:,n);
```

Appendix D

A two mass system with a hysteretic damper

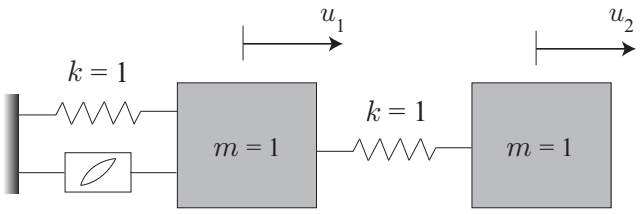

Figure D.1: A two degree of freedom spring-mass system with a hysteretic damper.

Figure D.1 shows a two degree of freedom oscillator. There are two unit masses attached by springs of unit stiffness as shown in the figure. A two state hysteretic damper is attached to the first mass. The displacements of the masses are taken as u_1 and u_2, with u_1 being the input to the hysteretic damper.

We arbitrarily choose the parameter values

$$A = 0.117 \times 10^{-3} \begin{bmatrix} 0.0638 & 0 \\ 0 & 1 \end{bmatrix}, \quad \bar{K} = \frac{1}{500} \begin{bmatrix} 1 & 0 \\ 0 & 1 \end{bmatrix}, \quad \text{and} \quad \bar{b} = \begin{Bmatrix} 0.0326 \\ 0.0068 \end{Bmatrix}.$$

Equations of motion of the two masses are

$$\begin{aligned} \ddot{u}_1 + 2\,u_1 - u_2 + f &= 0, \\ \ddot{u}_2 - u_1 + u_2 &= 0, \end{aligned} \tag{D.1}$$

where f is the hysteretic damper force. In addition, there are two first order differential equations for the two-dimensional state q, as given earlier in section 3.3.6. The hysteretic force f is calculated at each instant following Eq. (3.24),

$$f = u_1 - q^T \bar{b}.$$

Figure D.2(a) shows the system response for an arbitrary initial condition. The

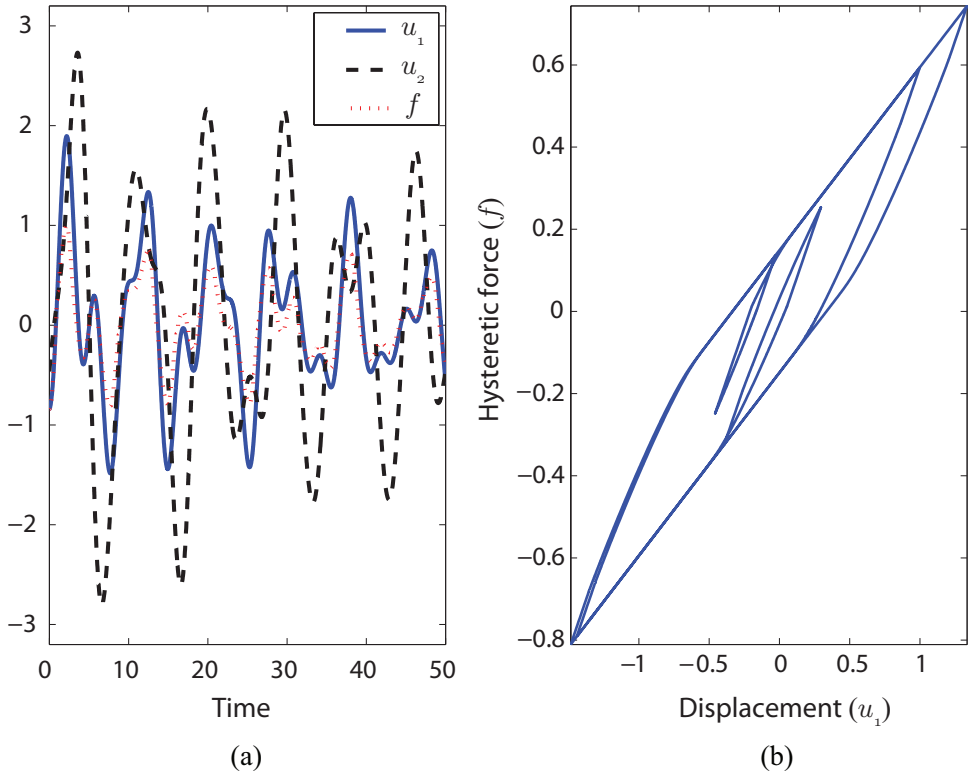

Figure D.2: (a) Displacements u_1, u_2, and hysteretic force f vs. time. (b) Hysteresis between u_1 and f for a portion of the computed solution.

blue solid line is displacement u_1, the black dashed line is the displacement u_2, and the red dotted line is the hysteretic force f. For this two degree of freedom system, the response has more than one frequency. Consequently, u_1 shows short reversals

within larger oscillations. Consequently the hysteretic force shows minor reversals (see Figure D.2(b)).

In future work, in the dynamics of the frictionally damped oscillator, it may be interesting to compare similar systems with hysterteretic models of varying degrees of complexity.

Appendix E

Fitted parameters for section 3.5

Numerical values of the fitted parameters for section 3.5 are given in Tables E.1 and E.2.

Table E.1: Fitted parameters for the cases of Figure 3.7

Case	$\bar{\mu}$	σ	$\bar{\alpha}$	$\bar{b}_1$	$\bar{b}_2$	k_s
1	0.0176	0.1425	0.2222	0.2047	0.2458	−0.2481
2	0.1164	0.0047	0.1879	0.0175	0.3734	0.1515
3	0.1506	0.9925	1.4728	−1.7047	−1.4578	2.5444

Table E.2: Fitted parameters for the cases of Figure 3.9

Case	$\bar{\mu}$	σ	$\bar{\alpha}$	$\bar{b}_1$	$\bar{b}_2$	k_s
1	0.2039	0.0707	2.4733	0.6868	−1.0032	−0.0319
2	0.0503	0.0152	0.3736	1.2695	−0.2733	3.8860

Appendix F

Energy dissipation per cycle for the Bouc-Wen model and the two-state model

We present numerical results for dissipation per cycle for the Bouc-Wen model and the two-state model under a single-frequency input, and under a two-frequency input.

Recall the Bouc-Wen model (Eq. (2.1))

$$\dot{z} = \alpha_1 \dot{u} - \alpha_2 |\dot{u}||z|^{n-1} z - \alpha_3 \dot{u}|z|^n, \tag{F.1}$$

where $\alpha_1 > 0$, $\alpha_2 > 0$, $\alpha_3 \in [-\alpha_2, \alpha_2]$ and $n > 0$.

For our numerical simulations, we consider (i) a single-frequency input

$$u(t) = \sin 2\pi t, \tag{F.2}$$

and (ii) a two-frequency input

$$u(t) = \sin 2\pi t + 0.6 \sin 8\pi t. \tag{F.3}$$

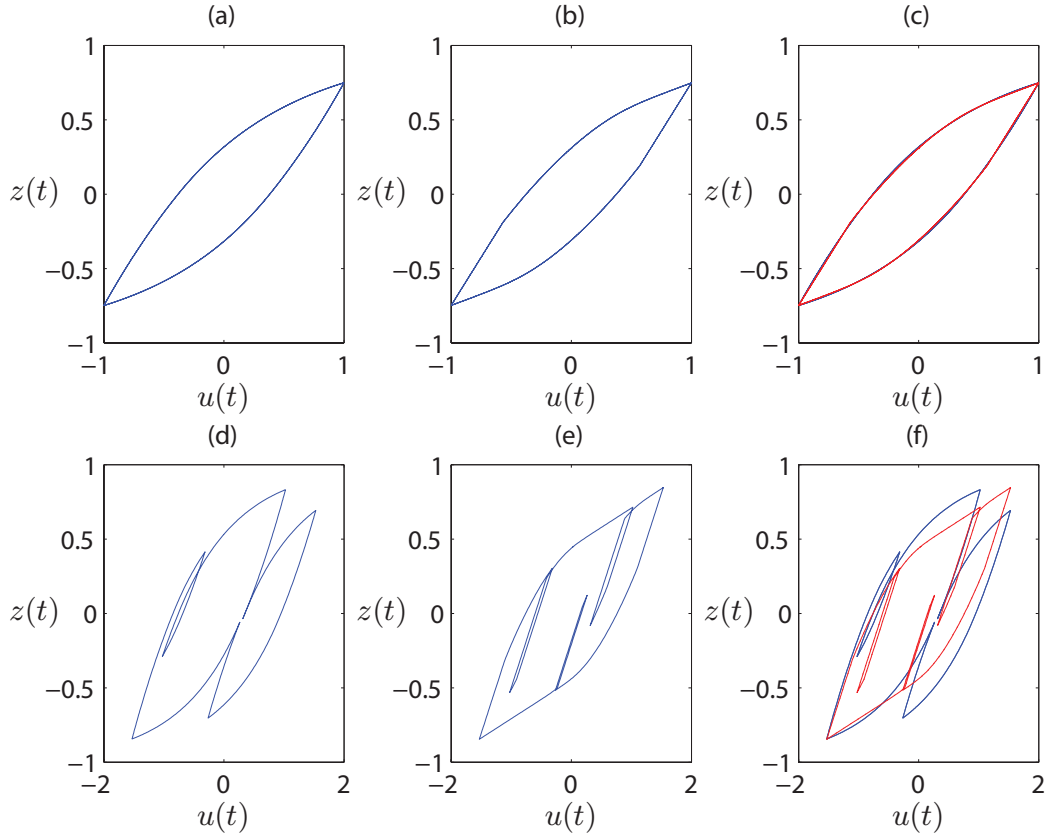

Figure F.1: (a) The Bouc-Wen model under the single-frequency input in Eq. (F.2). (b) The two-state model under the single-frequency input in Eq. (F.2). (c) The hysteresis loops in (a) and (b) are compared. Bouc-Wen model (blue), two-state model (red). (d) The Bouc-Wen model under the two-frequency input in Eq. (F.3). (e) The two-state model under the two-frequency input in Eq. (F.3). (f) The hysteresis loops in (d) and (e) are compared. Bouc-Wen model (blue), two-state model (red). Parameters used for the Bouc-Wen model: $\alpha_1 = 1$, $\alpha_2 = 0.8$, $\alpha_3 = 0.2$ and $n = 1$. Parameters used for the two-state model: $\bar{\mu} = 1$, $\sigma = 0.1524$, $\bar{\alpha} = 3.3311$, $\bar{b}_1 = 1.1334$, $\bar{b}_2 = 1.4232$ and $k_s = 0.2942$.

Figure F.1(a) shows a response of the Bouc-Wen model under the single-frequency input in Eq. (F.2). Parameters used were $\alpha_1 = 1$, $\alpha_2 = 0.8$, $\alpha_3 = 0.2$ and $n = 1$. Figure F.1(b) shows a response of the two-state model under the single-frequency input in Eq. (F.2). Parameters of the two-state model are fitted in such a way that the two loops in Figures F.1(a) and (b) match. Parameters used for our two-state model were $\bar{\mu} = 1$, $\sigma = 0.1524$, $\bar{\alpha} = 3.3311$, $\bar{b}_1 = 1.1334$, $\bar{b}_2 = 1.4232$ and $k_s = 0.2942$. Figure F.1(c) shows the match between the Bouc-Wen model and our two-state model.

The energy dissipated per cycle under the single-frequency input for the Bouc-

Wen model is $D = 0.8316$ in some units, and for the two-state model is $D_2 = 0.8257$ in the same units. The relative difference between the dissipated energy per cycle is 0.71%.

Figure F.1(d) shows the response of the Bouc-Wen model under the two-frequency input in Eq. (F.3). Note that the two minor loops are not captured by the Bouc-Wen model. Figure F.1(d) shows the response of the two-state model under the two-frequency input in Eq. (F.3). Minor loops are captured well by the two-state model.

The energy dissipated per cycle under the two-frequency input for the Bouc-Wen model is $D = 1.0637$ in some units, and for the two-state model is $D_2 = 0.9368$ in the same units. The relative difference between the dissipated energy per cycle is 13.54%.

Therefore, in the presence of minor loops, the error can be 20-30 times bigger. Surely, being able to capture the minor loops accurately is academically desirable regardless of quantitative magnitude of relative errors involved.

Appendix G

Fitting of results in Figure 4.5 using the Iwan model

We note that the original Iwan model is a high-dimensional discrete system (as shown in Figure 3.1). One drawback of the Iwan model is that the model is not expressible in terms of a system of differential equations. In the original paper [10], Iwan proposed an analytical form for the output force $f(t)$ for a system driven by a displacement input $u(t)$. The form was later simplified by Segalman [12], and since then several authors have used that particular form, as in

$$f(t) = \int_0^\infty \rho(\phi)[u(t) - \xi(t,\phi)]d\phi, \tag{G.1}$$

where $\rho(\phi)$ is a density distribution function and $\xi(t,\phi)$ is the current displacement of sliders of strength ϕ. Segalman [12] proposed a power law population distribution for $\rho(\phi)$, as in

$$\rho(\phi) = R\,\phi^\chi[H(\phi) - H(\phi - \phi_{\max})] + S\delta(\phi - \phi_{\max}),$$

where $H(\cdot)$ is the Heaviside step function and $\delta(\cdot)$ is the Dirac delta function, and where R, χ, $\phi_{\max}$ and S are fitted parameters.

Subsequent analysis starting from Eq. (G.1) requires storage and utilization of

the entire history of the input, and is simple only in the perfectly periodic case. For this reason, this formulation is difficult to use if input displacements contain many arbitrary minor reversals within it. The advantage of our model reduction in this setting is that we can have complex inputs with many reversals that are solved for incrementally, and the history of the input need not be remembered. In what follows, we use the linear complementarity problem or LCP formulation (as discussed in chapters 2 and 3) to fit the results obtained in Figure 4.5 using an Iwan model. We will compare the fit quality and simulation times of the Iwan model and our two-state model.

For the Iwan model, we take (recall Eq. (3.2))

$$\mu \operatorname{sgn}(\dot{\xi}) + K\xi = bu(t), \tag{G.2}$$

where

$$\mu = \frac{\mu_0}{n}\begin{bmatrix} 1 & 0 & \cdots & 0 \\ 0 & 2 & \cdots & 0 \\ \vdots & \vdots & \ddots & \vdots \\ 0 & 0 & \cdots & n \end{bmatrix}, \; K = \frac{1}{n}\begin{bmatrix} 1 & 0 & \cdots & 0 \\ 0 & 1 & \cdots & 0 \\ \vdots & \vdots & \ddots & \vdots \\ 0 & 0 & \cdots & 1 \end{bmatrix}, \; b = \frac{1}{n}\begin{Bmatrix} 1 \\ 1 \\ \vdots \\ 1 \end{Bmatrix},$$

and where ξ is high-dimensional and $u(t)$ is a displacement input. The system (Eq. (G.2)) has two parameters, μ_0 and n. The hysteretic output of Eq. (G.2) is

$$f(t) = u(t) - \frac{1}{n}\sum_{j=1}^{n} \xi_j. \tag{G.3}$$

We fix n and we fit μ_0. For better fitting, we introduce an *ad hoc* parameter ζ in the output force to account for a nonzero mean value acquired during complex input in a finite window of time.

$$f(t) = u(t) - \frac{1}{n}\sum_{j=1}^{n} \xi_j + \zeta.$$

Note that ζ does not affect the solution of Eq. (G.2).

Figure G.1 shows fitting of the hysteresis loops of case 1 in Figure 4.5 by the Iwan model with $n = 5$, $n = 10$, $n = 20$ and $n = 50$. The corresponding simulation time taken in Matlab in seconds are 0.89 ($n = 5$), 1.15 ($n = 10$), 1.98 ($n = 20$) and 4.11 ($n = 50$) for three cycles of the input history with a time increment of 0.001. In each subplot of Figure G.1, the blue curve is the finite element result (normalized), and the red curve is the fitted curve using the Iwan model. The fit quality improves with increase in the number of elements. Numerical values of the fitted parameters for the cases of Figure G.1 are given in Table G.1.

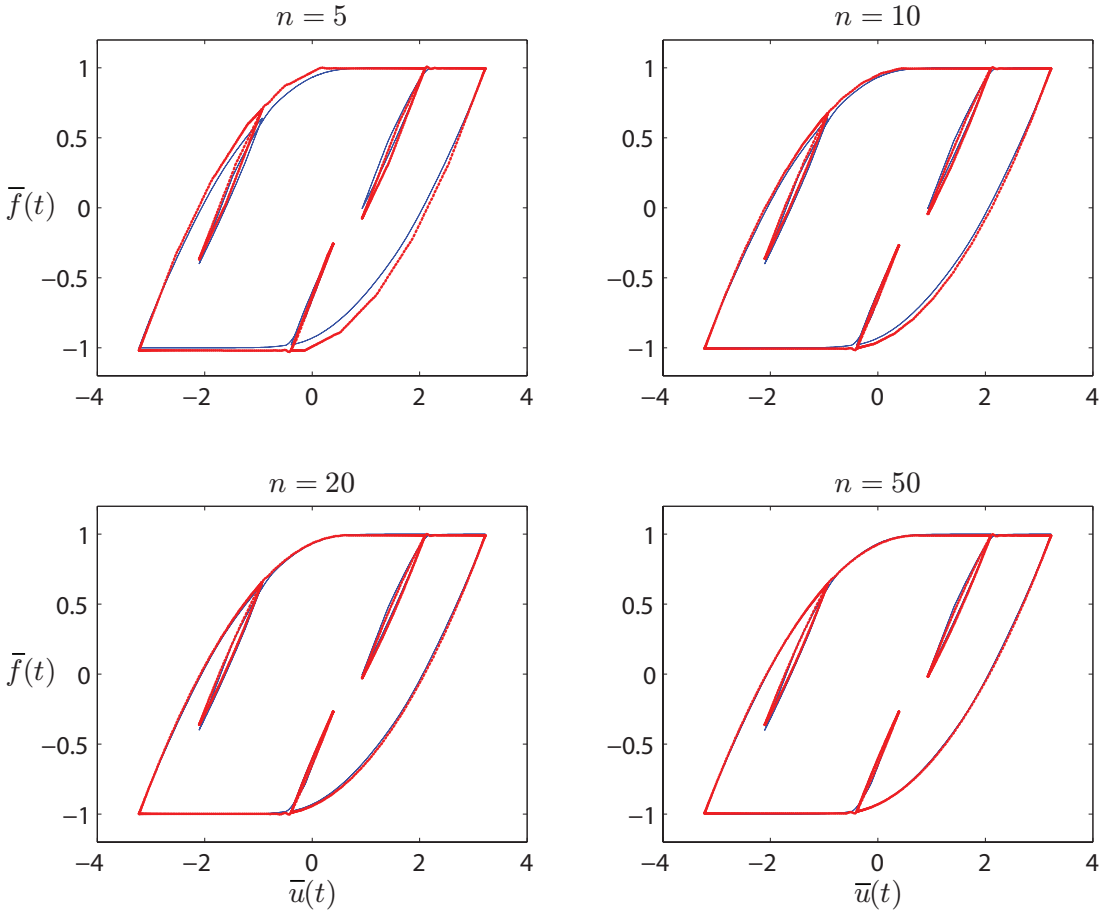

Figure G.1: Fitting of hysteresis loop (the blue curve) of case 1 in Figure 4.5 by the Iwan model with $n = 5$, $n = 10$, $n = 20$ and $n = 50$. The fitted curves using the Iwan model are plotted in red.

Figure G.2 shows fitting of hysteresis loops of cases 1 through 6 in Figure 4.5 by the Iwan model with $n = 20$, and by the two-state model. In each subplot of Figure G.2, the blue solid line is the finite element result (normalized; hidden by the red

Table G.1: Fitted parameters for the cases of Figure G.1.

	$n = 5$	$n = 10$	$n = 20$	$n = 50$
μ_0	0.3362	0.1820	0.0948	0.0389
ζ	−0.2128	−0.1057	−0.0536	−0.0222

solid line), the red solid line with dots is the fitted curve using the Iwan model, and the black dashed line is the fitted curve using the two-state model.

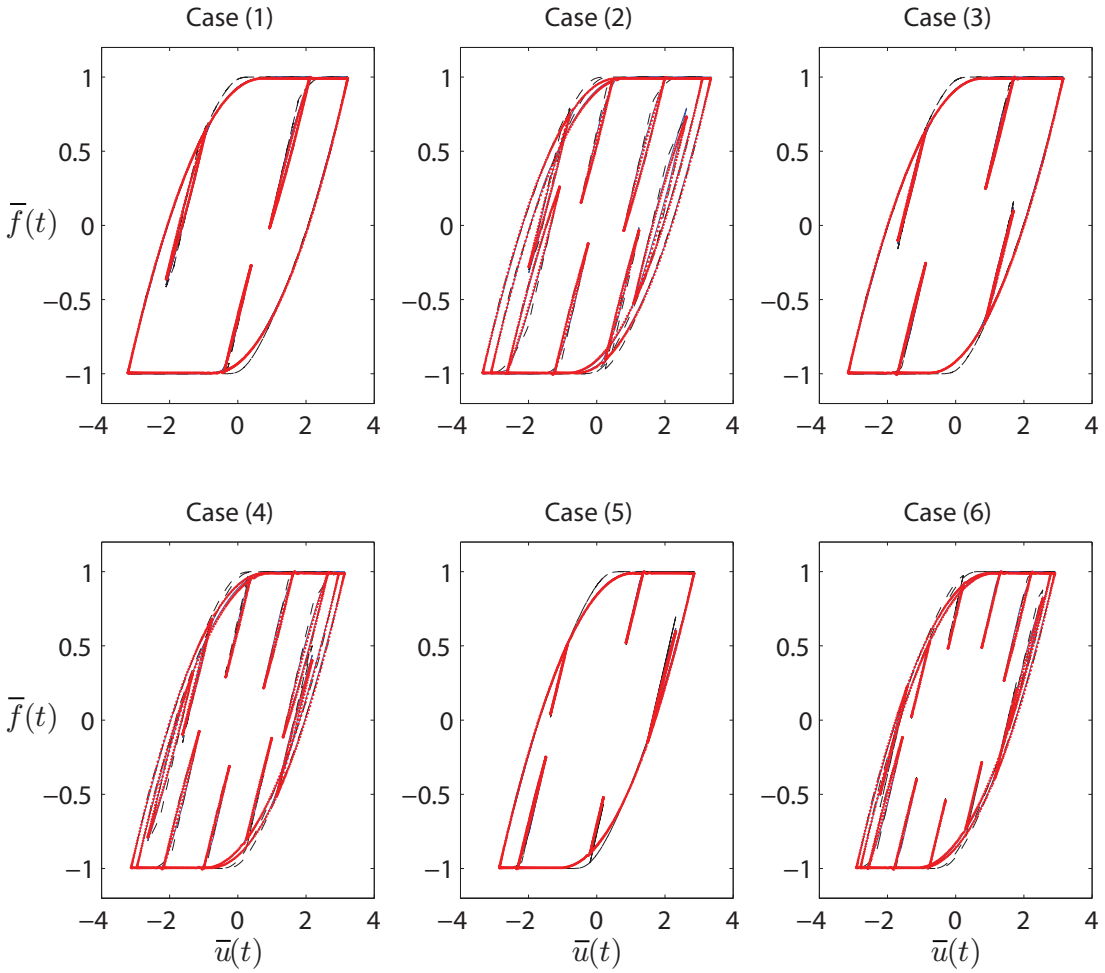

Figure G.2: Fitting of hysteresis loops (the blue solid lines) of cases 1 through 6 in Figure 4.5 by the Iwan model with $n = 20$ (the red solid lines with dots), and by the two-state model (the black dashed lines). Parameters used for the Iwan model: $\mu_0 = 0.0948$ and $\zeta = -0.0536$.

Note in Figure G.2 that the quality of fitting by the Iwan model with $n = 20$ is superior to the quality of fitting by the two-state model. However, using more states in our reduced-order model, a better fit is achievable (details not presented

here).

In Table G.2, we show simulation time in seconds for the cases of Table 4.1 using the Iwan model with $n = 20$, and using the two-state model solved by Matlab's `ode45` with numerical tolerance set at 10^{-5} as well as using the incremental map resembling the LCP formulation discussed in chapter 3. For each case, we simulated 100 cycles of the input; and for the LCP and incremental maps we used a time increment of 0.001. The Iwan model with the LCP solver is about 10-15% faster than `ode45`, but 5 times smaller than the incremental map with two states.

Table G.2: Simulation time in seconds for the cases of Table 4.1.

	Case 1	Case 2	Case 3	Case 4	Case 5	Case 6
Iwan model (LCP) ($n = 20$)	60.61	61.23	59.83	60.09	56.85	56.56
Two-state model (ODE) (tol. 10^{-5})	69.62	69.89	69.93	70.01	60.22	60.79
Two-state model (incremental map)	11.61	11.86	11.88	11.89	11.53	11.56

In summary, when comparable incremental algorithms are used for both calculations, the Iwan model is about 5 times slower than our two-state model.

Appendix H

Computational data: hysteresis in two single-bolted joints

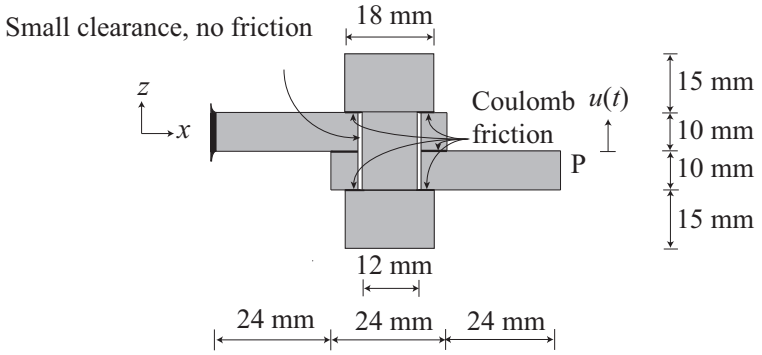

(a)

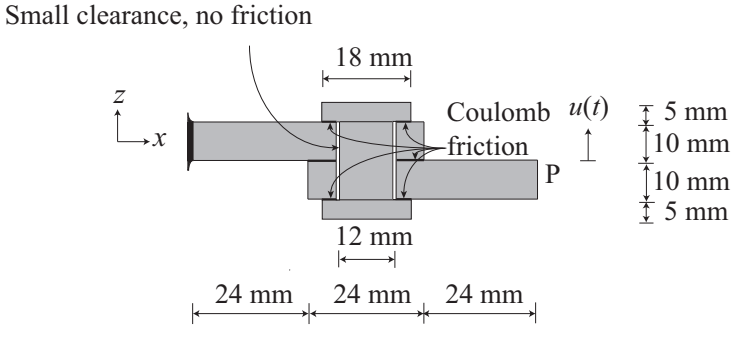

(b)

Figure H.1: Two other geometries. Compare with Figure 4.1.

For completeness, we present computational results for two other single-bolted lap joints: see Figures H.1(a) and H.1(b). These models differ from the model in Figure 4.1 in their dimensions only. For both these new models, we assigned the same material properties, boundary conditions, and frictional contact conditions as in Figure 4.1.

Table H.1: Two-frequency displacement inputs, friction coefficients μ, and bolt preloads (PL) considered for the finite element simulation for the model in Figure H.1(a).

Case	μ	PL (kN)	$u(t)$ (mm)
1	0.10	30	$2\sin 2\pi t + \sin 8\pi t$
2	0.10	30	$2\sin 2\pi t + \sin 9\pi t$
3	0.10	30	$2\sin 2\pi t + 0.8\ \sin 10\pi t$
4	0.10	30	$2\sin 2\pi t + 0.8\ \sin 11\pi t$
5	0.10	30	$2\sin 2\pi t + 0.6\ \sin 12\pi t$
6	0.10	30	$2\sin 2\pi t + 0.6\ \sin 13\pi t$

Table H.2: Two-frequency displacement inputs, friction coefficient μ, and bolt preload (PL) considered for the finite element simulation for the model in Figure H.1(b).

Case	μ	PL (kN)	$u(t)$
1	0.20	20	$2\sin 2\pi t + \sin 8\pi t$
2	0.20	20	$2\sin 2\pi t + \sin 9\pi t$
3	0.20	20	$2\sin 2\pi t + 0.8\ \sin 10\pi t$
4	0.20	20	$2\sin 2\pi t + 0.8\ \sin 11\pi t$
5	0.20	20	$2\sin 2\pi t + 0.6\ \sin 12\pi t$
6	0.20	20	$2\sin 2\pi t + 0.6\ \sin 13\pi t$

52614 and 42186 elements respectively (ABAQUS C3D8R) were used for Figures H.1(a) and H.1(b). Tables H.1 and H.2 show various inputs used for simulations. Figures H.2 and H.3 show the normalized hysteresis loops obtained, and are seen to be qualitatively similar to Figures 4.5 and 4.6. Fitting results from the two-state model are shown in Figures H.4 and H.5 respectively, and are seen to be excellent.

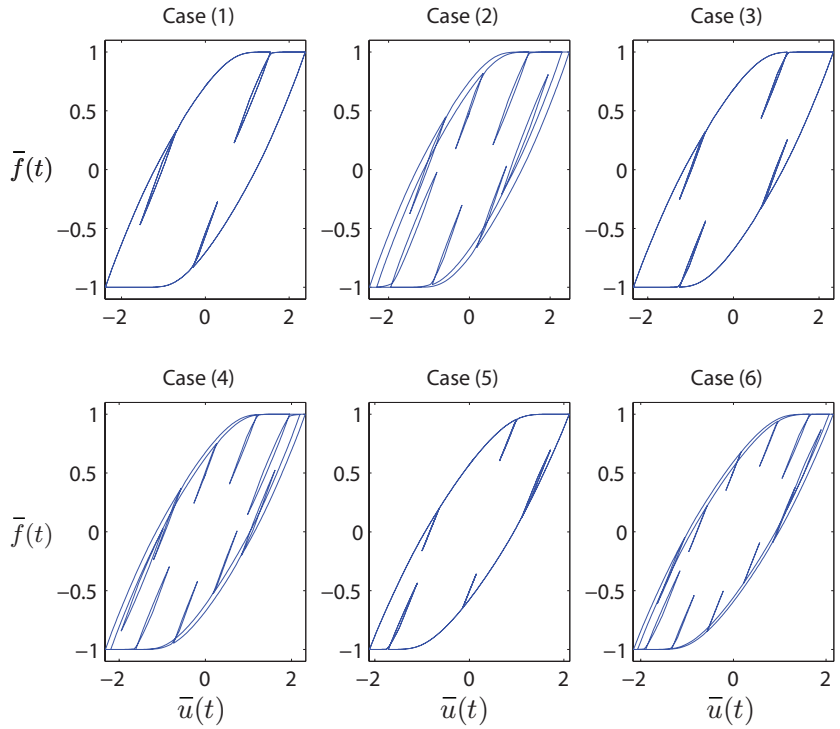

Figure H.2: Hysteresis loops obtained for the cases considered in Table H.1. $a_0 = 5.8188$, $a_1 = 14.8891$ and $a_2 = 0.8335$ for all six cases.

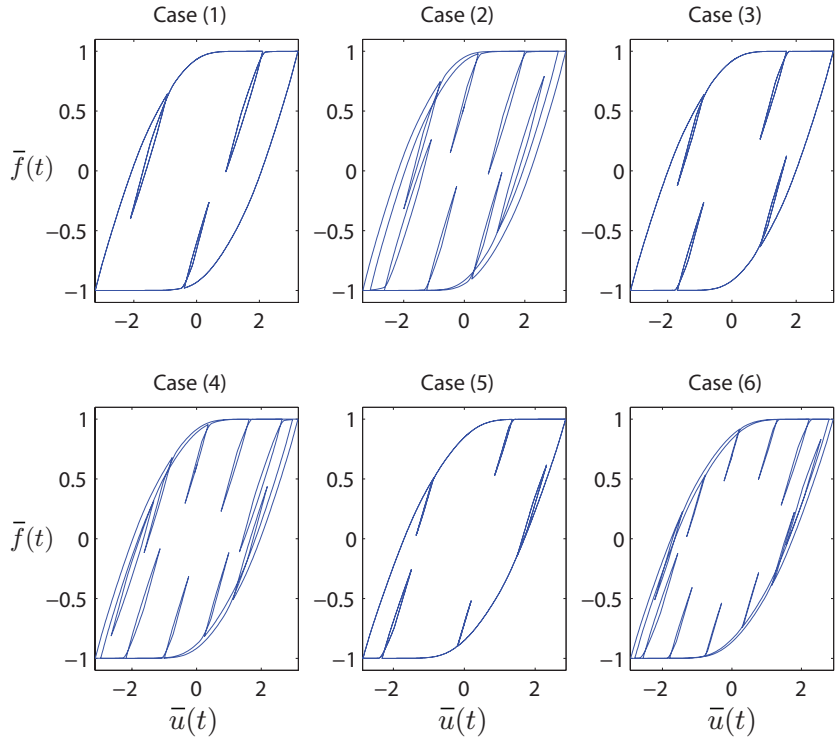

Figure H.3: Hysteresis loops obtained for the cases considered in Table H.2. $a_0 = 14.5346$, $a_1 = 34.9184$ and $a_2 = 1.1280$ for all six cases.

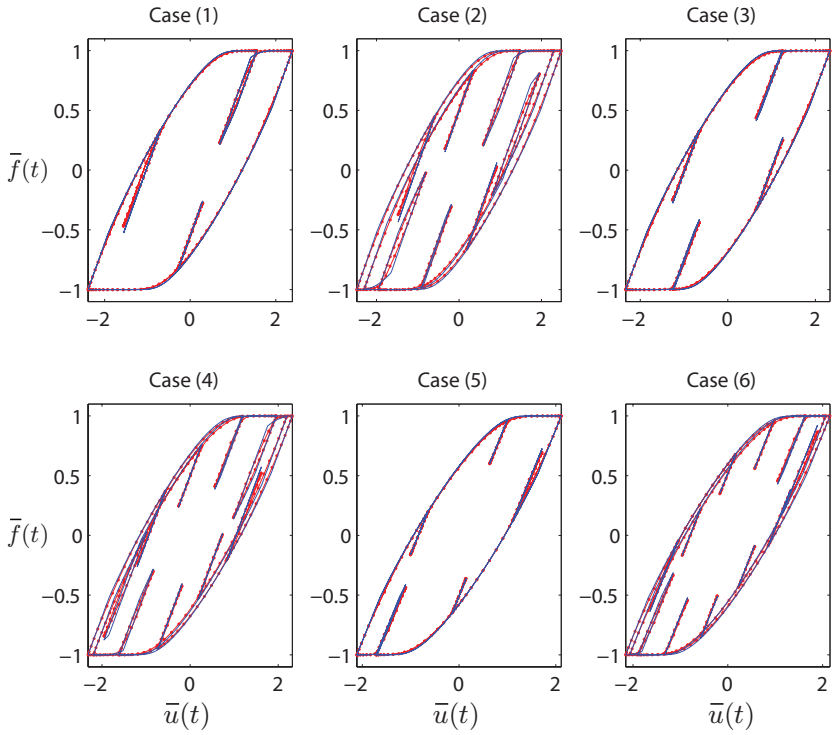

Figure H.4: Fitting loops of Figure H.2, with parameters given in Eq. (4.20). The blue solid lines: fitted hysteresis loops from the two-state model. Red solid lines with dots: FE results.

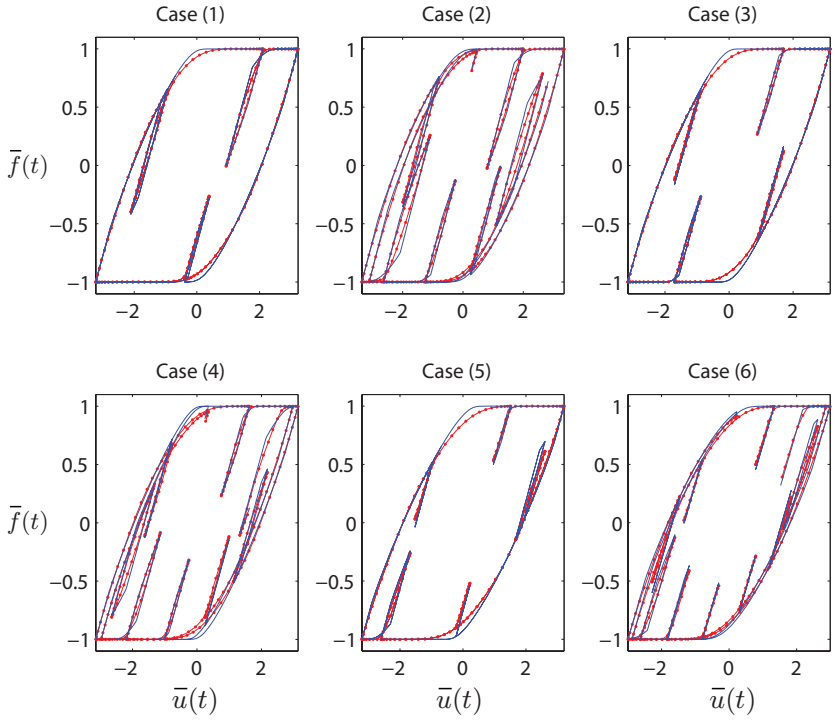

Figure H.5: Fitting loops of Figure H.3, with parameters given in Eq. (4.20). The blue solid lines: fitted hysteresis loops from the two-state model. Red solid lines with dots: FE results.

Appendix I

Derivation of c_s

Here we derive the expression for c_s in Eq. (4.11).

Recall Eq. (4.5), and consider that when $|u|$ is large enough, c saturates to one of two constant vectors. Let

$$\pm c_s = \bar{\alpha} q - \bar{b} u. \tag{I.1}$$

From Eq. (I.1), provided $\dot{u}$ does not change sign,

$$\dot{q} = \frac{\dot{u}}{\bar{\alpha}} \bar{b}, \tag{I.2}$$

where q and $\bar{b}$ are vectors, and u and $\bar{\alpha}$ are scalars. Thus, the slip direction

$$\eta \to \frac{\bar{b}}{\|\bar{b}\|} = \hat{b}$$

with the hat denoting a unit vector, as $c \to \pm c_s$. In the same saturated regime, from Eq. (4.6),

$$\sqrt{\eta^T A \eta} + \eta^T c_s = 0 \tag{I.3}$$

because slip is steadily occurring. It remains to find c_s. From Eq. (3.9), with $c = c_s$,

$$\frac{A\eta}{\sqrt{\eta^T A \eta}} + c_s - \lambda \eta = 0. \tag{I.4}$$

Premultiplying both sides of Eq. (I.4) with η^T gives

$$\sqrt{\eta^T A \eta} + \eta^T c_s - \lambda = 0. \tag{I.5}$$

From Eqs. (I.3) and (I.5), $\lambda = 0$. From Eq. (I.4),

$$c_s = -\frac{A\hat{b}}{\sqrt{\hat{b}^T A \hat{b}}} = -\frac{A\bar{b}}{\sqrt{\bar{b}^T A \bar{b}}}. \tag{I.6}$$

Appendix J

Hysteresis in a double-bolted joint

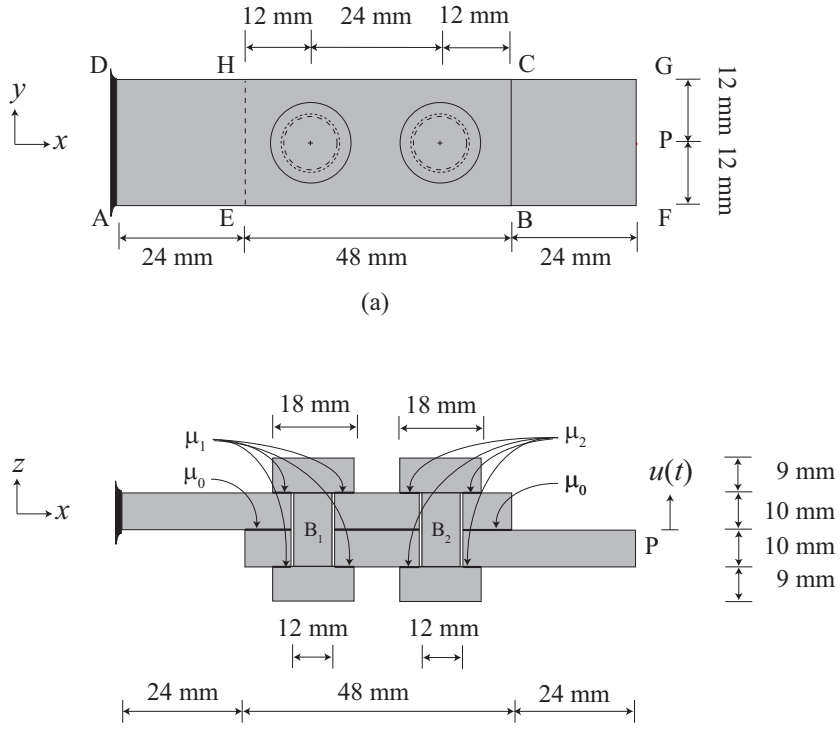

Figure J.1: A lap joint connecting two plates by two bolts B_1 and B_2. (a) Top view. (b) Mid-sectional side view. The left end is clamped, and the the right end is free. We apply transverse displacement inputs $u(t)$ at point P. The radial clearances between the bolt shanks and plate holes are 0.6 mm.

We consider a joint with two bolts B_1 and B_2 as sketched in Figure J.1. The material properties assigned were $E = 210$ GPa and $\nu = 0.3$.

Frictional contact with possible separation is defined between the two plates. The friction coefficient between the two plates is μ_0; that between the bolt B_1 and plates is μ_1; and that between the bolt B_2 and plates is μ_2, as indicated in Figure J.1. PL_1 and PL_2 are bolt preloads assigned to B_1 and B_2 respectively.

The finite elements mesh used had 90264 elements (ABAQUS C3D8R). Table J.1 shows the friction coefficients, bolt preloads and displacement inputs used in the FE simulations.

Table J.1: Two-frequency displacement inputs, friction coefficients μ_0, μ_1 and μ_2, and bolt preloads PL_1 and PL_2 considered for the finite element simulation for the model in Figure J.1.

Case	μ_0	μ_1	μ_2	PL_1 (kN)	PL_2 (kN)	$u(t)$ (mm)
1	0.10	0.10	0.10	20	20	$2\sin 2\pi t + \sin 8\pi t$
2	0.20	0.20	0.20	40	40	$2\sin 2\pi t + 0.6\ \sin 12\pi t$
3	0.15	0.15	0.15	40	20	$2\sin 2\pi t + \sin 8\pi t$
4	0.15	0.10	0.20	20	40	$2\sin 2\pi t + 0.6\ \sin 12\pi t$
5	0.15	0.20	0.10	40	20	$2\sin 2\pi t + \sin 8\pi t$
6	0.15	0.20	0.10	20	40	$2\sin 2\pi t + 0.6\ \sin 12\pi t$

Since the bolt preloads and friction coefficients differ, the normalizing parameters a_0, a_1 and a_2 differ for each load case. These parameters are reported in Table J.2.

Table J.2: a_0, a_1 and a_2 calculated for loading cases in Table J.1.

Case	a_0	a_1	a_2
1	3.3689	4.0765	0.7565
2	5.0186	6.9464	1.0560
3	4.5717	6.0402	1.1333
4	6.4280	8.4465	1.1111
5	4.2293	5.5430	1.1224
6	4.1501	5.4446	1.1429

The normalized hysteresis loops along with the fits obtained from the two-state model are shown in Figure J.2; corresponding numerical values of fitted parameters are given in Table J.3. In Table J.3, $\bar{\alpha}$ and σ are free parameters, while $\bar{b}_1$ and $\bar{b}_2$ for

each case satisfy Eqs. (4.18) and (4.19) for the corresponding $\bar{\alpha}$ and σ. An excellent fit is obtained in every case.

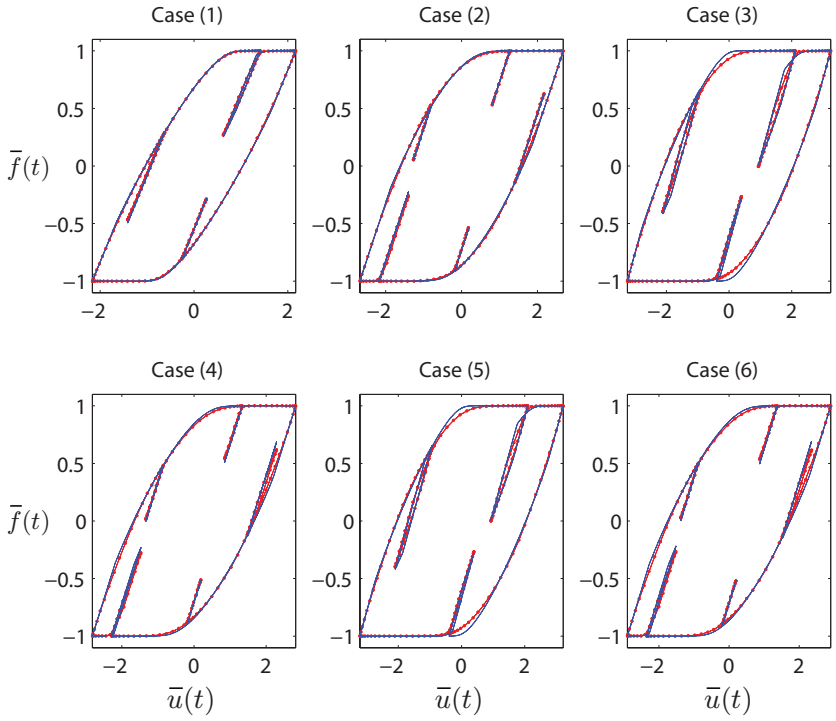

Figure J.2: Hysteresis loops: FE results, and two-state model with parameters as given in Table J.3. Solid lines represent fitted hysteresis loops, and solid lines with dots denote FE results.

Table J.3: Fitted parameters for the cases of Figure J.2. Unlike the single-bolt case, these fitted parameters vary with joint details.

Case	$\bar{\alpha}$	σ
1	0.7223	0.0627
2	0.6818	0.1206
3	0.6554	0.0587
4	0.6267	0.0898
5	0.6584	0.0597
6	0.6223	0.0872

Appendix K

Hysteresis loops for constant μ

In Figures 6.4 and 6.5, we presented results for randomly generated friction coefficients μ between 0 to 1, varying from crack to crack within the same simulation. Here, we consider the same μ on all crack faces. We consider $\mu = 0.1$ and $\mu = 0.2$, for both Model 1 and Model 2. Figures K.1 and K.2 show results for Model 1 and Model 2 respectively. In these figures, blue solid curves and red dotted curves represent $\mu = 0.1$ and $\mu = 0.2$ respectively. The hysteresis loops are magnified using the same method as in section 6.2.2 (recall Eq. 6.3), except that within each subplot, the a and b values are the same (numerical details omitted). It is seen that the hysteresis loops obtained are qualitatively similar. The $\mu = 0.2$ loops are fatter than the ones for $\mu = 0.1$, but not exactly in proportion with μ (not surprising because the frictional contact problem with interacting cracks is strongly nonlinear).

It remains to comment on hysteresis loops obtained with very high friction values (such as 2, 5 or 10). Analytically, we expect the rising branch (starting from zero) of each hysteresis loop to be a straight line, as was observed for both the variable μ cases in Figures 6.4 and 6.5 as well as for $\mu = 0.1$ and 0.2 in Figures K.1 and K.2. However, these hysteresis loops are actually very small deviations from purely linear behavior, and are computationally obtained when the dominant behavior is subtracted and fine details of remaining behavior are observed closely. With this background, we report that for high values of μ, the rising branch we obtained was not straight. This may be due to numerical difficulties due to the high friction

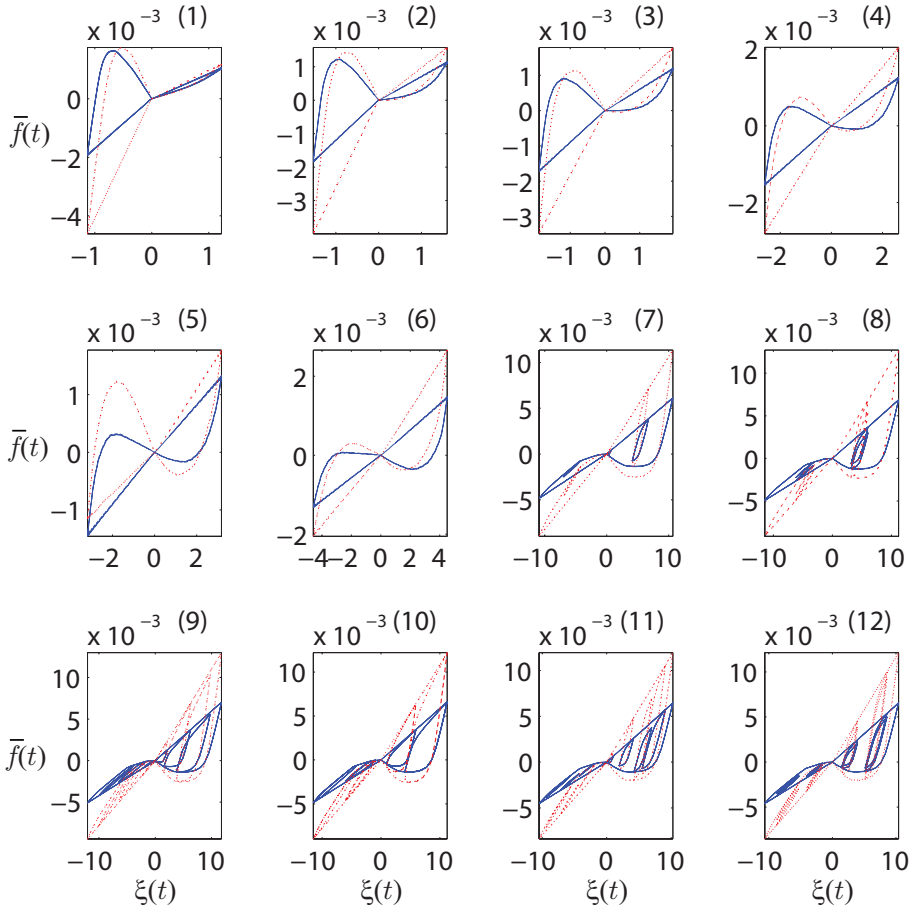

Figure K.1: Hysteresis loops obtained from Model 1 for the twelve load cases considered in Table 6.1. Blue solid curves and red dotted curves are obtained using $\mu = 0.1$ and $\mu = 0.2$ respectively at all crack interfaces. Within each subplot, the same a and b are used to enable meaningful comparison (see Eq. 6.3).

(which might be addressed using super-fine meshes in future work) or possibly due to complex contact physics that we do not understand at this time. Accordingly, we refrain from commenting on high-μ behavior in this work and leave it to future work.

We reemphasize that our main interest lies in the shapes of the hysteresis loops already obtained, and those results are clear for small μ; and our main contribution is expected to be in the area of vibration damping, where the scalar model of Eq. 6.5 provides a great improvement over simple viscous damping models or the even simpler modal damping ratios that are commonly used by analysts and designers.

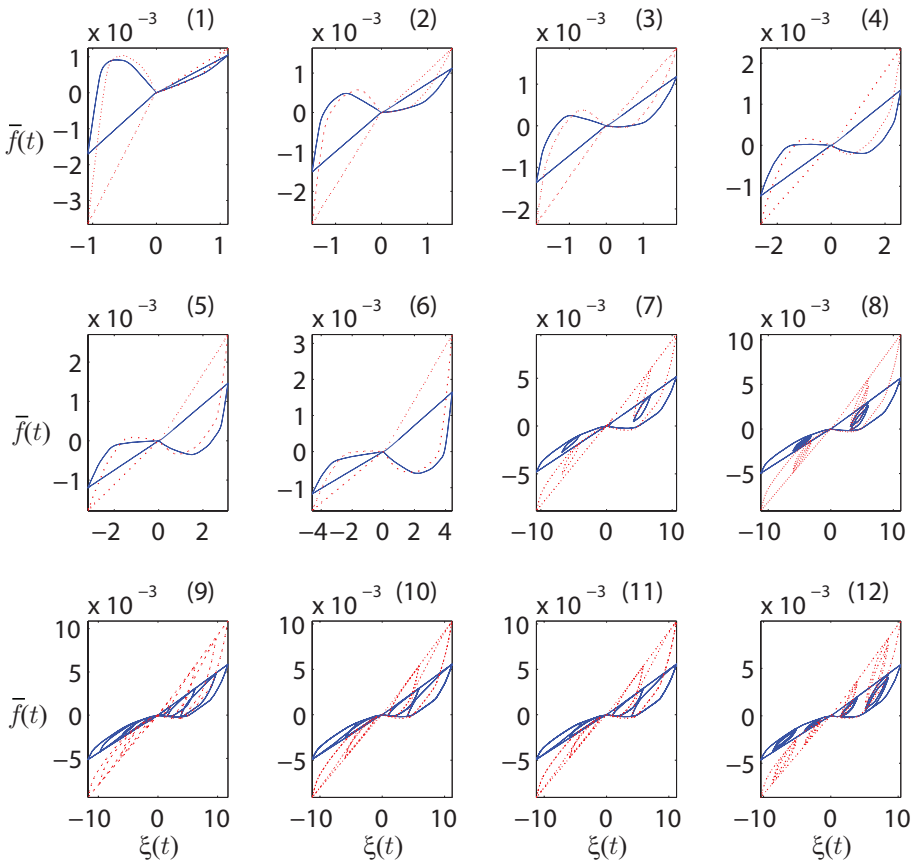

Figure K.2: Hysteresis loops obtained from Model 2 for the twelve load cases considered in Table 6.1. Blue solid curves and red dotted curves are obtained using $\mu = 0.1$ and $\mu = 0.2$ respectively at all crack interfaces. Within each subplot, the same a and b are used to enable meaningful comparison (see Eq. 6.3).

Appendix L

Correlation between two models 1 and 2

An anonymous reviewer of [58] suggested that a comparison between the results of the two models (the two sets of cracks) for various load cases should be presented, so that an assessment may be made of how many such geometries, or alternatively how big a number of random cracks, needs to be used to obtain meaningful averaged results. To this end, for each of the twelve load cases of Table 6.1, the dissipation per cycle for Model 2 is plotted against that for Model 1 in Figure L.1. If there were very

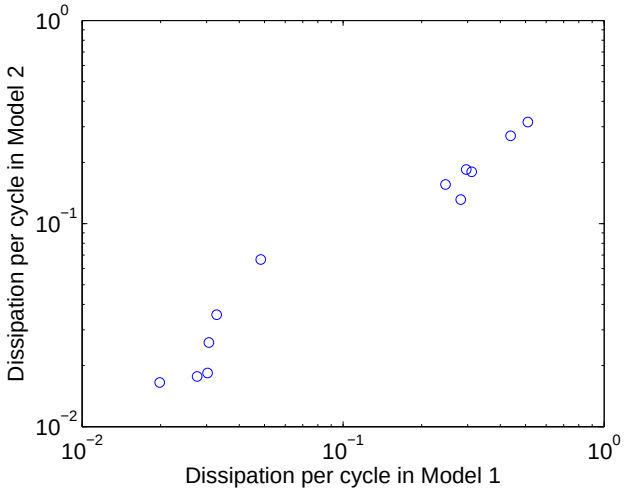

Figure L.1: Dissipation per cycle in Model 1 and Model 2 plotted on logarithmic axes. Each data point corresponds to the same load case but two geometries (two finite element models).

many cracks so that the true population average behavior could be estimated, the plotted points would lie on a 45 degree line. Here, they do not; however, they are not very far from such a line. As an engineering approximation, we may say that if the deviation could be reduced by a factor of about 10, then the plot would be sufficiently close to a straight line for most practical purposes. Given that statistical estimates of parameters typically converge like $n^{-1/2}$ where n is the number of data points, we estimate that about 100 such sets of simulations (i.e., 100 models like Model 1 and Model 2) would be needed to see the underlying straight line clearly. Alternatively, perhaps a single model with 100 times as many cracks, i.e., with about 3200 cracks, might give an excellent idea of the average homogenized behavior through a single set of simulations.

We emphasize again, however, that our main interest here lies in obtaining a suitable simple form of hysteretic damping for use in structural vibrations, and so our interest in Figure 6.8 of the main chapter is greatest.

Appendix M

Fitted parameters for Figure 6.8

The fitted parameters used for Figure 6.8 are given in Table M.1.

Table M.1: Fitted parameters K_0, θ_m, $\tilde{\beta}$ used in Figure 6.8. Note: $\epsilon = 10^{-4}$ in all cases.

Case	K_0	θ_m	$\tilde{\beta}$
1	0.8091	3.9400×10^{-4}	4.8670×10^{-4}
2	0.9094	1.2323×10^{-4}	8.7557×10^{-4}
3	0.4543	7.110×10^{-4}	0.0014
4	0.6600	3.2359×10^{-4}	7.9801×10^{-4}
5	1.8723	2.7797×10^{-6}	4.1697×10^{-4}
6	4.7454	1.0211×10^{-7}	3.8258×10^{-4}
7	4.3396	9.6901×10^{-5}	4.2733×10^{-4}
8	3.4291	1.1566×10^{-4}	4.8399×10^{-4}
9	3.9350	1.0398×10^{-4}	4.4147×10^{-4}
10	4.1819	1.1658×10^{-4}	4.6170×10^{-4}
11	4.3097	3.6350×10^{-5}	4.4812×10^{-4}
12	4.3257	4.4764×10^{-5}	4.5683×10^{-4}

Bibliography

[1] G. Bertotti and I. Mayergoyz, eds. The science of hysteresis, vols. I-III, Elsevier Academic Press, New York, 2006.

[2] J. A. Ewing, "Experimental researches in magnetism", *Philosophical Transactions of the Royal Society of London*, 1885, v. 176, pp. 523-640.

[3] F. E. Rowett, "Elastic hysteresis in steel", *Proceedings of the Royal Society of London A*, 1914, v. 89, n. 614, pp. 528-543.

[4] F. Preisach, "Über die magnetische nachwirkung", *Zeitschrift für Physik*, 1935, v. 94, pp. 277-302.

[5] Lord Kelvin (W. Thomson), "On the elasticity and viscosity of metals", *Proceedings of the Royal Society of London A*, 1865, v. 14, pp. 289-297.

[6] A. L. Kimball and D. E. Lovell, "Internal friction in solids", *Physical Review*, 1927, v. 30, pp. 948-959.

[7] R. Bouc, "Forced vibrations of mechanical systems with hysteresis", Proceedings of the Fourth Conference on Nonlinear Oscillation, Prague, Czechoslovakia, 1967, pp. 315.

[8] Y. K. Wen, "Method for random vibration of hysteretic systems", *Journal of the Engineering Mechanics Division, ASCE*, 1976, v. 102, n. 2, pp. 249-263.

[9] F. Ikhouane and J. Rodellar, Systems with Hysteresis: Analysis, Identification and Control using the Bouc-Wen Model, John Wiley & Sons, Ltd, New York, 2007.

[10] W. D. Iwan, "A distributed-element model for hysteresis and its steady-state dynamic response", *Journal of Applied Mechanics, ASME*, 1966, v. 33, n. 4, pp. 893-900.

[11] W. D. Iwan, "On a class of models for the yielding behavior of continuous and composite systems", *Journal of Applied Mechanics, ASME*, 1967, v. 34, n. 3, pp. 612-617.

[12] D. J. Segalman, "A four-parameter Iwan model for lap-type joints", *Journal of Applied Mechanics, ASME*, 2005, v. 72, n. 5, pp. 752-760.

[13] M. W. R. Brake, "A reduced Iwan model that includes pinning for bolted joint mechanics", *Nonlinear Dynamics*, 2017, v. 87, n. 2, pp. 1335-1349.

[14] B. J. Lazan, Damping of materials and members in structural mechanics, Pergamon Press Ltd., Oxford, 1968.

[15] T. J. Reid, "Free vibration and hysteretic damping", *Journal of the Royal Aeronautical Society*, 1956, v. 60, pp. 283.

[16] S. Biswas and A. Chatterjee, "A reduced-order model from high-dimensional frictional hysteresis", *Proceedings of the Royal Society A*, 2014, v. 470, 20130817.

[17] A. Bhattacharjee and A. Chatterjee, "Dissipation in the Bouc-Wen model: small amplitude, large amplitude and two-frequency forcing", *Journal of Sound and Vibration*, 2013, v. 332, n. 7, pp. 1807-1819.

[18] P. Jana and A. Chatterjee, "Modal damping in vibrating objects via dissipation from dispersed frictional microcracks", *Proceedings of the Royal Society A*, 2013, v. 469, 20120685.

[19] F. Ikhouane, V. Manosa and J. Rodellar, "Dynamic properties of the hysteretic Bouc-Wen model", *Systems and Control Letters*, 2007, v. 56, pp. 197-205.

[20] S. Erlicher and N. Point, "Thermodynamic admissibility of Bouc-Wen type hysteresis models", *C. R. Mecanique*, 2004, v. 332, n. 1, pp. 51-57.

[21] A. E. Charalampakis and V. K. Koumousis, "A Bouc-Wen model compatible with plasticity postulates", *Journal of Sound and Vibration*, 2009, v. 322, pp. 954-968.

[22] C. Canudas de Wit, H. Olsson, K. J. Åström and P. Lischinsky, "A new model for control of systems with friction", *IEEE Trransactions on Automatic Control*, 1995, v. 40, n. 3, pp. 419-425.

[23] H. Dankowicz and A. B. Nordmark, "On the origin and bifurcations of stick-slip oscillations", *Physica D*, 2000, v. 136, pp. 280-302.

[24] E. Barbisio, F. Fiorillo and C. Ragusa, "Predicting loss in magnetic steels under arbitrary induction waveform and with minor hysteresis loops", *IEEE Transactions on magnetics*, 2004 v. 40, n. 4, pp. 1810-1819.

[25] R. W. Cottle, J. S. Pang and R. E. Stone, The Linear Complementarity Problem, Academic Press, NY, 1992.

[26] M. J. Miranda and P. L. Fackler, Applied Computational Economics and Finance, MIT Press, 2002. "CompEcon Toolbox" accompanies the text: see http://www4.ncsu.edu/ pfackler/compecon/.

[27] R. W. Ogden, Non-linear elastic deformations, Courier Corporation, 1997.

[28] K. Hackl and F. D. Fischer, "On the relation between the principle of maximum dissipation and inelastic evolution given by dissipation potentials", *Proceedings of the Royal Society A*, 2008, v. 464, pp. 117-132.

[29] A. Chatterjee, "An introduction to the proper orthogonal decomposition", *Current Science*, 2000, v. 78, n. 7, pp. 808-817.

[30] L. Meirovitch, Fundamentals of Vibrations, Waveland Press, Illinois, 2010.

[31] J.-S. Pang and J. C. Trinkle, "Complementarity formulations and existence of solutions of dynamic multi-rigid-body contact problems with Coulomb friction", *Mathematical Programming*, 1996, v. 73, pp. 199-226.

[32] S. Biswas and A. Chatterjee, "A two-state hysteresis model from high dimensional friction", *Royal Society Open Science*, 2015, v. 2, 150188.

[33] D. C. Jiles and D. L. Atherton, "Theory of ferromagnetic hysteresis", *Journal of Magnetism and Magnetic Materials*, 1986, v. 61, n. (1-2), pp. 48-60.

[34] A. Klarbring and J.-S. Pang, "Existence of solutions to discrete semicoercive frictional contact problems". *SIAM Journal on Optimization*, 1998, v. 8, n. 2, pp. 414-442.

[35] D. Scerrato, I. Giorgio, A. Madeo, A. Limam and F. Darve, "A simple nonlinear model for internal friction in modified concrete", *International Journal of Engineering Science*, 2014, v. 80, pp. 136-152.

[36] D. Scerrato, I. Giorgio, A. Della Corte, A. Madeo and A. Limam, "A microstructural model for dissipation phenomena in the concrete", *International Journal for Numerical and Analytical methods in Geomechanics*, 2015, v. 39, n. 18, pp. 2037-2052.

[37] D. A. Harville, Matrix Algebra from a Statistician's Perspective, Vol. 157. NY: Springer, 1997.

[38] L. E. Goodman and C. B. Brown, "Energy dissipation in contact friction: constant normal and cyclic tangential loading", *Journal of Applied Mechanics, ASME*, 1962, v. 29, n. 1, pp. 17-22.

[39] M. Groper, "Microslip and macroslip in bolted joints", *Experimental Mechanics*, 1985, v. 25, n. 2, pp. 171-174.

[40] R. A. Ibrahim and C. L. Pettit, "Uncertainties and dynamic problems of bolted joints and other fasteners", *Journal of Sound and Vibration*, 2005, v. 279, n. 3, pp. 857-936.

[41] E. E. Ungar, Energy dissipation at structural joints: mechanisms and magnitudes, Technical Documentary Report No. FDL-TDR-64-98, Air Force Flight Dynamics Lab, Wright-Patterson Air Force Base, OH, 1964.

[42] S. W. E. Earles, "Theoretical estimation of the frictional energy dissipation in a simple lap joint", *Journal of Mechanical Engineering Science*, 1966, v. 8, n. 2, pp. 207-214.

[43] A. F. Metherell and S. V. Diller, "Instantaneous energy dissipation rate in a lap joint-uniform clamping pressure", *Journal of Applied Mechanics, ASME*, 1968, v. 35, n. 1, pp. 123-128.

[44] C. F. Beards, "Damping in structural joints", *The Shock and Vibration Digest*, 1992, v. 24, n. 7, pp. 3-7.

[45] L. Gaul and J. Lenz, "Nonlinear dynamics of structures assembled by bolted joints", *Acta Mechanica*, 1997, v. 125, n. 1-4, pp. 169-181.

[46] K. C. Valanis, Fundamental consequences of a new intrinsic time measure. Plasticity as a limit of the endochronic theory, No. G-224/DME-78-01. Iowa Univ. Iowa city, 1978.

[47] W. Chen and X. Deng, "Structural damping caused by micro-slip along frictional interfaces", *International Journal of Mechanical Sciences*, 2005, v. 47, n. 8, pp. 1191-1211.

[48] Y. Song, C. J. Hartwigsen, D. M. McFarland, A. F. Vakakis and L. A. Bergman, "Simulation of dynamics of beam structures with bolted joints using adjusted Iwan beam elements", *Journal of Sound and Vibration*, 2004, v. 273, n. 1, pp. 249-276.

[49] M. Oldfield, H. Ouyang and J. E. Mottershead, "Simplified models of bolted joints under harmonic loading", *Computers & Structures*, 2005, v. 84, n. 1, pp. 25-33.

[50] D. D. Quinn and D. J. Segalman, "Using series-series Iwan-type models for understanding joint dynamics", *Journal of Applied Mechanics, ASME*, 2005, v. 72, n. 5, pp. 666-673.

[51] E. Cigeroglu, W. Lu and C. H. Menq, "One-dimensional dynamic microslip friction model", *Journal of Sound and Vibration*, 2006, v. 292, n. 3, pp. 881-898.

[52] H. Ouyang, M. J. Oldfield and J. E. Mottershead, "Experimental and theoretical studies of a bolted joint excited by a torsional dynamic load", *International Journal of Mechanical Sciences*, 2006, v. 48, n. 12, pp. 1447-1455.

[53] H. Ahmadian, H. Jalali and F. Pourahmadian, "Nonlinear model identification of a frictional contact support", *Mechanical Systems and Signal Processing*, 2010, v. 24, n. 8, pp. 2844-2854.

[54] D. D. Quinn, "Modal analysis of jointed structures", *Journal of Sound and Vibration*, 2012, v. 331, n. 1, pp. 81-93.

[55] M. Rajaei and H. Ahmadian, "Development of generalized Iwan model to simulate frictional contacts with variable normal loads", *Applied Mathematical Modelling*, 2014, v. 38, n. 15, pp. 4006-4018.

[56] J. Montgomery, "Methods for modeling bolts in the bolted joint", ANSYS User's Conference, April 2002.

[57] J. Kim, J. C. Yoon and B. S. Kang, "Finite element analysis and modeling of structure with bolted joints", *Applied Mathematical Modelling*, 2007, v. 31, n. 5, pp. 895-911.

[58] S. Biswas, P. Jana and A. Chatterjee, "Hysteretic damping in an elastic body with frictional microcracks", *International Journal of Mechanical Sciences*, 2016, v. 108-109, pp. 61-71.

[59] G. B. Muravskii, "On frequency independent damping", *Journal of Sound and Vibration*, 2004, v. 274, pp. 653-668.

[60] S. Patsias, G. R. Tomlinson and A. M. Jones, "Initial studies into hard coatings for fan blade damping", Proceedings of the 6th National Turbine Engine High Cycle Fatigue (HCF) Conference, Jacksonville, Florida, USA, March, 2001.

[61] T. Lauwagie, K. Lambrinou, S. Patsias, W. Heylen and J. Vleugels, "Resonant-based identification of the elastic properties of layered materials: application to air-plasma sprayed thermal barrier coatings", *NDT & E International*, 2008, v. 41, n. 2, pp. 88-97.

[62] R. K. Abu Al-Rub and A. N. Palazotto, "Micromechanical theoretical and computational modeling of energy dissipation due to nonlinear vibration of hard ceramic coatings with microstructural recursive faults", *International Journal of Solids and Structures*, 2010, v. 47, n. 16, pp. 2131-2142.

[63] Y. H. Jang and J. R. Barber, "Frictional energy dissipation in materials containing cracks", *Journal of the Mechanics and Physics of Solids*, 2011, v. 59, pp. 583-594.

[64] Y. H. Jang and J. R. Barber, "Effect of phase on the frictional dissipation in systems subjected to harmonically varying loads", *European Journal of Mechanics A/Solids*, 2011, v. 30, pp. 269-274.

[65] J. R. Barber, M. Davies and D. A. Hills, "Frictional elastic contact with periodic loading", *International Journal of Solids and Structures*, 2011, v. 48, pp. 2041-2047.

[66] C. Putignano, M. Ciavarella and J. R. Barber, "Frictional energy dissipation in contact of nominally flat rough surfaces under harmonically varying loads", *Journal of the Mechanics and Physics of Solids*, 2011, v. 59, pp. 2442-2454.

[67] M. Kachanov, "Elastic solids with many cracks: A simple method of analysis", *International Journal of Solids and Structures*, 1987, v. 23, pp. 23-43.

[68] A. Carpinteri and A. Spagnoli, "A fractal analysis of size effect on fatigue crack growth", *International Journal of Fatigue*, 2004, v. 26, pp. 125-133.

[69] P. Davis and P. Rabinowitz, Methods of Numerical Integration, Academic Press, Orlando, FL, 1984.

[70] C. Spitas, "A continuous piecewise internal friction model of hysteresis for use in dynamical simulations", *Journal of Sound and Vibration*, 2009, v. 324, pp. 297-316.

[71] A. Klarbring, "Contact, friction, discrete mechanical structures and discrete frictional systems and mathematical programming", P. Wriggers and P. Panagiotopoulos (eds), New developments in contact problems, Wien: Springer, 1999, pp. 55-100.